Dense medium separation **:** A dynamic model and medium loss analysis

by

Claire Lowry

Submitted in partial fulfillment of the requirements for the degree
Master of Engineering (Electronic Engineering)

in the

Department of Electrical, Electronic and Computer Engineering
Faculty of Engineering, Built Environment and Information Technology

UNIVERSITY OF PRETORIA

November 2023

SUMMARY

DENSE MEDIUM SEPARATION: A DYNAMIC MODEL AND MEDIUM LOSS ANALYSIS

by

Claire Lowry

Supervisor:	Prof. I. K. Craig
Co-supervisor:	Prof. J. D. le Roux
Department:	Electrical, Electronic and Computer Engineering
University:	University of Pretoria
Degree:	Master of Engineering (Electronic Engineering)
Keywords:	Dense medium separation, extended Kalman filter, ferrosilicon, iron ore, medium, medium losses, process modelling and identification, process observation

In this study, a model of a dense medium separation circuit of an iron ore plant in South Africa is developed, focusing on the flow of medium in the circuit. The model is used to simulate and detect medium losses within the dense medium separation circuit.

Dense medium separation (DMS) is a method of extracting valuable minerals from waste materials using gravitational and centrifugal forces. It is widely employed in the processing of various minerals, particularly coal and diamonds, as well as iron ore, complex sulfides, and base metal oxides. The fundamental principle of a DMS circuit involves separating low density material (product for coal plants, gangue for heavier mineral plants) from high density material (gangue for coal processing, product for heavier mineral processing) using a medium. This medium is utilized in the separation vessel, and then recovered. There are several points in the circuit in which the medium can be lost, and, as the medium can contribute between 18% and 39% of the total operating costs of metalliferous DMS plants, it is valuable to be able to detect and reduce the losses of this medium.

This dissertation presents a model for the DMS circuit at the plant studied. The circuit is divided into individual units: the correct medium, secondary, and dilute medium tanks, the mixing box, the primary and secondary densifiers, the dense medium cyclone and drain-and-rinse screens, and the magnetic separator. Each unit is modelled from first principles, with a focus on medium flows. Where possible, the units are modelled dynamically. The dense medium cyclone and drain-and-rinse screens, the primary and secondary densifiers, and the magnetic separator are, however, modelled in steady-state as their dynamics are assumed significantly faster than the rest of the circuit. The full circuit model is then simulated in a simulation platform, Simulink, and validated using plant data.

An observability study is conducted on the developed model of the circuit. The observability study shows that the dilute medium tank is not observable. Furthermore, the units modelled in steady-state (primary and secondary densifiers, the drain-and-rinse screens, and the magnetic separator) have very limited instrumentation, and thus it is not possible to confirm the outputs of these models online. However, the analysis shows that the correct medium tank and secondary tank models are fully observable, including for the augmented models where the flow into the tank is considered an unmeasured state. The mixing box model is also fully observable, including for the augmented system where a key parameter in the model is not known.

An extended Kalman filter is designed for estimation of unmeasured but observable states, and implemented on both simulation and plant data. The extended Kalman filter is shown to be accurate; however, the estimations of flow rates into the correct medium and secondary tanks are quite noisy. This study then presents an analysis of medium loss scenarios, and the developed model is used to simulate these. The extended Kalman filter developed is used for state estimation in these simulated medium loss scenarios, as well as on plant data of these scenarios where available. An analysis of the medium loss scenarios shows medium losses due to blockages in the mixing box resulting in overflows can be identified using state estimation, while the addition of a flow meter on the secondary densifier overflow is required in order for losses at the product and waste drain-and-rinse screens to be identified. Finally, the state estimation results show that medium losses to the magnetic separator effluent are not identifiable using state estimation and the developed model, and that a density-focused approach is possibly required for this.

Acknowledgments

I would like to thank Anglo American for the financial support to pursue this study, and would like to express my immense thanks to my colleagues and managers, who have provided much support and advice.

I would like to thank my supervisors, Prof. Derik le Roux and Prof. Ian Craig, for their guidance, support, patience and encouragement.

I would like to thank my mum and dad for their support and encouragement. I am also grateful to my brothers, grandmother, aunts, uncles, cousins and friends for their continuous encouragement. And I'd especially like to thank my baby cousin Thomas, whose mother made me promise to finish this dissertation before he started walking.

LIST OF ABBREVIATIONS

CM	correct medium
DM	dilute medium
DMC	dense medium cyclone
DMS	dense medium separation
EKF	extended Kalman filter
KF	Kalman filter
MB	mixing box
MPC	model predictive control
MS	magnetic separator
NMPC	nonlinear model predictive control
PD	primary densifier
SD	secondary densifier
SDR	specific drain rate

TABLE OF CONTENTS

LIST OF FIGURES

LIST OF TABLES

CHAPTER 1   INTRODUCTION

1.1   PROBLEM STATEMENT

1.1.1   Context of the problem

Dense medium separation (DMS) is a beneficiation process that separates valuable minerals from waste material, with the basic principle being the separation of low density material from high density material (Legault-Seguin et al., 2017). A dense medium is employed to achieve this separation. The medium is used in a separation vessel, and then recovered. In iron ore processing, ferrosilicon is used (Maré et al., 2015; Scott, 2017; Tom, 2015) as the medium, which is an expensive consumable (Dardis, 1989).

The process flow of the DMS circuit studied here is seen in Figure 1.1: correctly-sized ore is fed to a dense medium cyclone, where higher density material forms the underflow of the cyclone, and lower density material forms the overflow (Napier-Munn, 2018). Both overflow and underflow from the cyclone are passed to drain-and-rinse screens, where the medium slurry is drained and sent to the correct medium tank. The cyclone overflow and underflow are then rinsed with wash water. In iron-ore processing, the drained and rinsed cyclone overflow is transported via conveyor to the tailings, and the underflow is sent via conveyor to product stockpiles (Legault-Seguin et al., 2017).

The medium recovery circuit (highlighted in yellow in Figure 1.1) consists of a correct medium tank, a secondary tank, and a dilute medium tank, as well as two densifiers (primary and secondary), and the magnetic separator. The drained medium slurry is sent to the correct medium tank, while the rinsed medium slurry is sent to the dilute medium tank, from which it is pumped to the magnetic separator, and the concentrate is returned to the correct medium tank (O'Brien et al., 2016).

In an ideally operated and designed DMS plant, medium recovery would be 100% efficient, and no
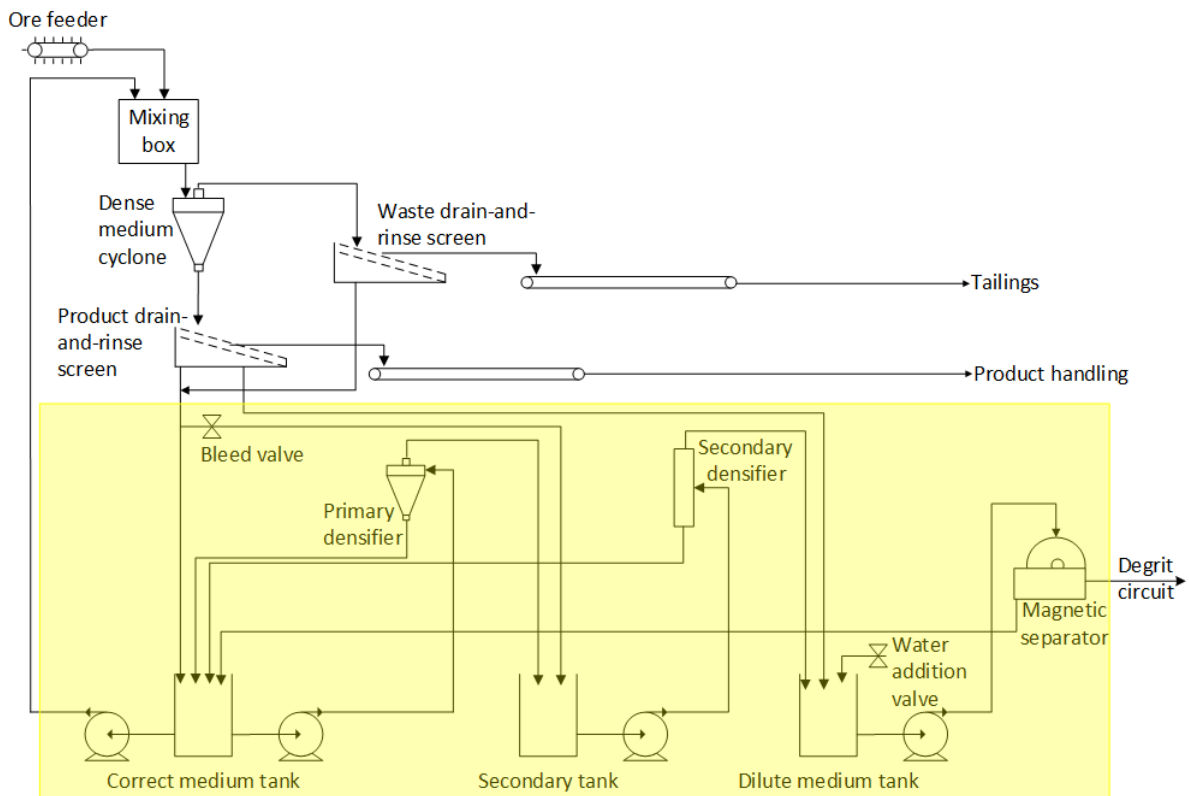
Figure 1.1. Diagram of a dense medium separation circuit at an iron ore plant, with medium recovery circuit highlighted in yellow.

losses of the medium would occur. However, in reality, between 200g and 500g of medium per ton of feed is lost (Dardis, 1989; Napier-Munn et al., 1995). These losses are continuous, and usually small in magnitude, with excessive losses occurring during short periods of time, in surging events (Dardis, 1989; Napier-Munn et al., 1995). Medium can be lost at various points in the circuit: at the drain-and-rinse screens due to adhesion to the ore or screen-blinding, in the effluent of the magnetic separator, or at the mixing box due to blockages causing overflows (Dardis, 1989; Napier-Munn et al., 1995). Ferrosilicon (the medium used in iron ore DMS plants) is an expensive consumable, and studies have shown that medium losses can contribute between 18% and 39% of the total operating costs of metalliferous DMS plants (Dardis, 1989; Rayner and Napier-Munn, 2003a). This work therefore focuses on modelling the medium flows within the DMS circuit with the goal of identifying medium losses, thus enabling their reduction.

1.1.2   Research gap

The problem to be addressed by this work is to detect excessive medium losses in a DMS circuit. Given that medium losses can contribute significantly to plant operating costs, detecting excessive losses can be economically advantageous. To detect the excessive medium losses, the medium flows within the DMS circuit need to be fully modelled.

While significant work has been done in modelling the DMS circuit, both in steady state and dynamically, there is little research reported in the literature, to the knowledge of the author, that is directly focused on the dynamic modelling of medium losses and the detection of excessive medium losses through modelling. Therefore, the development of a fully dynamic model, focusing on the flow of medium in the circuit, is required. This study addresses this requirement.

Given the lack of dynamic modelling focused on medium losses, there is also a lack of simulation of medium loss scenarios to provide insight into how medium losses occur. Furthermore, development of state estimation on such a dynamic model of the DMS circuit will investigate the feasibility of detecting medium losses in the DMS circuit, which is as yet unreported in the literature. This study addresses these gaps.

1.2   RESEARCH OBJECTIVE AND QUESTIONS

This research will address the following research questions:

1. Is it possible to model the dense medium circuit, focusing on medium flows and losses?

    (a) Is it possible to model the correct medium, secondary, and dilute medium tanks, and the mixing box focusing on medium flows?

    (b) Is it possible to model the primary and secondary densifiers, the dense medium cyclone, the drain-and-rinse screens, and the magnetic separator, focusing on medium flows?

2. Are the medium flows in the DMS model developed observable?

3. What are the typical key sources of medium loss within the DMS circuit?

4. Can the typical key sources of medium loss within the DMS circuit be simulated using the developed model?

5. Given the level of observability in the circuit, can the key sources of medium loss within the DMS circuit be detected?

6. If not, what additional instrumentation is required for the medium losses within the DMS model to be observable?

1.3 HYPOTHESIS AND APPROACH

While flow measurements of the medium in the circuit are not available, the levels of the tanks within the circuit, as well as the discharge pressure of pumps in the circuit are available. Thus, the hypothesis of this dissertation is that the medium flows within a DMS circuit can be modelled with the medium flows being observable, and that this model can be used to simulate medium losses, while state estimation of the model can be used to detect medium losses.

In order to answer the research questions posed in this proposal, and to test the hypothesis formed, the following approach will be followed:

1. A literature study will be conducted focusing on the DMS process, medium losses in DMS circuits, modelling of the DMS circuit and individual components in the circuit both in steady-state and dynamically, and control of the DMS circuit.

2. Based on the review of the literature, a model will be developed for the individual units within the DMS circuit, and combined to form a model of the full circuit.

3. The developed model of the full DMS circuit will be simulated and validated using plant data.

4. The developed models of the DMS circuit units will be assessed for observability.

5. State estimation will then be developed for the DMS circuit units that are found to be observable.

6. The developed state estimation will be tested on simulation data, and implemented on plant data.

7. Sources of medium losses in the DMS circuit will be identified and simulated using the developed model.

8. The state estimation developed for the model will be applied to simulated medium loss scenarios. Where available, the developed state estimation will be implemented on plant data for known medium loss events.

9. The performance of the state estimation in detecting medium loss events will be analysed. Additional instrumentation required to improve the capability to detect medium losses will be analysed.

10. The study will conclude with an evaluation of the effectiveness of the developed model and state estimation in detecting medium losses, and will propose avenues for further work to improve the effectiveness.

1.4   RESEARCH GOALS

The goals of this research are as follows:

- Develop a model of the DMS circuit, focusing on medium flows.

- Simulate and validate (with plant data) the developed model of the DMS circuit.

- Assess observability of developed model, and develop state estimation of observable but un-measured states.

- Develop and apply state estimation to simulation and plant data.

- Simulate medium losses and assess effectiveness of state estimation in detecting medium losses.

- Identify additional instrumentation required to improve medium losses detection.

1.5   RESEARCH CONTRIBUTION

The contribution of this work is to develop a dynamic model of the DMS circuit, focused on the flow of medium in the circuit, and to develop state estimation for the observable but unmeasured states. The model is simulated and validated using plant data. This study uses this model to simulate medium losses, and the observability of these losses is assessed. State estimation is applied to the simulated medium loss events, as well as to plant data of medium loss events where available. This work therefore analyses medium losses in the DMS circuit, demonstrates if these losses can be observed given the current level of instrumentation on the circuit, and makes recommendations for additional instrumentation, to allow for full observability of medium losses.

1.6   RESEARCH OUTPUTS

The dynamic non-linear model for the DMS circuit focusing on medium losses, which is developed, analysed for observability, simulated and validated in Chapters 3, 5, 4 and 4.3 respectively, as well as the state estimation developed in Chapter 6 was submitted for publication:

- Lowry, C., J.D. le Roux, and Craig, I.K., Analysis and validation of a dynamic dense medium separation circuit model for detecting medium losses, submitted to *Minerals Engineering*.

1.7   OVERVIEW OF STUDY

This study begins with a literature review in Chapter 2, which covers the work done in the modeling and control of the DMS circuit to date, as well as studies on medium and medium losses. Chapter 3 presents a model for the individual units within the DMS circuit. This is followed by Chapter 4, in which the developed models of the individual units are combined on a simulation platform, Simulink, and simulated. The developed model is then validated using plant data. In Chapter 5 the observability of each unit is discussed. In Chapter 6, state estimation of the observable units is developed, and implemented on simulation and plant data. Sources of medium loss are then discussed and simulated in Chapter 7. State estimation is applied to these simulations and, where possible, to plant data of these scenarios. Chapter 8 then discusses the results of the medium loss state estimation, and the observability of medium losses overall. Finally, a summary of the study as well as concluding remarks and recommendations for future work are given.

CHAPTER 2   LITERATURE STUDY

2.1   INTRODUCTION

Dense medium separation (DMS) is a beneficiation process that utilises gravitational and centrifugal forces to separate valuable minerals from waste material (Legault-Seguin et al., 2017; Lundt and Grewalt, 2017; Maré et al., 2015). This technology is used in the processing of many minerals, predominantly coal and diamonds, and also iron ore, complex sulphides and base metal oxides, amongst others (Legault-Seguin et al., 2017; Lundt and Grewalt, 2017; Napier-Munn et al., 1995). The basic principle of a DMS circuit is the separation of low density material (product in the case of coal plants, gangue in the case of heavier minerals plants) from high density material (gangue in coal processing, and product in heavier mineral processing) (Legault-Seguin et al., 2017; Maré et al., 2015; Napier-Munn et al., 1995). The DMS process employs a medium to achieve this separation. The medium is used in the separation vessel, and then recovered. In coal processing, magnetite is used as the medium, and in metalliferous ore ferrosilicon is used (Maré et al., 2015; Scott, 2017; Tom, 2015). There are several points in the circuit in which the medium can be lost, and given its significant cost, it is important to be able to detect and reduce the losses of this medium.

This survey gives a broad review of the available literature on the DMS process, with particular focus on the medium recovery within this process, and potential sources of loss of this medium. The work done on modelling of the components of the DMS circuit, as well as on control and optimisation of the process, is extensively reviewed. The focus of this dissertation is on iron ore processing, rather than coal or other mineral processing, so particular attention will be paid to literature specific to iron ore. However, due to the dominance of coal in the application of DMS circuits, work done on coal circuits is also reviewed here, through the lens of detecting and controlling medium losses.

2.2   DENSE MEDIUM SEPARATION PROCESS

A typical DMS circuit consists of two high level processes: separation of low density material from high density material, and medium recovery (Legault-Seguin et al., 2017; Maré et al., 2015). Correctly-sized ore (crushed to an appropriate size in upstream processes) is fed to a separation vessel, along with the dense medium. The separation vessel can be static open-bath separators (such as drums), usually used for coarser material, or dynamic vessels (centrifugal devices such as cyclones) for finer material (Legault-Seguin et al., 2017). This dissertation will focus exclusively on the dense medium cyclone as the separation vessel. Material that is of a higher relative density than the medium forms the underflow of the cyclone, and material of lower relative density than the medium forms the overflow (Napier-Munn, 2018; Tom, 2015). Both overflow and underflow from the cyclone are passed to drain screens, where the medium slurry is drained and sent to the correct medium tank. The cyclone overflow and underflow are passed to rinse screens, where the material is rinsed with wash water. The rinsed medium slurry is sent to the dilute medium tank (as it has been diluted with the wash water). The drained and rinsed cyclone overflow and underflow is then sent to further processing (Legault-Seguin et al., 2017).

The medium recovery process of a DMS plant consists of two circuits: the correct medium circuit, and the dilute medium circuit (Legault-Seguin et al., 2017; Napier-Munn et al., 1995; Tom, 2015). As previously described, the medium slurry from the drain section of the drain-and-rinse screen is sent to the correct medium tank. The diluted medium from the rinse section of the screen is sent to the dilute medium tank. The simplest form of a DMS plant has only two tanks - the correct medium tank and the dilute medium tank (Scott, 2017). In these plants dilute medium is pumped from the dilute medium tank to magnetic separators, and the concentrate is returned to the correct medium tank (O'Brien et al., 2016; Rayner and Napier-Munn, 2003a; Scott, 2017). Magnetic separators consist of a rotating magnetic drum mounted on a shaft in a feed pan, with an effluent collection pan. Dilute medium is fed to the feed pan, and the non-magnetic material passes in a natural path to the effluent collection pan, and is then transported to the tails. The magnetic material (the concentrate medium) is drawn to the magnetic drum and is rotated out of the non-magnetic flow and thus recovered (Rayner and Napier-Munn, 2003a,b). A diagram of a typical wet drum magnetic separator is shown in Figure 2.1.
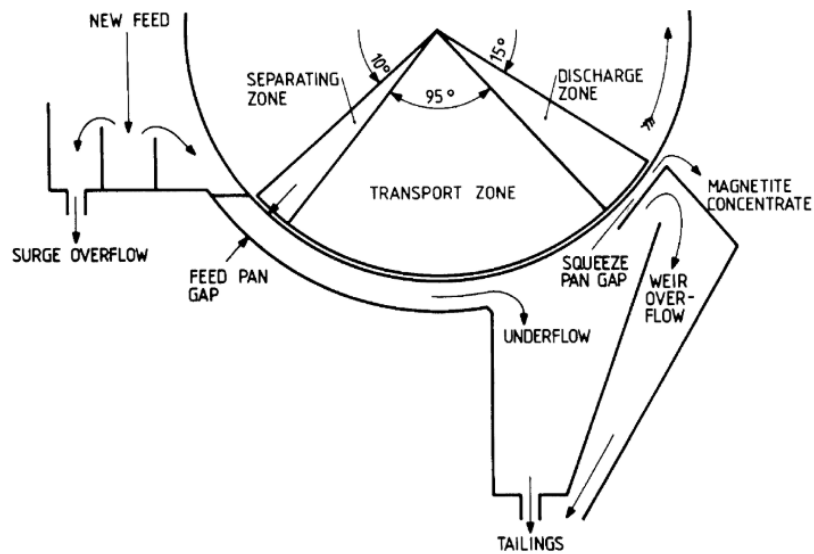
Figure 2.1. Diagram of the operation of a typical wet drum magnetic separator. Taken from Rayner and Napier-Munn (2003a), with permission.

The recovered concentrate medium from the wet drum magnetic separator is then sent to the correct medium circuit. Medium returning to the correct medium tank is kept at a higher density than required, and the density is then reduced through water addition to the correct medium tank or in-line, directly to the correct medium pump (Legault-Seguin et al., 2017; O'Brien et al., 2016). The process that has been described here is the simplest form of the DMS circuit (Scott, 2017). A schematic of such a circuit is shown in Figure 2.2.
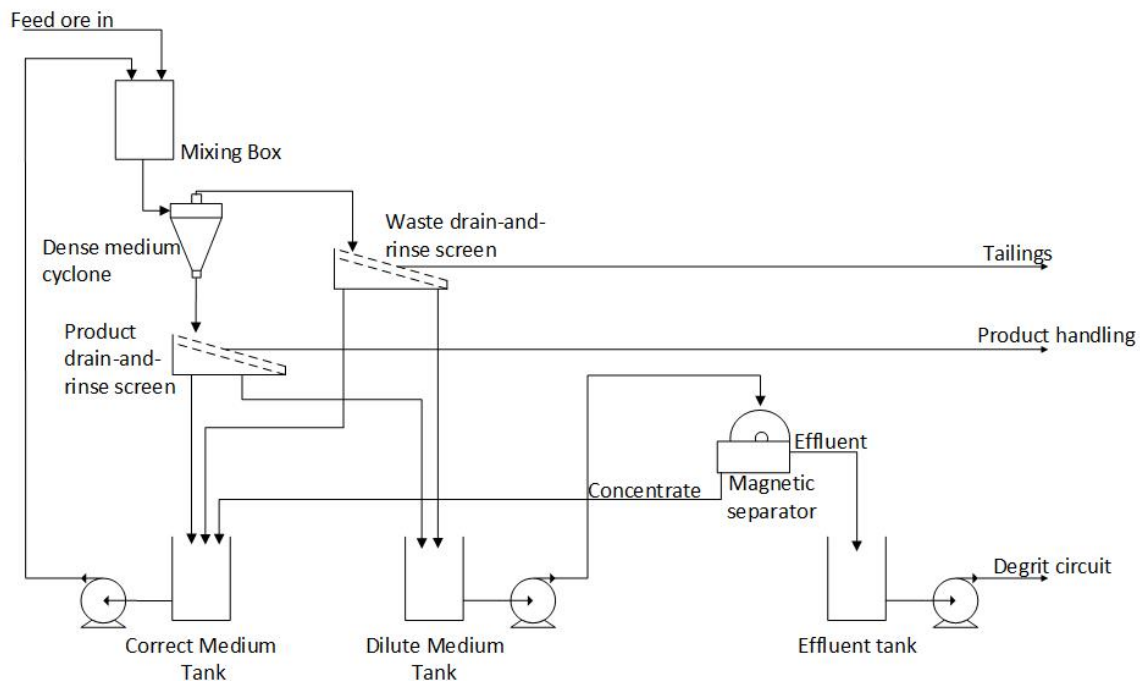
Figure 2.2. Diagram of a simple DMS circuit.

Many plants are configured in variations of the design seen in Figure 2.2. In some plants, such as the plant studied in this dissertation, densifiers (in the form of hydrocyclones and/or pipe densifiers) are used to achieve the higher-than-required density of the medium (Legault-Seguin et al., 2017; Scott, 2017). These allow for de-watering and thickening of the medium (Scott, 2017).

2.3   MEDIUM

The dense medium used in DMS circuits is of great importance, as it is largely responsible for defining the density cut-point of the dense medium cyclone, with material of higher density than the medium reporting to the overflow, and material of lower density reporting to the underflow of the cyclone. This determines the efficiency of the circuit as a whole. Magnetite is used as the dense medium in coal processing, whereas in iron ore and other heavy mineral processing, where the density of separation is significantly higher, the dense medium used is ferrosilicon (Rayner and Napier-Munn, 2003a; Scott, 2017; Tom, 2015). Ferrosilicon is an expensive consumable. According to Dardis (1989), the cost of ferrosilicon losses accounts for between 18% and 39% of the total operating costs of DMS circuits. There is therefore a strong economic incentive to optimise medium recovery and reduce losses of ferrosilicon in a DMS circuit (Dardis, 1989).

2.3.1 Sources of medium losses

Napier-Munn et al. (1995) found that there are two possible sources through which medium can be lost from the circuit, which can be identified by studying a typical DMS process flowsheet (such as that in Figure 2.2). This concurred with work done by Dardis (1989). These sources are as follows:

2.3.1.1 Adhesion losses

Medium adheres to the products of the dense medium cyclone, after undergoing draining and washing on the screens. Adhesion losses are greatly influenced by the porosity of the ore (Dardis, 1989; Napier-Munn et al., 1995; Rayner and Napier-Munn, 2003a; Sripriya et al., 2006), and will be higher when the ore is more porous. The level of medium adhesion is also influenced by the drain-and-rinse screen washing configuration: if the washing process is sub-optimal, the adhesion losses will be greater (Dardis, 1989; Napier-Munn et al., 1995). Adhesion losses also increase with increased loading of the screen, and bed depth (Dardis, 1989; Napier-Munn et al., 1995).

2.3.1.2 Magnetic separator losses

Medium is present in the effluent of the wet drum magnetic separators and is therefore lost to the circuit (Dardis, 1989; Napier-Munn et al., 1995). These losses are greatly influenced by the efficiency of the magnetic separator, and the conditions under which it is operated (Rayner and Napier-Munn, 2003a). If the magnetic separator feed density is not within the supplier-recommended operating range (and the same applies to the feed flow rate), it will operate sub-optimally and losses will occur. Magnetic separator settings, such as pulp height, magnetic position, separation and discharge zone gaps, drum speed and the ratio of magnetics to non-magnetics also affect the performance of the magnetic separator, and therefore the amount of medium lost to the effluent (Dardis, 1989; Rayner and Napier-Munn, 2003a,b).

2.3.2 Factors affecting medium losses

There are numerous causes that are specific to adhesion losses (eg. ore porosity and increased screen loading), as well as to magnetic separator effluent losses (eg. magnetic separator gap setting). Napier-Munn et al. (1995), through studies on four DMS plants (two iron ore plants, one manganese plant and one tin concentrator plant), investigated operational factors that affect both these sources of losses. The first is operating density. It was found that both adhesion losses as well as magnetic effluent losses increase with increasing density, with the increase being largely due to poor drainage on the drain-and-rinse screens as a result of higher medium viscosity (Napier-Munn et al., 1995). Sripriya et al. (2006) found the same in a separate study on a coal DMS plant in India. The second factor is

plant downtime. Again, it was found that medium losses increased with increased plant downtime, and this was also observed separately by Dardis (1989). This effect is not well understood, but is thought to be due to housekeeping practices.

Causes of observed medium loss that are much more difficult to measure include losses due to housekeeping (during plant stoppages and during normal operation), losses during ferrosilicon make-up (where the medium slurry is prepared to be added to the circuit), undetected surges due to imbalances in magnetic separator flows, screen wash water stoppages, and corrosion of the medium (Dardis, 1989; Napier-Munn et al., 1995).

2.3.3   Amount of medium lost

The task of quantifying the amount of medium lost through the two discussed sources (adhesion and magnetic separator losses) is not trivial. Observed losses of ferrosilicon range between 200g and 500g per ton of feed, and it is generally accepted that only about 50% of observed ferrosilicon losses can be measured (Dardis, 1989; Napier-Munn et al., 1995). This is due to a number of the causes of losses (such as corrosion of the medium, and housekeeping) being very difficult to measure. This is further exacerbated by the fact that a large percentage of the losses occur over a short time period (generally due to flow surges or overloading of the circuit), which renders most sampling procedures ineffective (Napier-Munn et al., 1995).

Additionally, there is not consensus in the literature on the relative contribution of the two sources (adhesion and magnetic separator effluent) to the total ferrosilicon losses in a DMS circuit (Rayner and Napier-Munn, 2003a; Scott, 2017; Sripriya et al., 2006). Dardis (1989) attributes 75% of losses to magnetic separator effluent, and the remainder to adhesion losses. Mulder (1985) on the other hand found that only 18% of medium losses are via the magnetic separator effluent at Sishen Mine in South Africa, with the balance lost through adhesion, and Napier-Munn et al. (1995), found that between 70% and 80% of the measured losses were attributable to adhesion, with the remaining 20% to 30% due to losses in the magnetic separator effluent. Napier-Munn et al. (1995) did, however, concede that conventional plant surveys can underestimate magnetic separator loss due to short time period high loss episodes.

2.4   DMS AND MEDIUM LOSSES MODELLING

As explored in Section 2.3, both adhesion and magnetic separator losses are affected by operating variables such as medium density, viscosity, flow rate, amongst others. Modelling of the circuit

that accurately predicts these variables can therefore be of use in the detection of medium losses, as abnormal operating conditions can be identified using models of the process (Tom, 2015).

A significant amount of work has been done on modelling the components of a DMS circuit. Most work done to model the circuit has been to develop steady-state models of the various components of the circuit (such as the dense medium cyclone and the wet drum magnetic separator). More recently, there has been increased interest in dynamic modelling of the circuit. The following review of models will focus on work that includes modelling medium flows, as that is of chief concern in this dissertation.

2.4.1 Steady-state models

There is a host of literature on steady-state models developed for the dense medium cyclone, the most notable of which is Wood's model (Clarkson and Wood, 1993). Steady-state models for pumps, too, are extensively available in the literature. Drain-and-rinse screens and the wet drum magnetic separator have not been reviewed as extensively.

2.4.1.1 Dense Medium Cyclone

The simplest representation of a dense medium cyclone is through a partition curve (Napier-Munn, 1991; Narasimha et al., 2007). A partition curve defines the proportion of material of any given density in the feed which reports to the underflow of the cyclone. The proportion is called the partition number, and is generally expressed as a percentage. The separating density, or cut-point density, ρ_{50}, is the density at which material is equally divided between the overflow and the underflow of the cyclone (Napier-Munn, 1991; Narasimha et al., 2007). Particles of different sizes behave differently, and so partition curves must be calculated separately for each particle size class or interval. The purpose of a model of a dense medium cyclone is therefore to predict the partition curve with an acceptable level of accuracy, while also providing insight into additional aspects such as throughput and medium partitioning (Napier-Munn, 2018, 1991). Napier-Munn (2018) provided a comprehensive overview of the work done in modelling the dense medium cyclone up until 2018. Published models that are available for general use, configurable using a spreadsheet of input variables, and valid over a wide range of operating conditions, are quite rare. The generally accepted standard for coal processing is a model developed by Clarkson and Wood (1993), which has been expanded into a simulation package (Barbee et al., 2005). The model is divided into three categories of calculations: medium calculations, partition calculations, and application checks. The methodology can be visualised by the flow diagram shown in Figure 2.3.
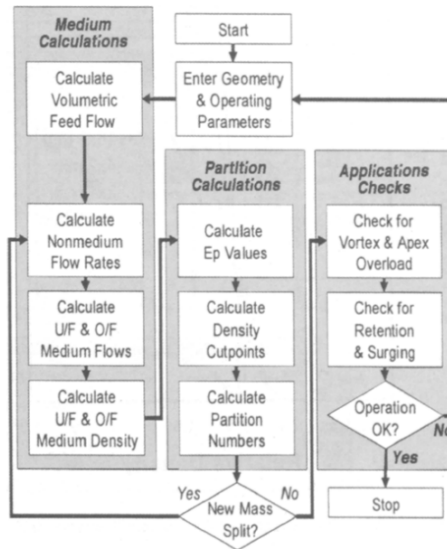
Figure 2.3. Dense medium cyclone simulation methodology. Taken from Barbee et al. (2005), with permission.

The medium set of calculations requires calculation of the volumetric flow rates of the dense medium cyclone. The total volumetric capacity is governed by the cyclone geometry and inlet pressure, which is expressed in terms of equivalent diameters of medium head (H). The total volumetric feed capacity can then be determined (Clarkson and Wood, 1993):

$$Q_f = KD_c^{1.93}H^{0.45}(D_u/D_o)^{0.15} \tag{2.1}$$

where D_c is the diameter of the cyclone, D_u is the apex diameter (underflow), D_o is the vortex finder diameter (overflow), and K is an empirical fitting and unit conversion coefficient.

In the absence of ore feed, the volumetric flow rate of medium to the underflow of the cyclone (Q_{um}^*) is calculated, and then adjusted to obtain the volumetric flow rate of medium to the underflow in the presence of ore feed (Q_{um}) (Clarkson and Wood, 1993):

$$Q_{um}^* = Q_f \left(\frac{0.79}{H^{0.37}} \right) \left(\frac{D_u}{D_o} \right)^{4.2} \tag{2.2}$$

$$Q_{um} = 0.97Q_{un} + \frac{{Q_{um}^*}^2}{Q_{un} + Q_{um}^*} \tag{2.3}$$

where Q_{un} is the volumetric flow rate of nonmedium solids (product, in the case of iron ore) in the cyclone underflow. In the simulation package developed subsequent to Wood's model (Barbee et al., 2005), an iterative method was used to calculate Q_{un}. In each iteration, the partition numbers predicted

by the dense medium cyclone model (discussed later) are used to recalculate the underflow mass flow rate. The calculated underflow mass flow rates for each density interval are normalised by their densities, and the resulting incremental volumes are summed to obtain an updated estimate of Q_{un}. The process is continued until a steady-state value for Q_{un} is reached.

The medium split to underflow is then calculated, and the underflow medium density is then determined using an empirical relationship, as follows:

$$\rho_{um} = 0.459 \rho_{fm} \left(\frac{Q_{um}}{Q_{fm}} \right)^{0.194(\rho_{fm}-2.04)} \left(\frac{P_{RR}^{0.17} H^{0.082}}{D_c^{0.1}} \right) \tag{2.4}$$

where P_{RR} is the Rosin-Rammler intercept of the feed medium size distribution determined using the laser-diffraction technique. The overflow medium density (ρ_{om}) can then be calculated using a volume balance approach as follows:

$$\rho_{om} = \left(\frac{\rho_{fm}}{1 - (Q_{um}/Q_{fm})} \right) \left(1 - \frac{Q_{um}\rho_{um}}{Q_{fm}\rho_{fm}} \right) \tag{2.5}$$

Using the volumetric flow rates of the underflow and overflow, as well as the density thereof, calculated in (2.5), the partition curves (for each particle size interval) of the dense medium cyclone can be determined. First, the Ecart Probables (E_p) is calculated. This is an empirical measure of the inefficiency of the cyclone, and describes the departure of the curve from a perfect partition which would be a vertical line at the cut-point density (Napier-Munn, 1991). Wood's model (Clarkson and Wood, 1993) assumes that the partition curves for all particle size classes have a common pivot point (ρ_{50}^*), which is calculated using the feed medium density, the underflow medium density and the overflow medium density. The density cut-point (ρ_{50}) for each specific particle size class is then calculated as follows:

$$\rho_{50} = \rho_{50}^* + \frac{E_p}{1.0986} \ln \left(\frac{Q_{fm}}{Q_{um}} - 1 \right) \tag{2.6}$$

The partition number for a given size interval is then estimated from the Whiten partition model (Clarkson and Wood, 1993; Scott, 2017):

$$P = \frac{1}{1 + \exp(1.0986(\rho_{50} - \rho)/E_p)} \tag{2.7}$$

Plotted against density, this forms a sigmoid curve and represents the probability (P) of a particle of a certain density reporting to the underflow of the cyclone. An example of such a curve, for different particle size intervals, is shown in Figure 2.4.
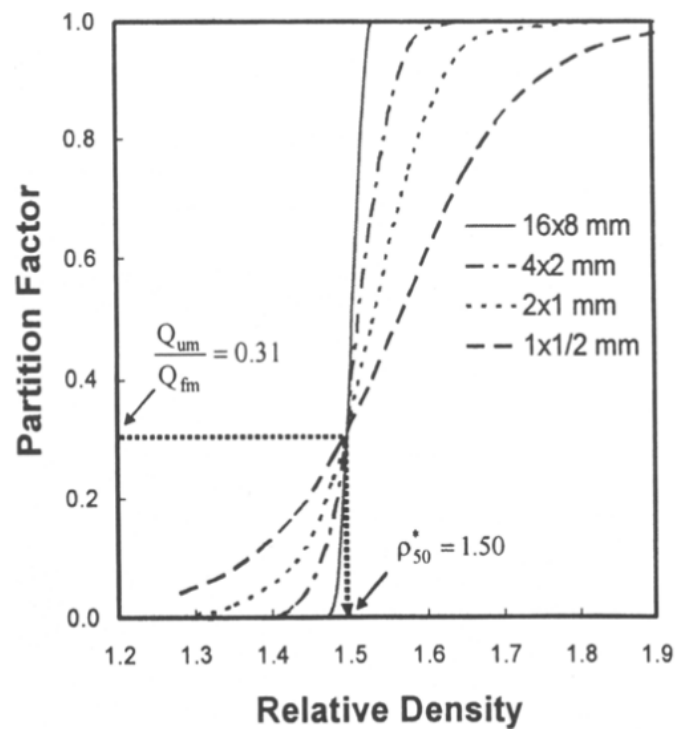
Figure 2.4. Partition curves for different size classes of a dense medium cyclone. Taken from Barbee et al. (2005), with permission.

Wood's model (Clarkson and Wood, 1993) and subsequently developed simulation package (Barbee et al., 2005) is the most widely used model of a dense medium cyclone (Napier-Munn, 2018), particularly in the coal industry. Dunglison (1999) expanded on Wood's work, and produced a more broadly applicable model to heavier minerals (such as iron ore). It is not used frequently in industry, however, as it was not widely published and is not easily available (Scott, 2017). Scott (2017) investigated both the Wood and Dunglison models and found negligible differences between the models. It should be noted, however, that this comparison was done using data from a coal plant. It is possible that for heavier minerals such as iron ore, the differences in the models' outputs would be more significant.

2.4.1.2 Densifiers

In DMS circuits that require lower operating densities (such as coal separation, where the density ranges between 1.4 and 1.8 SG), the magnetic separator is sufficient for removing water to allow density control (Legault-Seguin et al., 2017). However, for DMS circuits that operate at higher densities (such as iron ore processing, which requires densities higher than 2.5 SG), densifiers are required for adequate density control. Adequate control of the circuit density is necessary in order to achieve the

desired cut-point density of the dense medium cyclone (Napier-Munn, 1991; Narasimha et al., 2007). To sufficiently control the density, water must be removed from the correct medium that circulates in the circuit. This is because there are various points at which water is added to the medium: through the ore feed, through rinse screen water sprays, and through medium pump gland water (Legault-Seguin et al., 2017).

Legault-Seguin et al. (2017) explores the use of densifiers in DMS circuits. Densifiers are divided into two categories: cyclone densifiers and pipe densifiers. The cyclone densifier is a hydrocyclone or battery of hydrocyclones, while the pipe densifier is a long cylindrical pipe with a feed inlet and a tangential outlet. Legault-Seguin et al. (2017) gives typical mass balances of pipe and cyclone densifiers:

Table 2.1. Pipe and cyclone densifiers mass balance (adapted from Legault-Seguin et al. (2017)).

Stream	Flow rate (m^3/hr)		Magnetics Recovery (%)	
	Cyclone	Pipe	Cyclone	Pipe
Feed	20	20	100	100
Overflow	14	6	53	3
Underflow	6	14	47	97

A comparison of the mass balances of the two types of densifiers in Table 2.1 shows that the pipe densifier rejects a far lower percentage of magnetics to its overflow in comparison to the cyclone densifier. This has the advantage of reducing the magnetic load to the dilute medium circuit, and therefore to the magnetic separator (Legault-Seguin et al., 2017).

In addition to the overview of densifiers given by Legault-Seguin et al. (2017), there is extensive work on hydrocyclones. In his book entitled 'Solid-Liquid Separation', Svarovski (2000) explores the flow patterns, pressure distribution, function, design and merits of hydrocyclones. The theories of separation as well as hydrocyclone models are also explored. As reviewed by Nageswararao et al. (2004), there are two prominent mathematical models of hydrocyclones that are used most in industry and in the literature (Bueno, 2021; Nageswararao et al., 2004; Svarovski, 2000). A brief summary of these is below:

- **Plitt hydrocyclone model**

Plitt (1976), revised in Flintoff et al. (1987), developed a mathematical model of a hydrocyclone (in steady-state) which outputs the cyclone throughput Q, the cut size d_{50c}, the volumetric flow split S and the sharpness of classification m. The inputs to this model are the diameters of the cyclone, vortex, spigot and inlet (D_c, D_o, D_u, and D_i respectively), as well as the free vortex height h. The model was developed using 297 sets of data from different cyclones, with different feeds: silica, copper, ore, tailings and silica flour. Linear regression was then used to produce relationships between the input and output variables. Plitt claimed that the performance of a hydrocyclone could be reasonably accurately estimated using the developed model, even without experimental data being available. The volume split equation from Plitt (1976) and Flintoff et al. (1987) is:

$$S = \frac{Q_{underflow}}{Q_{overflow}} = a\frac{\left(\frac{D_u}{D_o}\right)^b (D_u^2 + D_o^2)^c h^d e^{0.54\psi}}{D_c^f H^g} \tag{2.8}$$

where H is the slurry feed head, and ψ is the volume fraction of solids in the feed. The parameters a to g in (2.8) can be calibrated using experimental data (Nageswararao et al., 2004), but should none be available, then Plitt (1976) recommends the following values:

$$a = 3.79 \quad b = 3.31 \quad c = 0.36 \quad d = 0.54 \quad f = 1.11 \quad g = 0.24$$

- **Nageswararao hydrocyclone model**

Nageswararao (1978), following work by Lynch and Rao (1975), developed a generalised model for hydrocyclones. The inputs to this model are the cyclone diameter D_c, reduced vortex finder D_o/D_c, reduced spigot D_u/D_c, reduced inlet D_i/D_c, reduced length of cylindrical section L_c/D_c, and cone angle θ. The model outputs are the Euler number, EU, the dimensionless cut size D_{50c}/D_c, the recovery of water to the underflow R_f, and the volumetric recovery of feed slurry to underflow R_v. As this work is mostly concerned with flow rate, the equation for R_v is shown below:

$$R_v = K_{V^0} D_c \left(\frac{D_o}{D_c}\right)^{-0.94} \left(\frac{D_u}{D_c}\right)^{1.83} \left(\frac{D_i}{D_c}\right)^{-0.25} \left(\frac{L_c}{D_c}\right)^{0.22} \theta^{-0.24} \left(\frac{P}{\rho_p g D_c}\right)^{-0.31} \tag{2.9}$$

where P is the cyclone feed pressure, ρ_p is the density of the cyclone feed pulp, and K_v is a material specific constant. Note that R_v is related to the volumetric split as follows (and therefore can be compared to that of Plitt's model in (2.8)):

$$R_v = \frac{S}{S+1} \tag{2.10}$$

2.4.1.3   Magnetic Separator

Early modelling of the magnetic separator was done in Wiegel (1976) using eight data sets from a wet drum magnetic separator. The model used regression equations formed from the data sets, for misplacement of magnetics and non-magnetics. Baker (1977) then developed a model for the recovery of medium (specifically magnetite) in a wet drum magnetic separator. The developed model could predict how different mediums would perform in a specific magnetic separator, with the same operating variables, but did not model the effect of changing one of these variables. In further work by Davis and Lyman (1983), magnetic separator operation was studies with a focus on the recovery of magnetite. It was found that the feed pan clearance, squeeze pan clearance, dry magnetite feed rate and magnetic separator drum speed were the significant operating variables, and a model was developed for magnetite loss.

Following this work, Rayner and Napier-Munn (2003a) developed a model for the recovery of magnetics in wet drum magnetic separators. Rayner and Napier-Munn (2003a) found that the magnetic separator works on the basis of flocculation. When the feed to the magnetic separator is exposed to the magnetic field of the drum, there is rapid formation of magnetic flocs (see Figure 2.1). A significant fraction of the magnetic solids in the feed will form part of these flocs. Rayner's model uses this concept of flocculation to model this process, and thus the fractional loss (the proportion of unflocculated particles), L, is:

$$L = e^{-k\frac{V}{Q_F}} \tag{2.11}$$

where Q_f is the volumetric feed flow rate per unit length, V is the volume of the separation zone per unit length, k is a first order rate constant and t is the flocculation time.

The rate constant k is derived in terms of feed, design and operating variables (such as non-magnetics contamination, drum diameter, volume concentration of solids in the feed, amongst others), as well as a number of parameters that require plant data to be fitted. The model includes an equation for the volumetric flow rate through the drainage area which then becomes the concentrate flow to the secondary and correct medium tanks:

$$Q_D = hQ_f \left(\frac{D^2\omega}{Q_f}\right)^i \left(\frac{x_p}{D}\right)^j \left(\frac{x_D}{D}\right)^k M_f^l \left(\frac{\rho_s Q_f}{F}\right)^m \tag{2.12}$$

where h, i, j, k, l, m are parameters to be fitted, D is the drum diameter, ω is the drum rotational velocity, x_p and x_D are the pickup and discharge gaps respectively, M_f is the feed moisture, Q_f and F

are the volumetric and mass feed rates per unit length respectively, ρ_s is the solids density, and M_f is the feed moisture.

Rayner and Napier-Munn (2003a) then validated the model against new sets of trials and it was found that the model was acceptably accurate in predicting magnetic losses.

In a separate paper, Rayner and Napier-Munn (2003b) modelled the concentration of solids in the concentrate output of the wet drum magnetic separator. This model is based on the theory that concentrate undergoes drainage and thereby is dewatered, and can thus be represented by an initial moisture, a drainage rate and a residence time:

$$M = 0.15 + (M_o - 0.15)e^{-g\left(\frac{780 + 260x_D}{Q_D}\right)} \tag{2.13}$$

where M is the concentrate moisture, M_0 is the initial moisture (determined from the feed moisture using operational parameters), g is the first order rate constant, x_D is the discharge gap, and Q_D is the volumetric flow rate of the drainage zone.

Again, the model showed acceptable agreement between predicted and observed concentrate solids content. For both the magnetic recovery model (Rayner and Napier-Munn, 2003a) and the concentrate solids content model (Rayner and Napier-Munn, 2003b), it is acknowledged that it was developed and fitted using the specific type of machine used in the work, and that extrapolation to other models of machine would be possible, but might require re-estimation of the parameters (Rayner and Napier-Munn, 2003a,b).

In addition to these models developed in Rayner and Napier-Munn (2003a) and Rayner and Napier-Munn (2003b), Legault-Seguin et al. (2017) gives mass balances at two differently configured DMS circuits, which includes the mass balances of the magnetic separators in the circuit, operating at different densities. Stener et al. (2016) also conducted a study in which the internal material flow in a magnetic separator was measured using an ultra-sound based method . This work did not produce a model, but does give insight into typical flows within a magnetic separator.

2.4.1.4 Drain-and-rinse screens

Banana screens are used for the process of draining and rinsing in a DMS circuit. Firth and O'Brien (2010) developed a model for a drain-and-rinse banana screen based on the comparison of the system (a mix of medium and ore passing over a screen) to a fluid in a pipe with features that provide resistance

to its flow under a force. Using this, the specific drain rate (*SDR*) of media from the drain section is calculated using experimentally determined constants, as well as properties of the screen:

$$SDR = C_1 Q^{0.5} A_p^{0.5} OA^{0.5} / (\sin \theta^{0.25} (1 + C_2 (\omega Am \cos \sigma / \cos \theta)^{C_3})^{0.25} e^{C_4 \phi}) \qquad (2.14)$$

where C_1, C_2, C_3 and C_4 are fitted constants, Q volumetric flow rate of medium and underflow solids, OA open area of the screen, θ is screen panel angle to the horizontal, ω is the screen vibration frequency, Am is the vibration amplitude, σ is the angle of throw, and ϕ is the volume fraction of coarse coal in the feed.

Dong et al. (2009) also developed a model for banana screens, focusing on particle flow in a typical multi-deck banana screen. However this model did not specifically consider drain-and-rinse screens, and additionally it only modelled dry particles, and therefore is not applicable to a drain-and-rinse screen in a DMS circuit.

2.4.1.5 Pumps

Pumps are fairly well studied in the literature, particularly in steady-state. The Pump Handbook (Karassik, 2008) provides a detailed understanding of pump theory for different types of pumps. Pumps can be classified by the principle by which energy is used: dynamic or displacement, and then by how this principle is implemented. Dynamic pumps can therefore be further split into centrifugal and special effect pumps. The pumps in the plant studied in this work are centrifugal pumps. Modelling of centrifugal pumps relies primarily on energy transfer relationships: mechanical input shaft power to the pump impeller results in an increase of pumping energy (Karassik, 2008). This is governed by the first law of thermodynamics, that is, *energy can neither be created nor destroyed, only altered in form* (Schmitz, 2017).

Applying the first law of thermodynamics to the pump system, and considering the system adiabatic (that is, considering any heat transfer as negligible), the following steady-flow energy equation is formed (Karassik, 2008):

$$P_s = \dot{m}(g\Delta H + \Delta u) \qquad (2.15)$$

where P_s is the mechanical shaft power, $\dot{m}$ is the mass flow rate, g is the gravitational acceleration constant, H is the head of the pump, and Δu represents efficiency losses. Thus, the shaft power is transformed into fluid power, which is the mass flow rate multiplied by the change in the total enthalpy. The head of the pump can be expressed in terms of static head, velocity head, pressure head and geodetic head (head due to displacement from a reference point), according to Bernoulli's equation

(Talmon, 2016):

$$H = h + \frac{p}{\rho g} + \frac{V^2}{2g} \qquad (2.16)$$

where h is the vertical displacement, p is the fluid pressure, ρ is the density of the fluid, and V is the velocity of the fluid. This relationship gives rise to a quadratic relationship between the pressure differential developed by a pump, and the flow rate of fluid from a pump, at constant speed, and constant pumping efficiency, as seen in Figure 2.5.
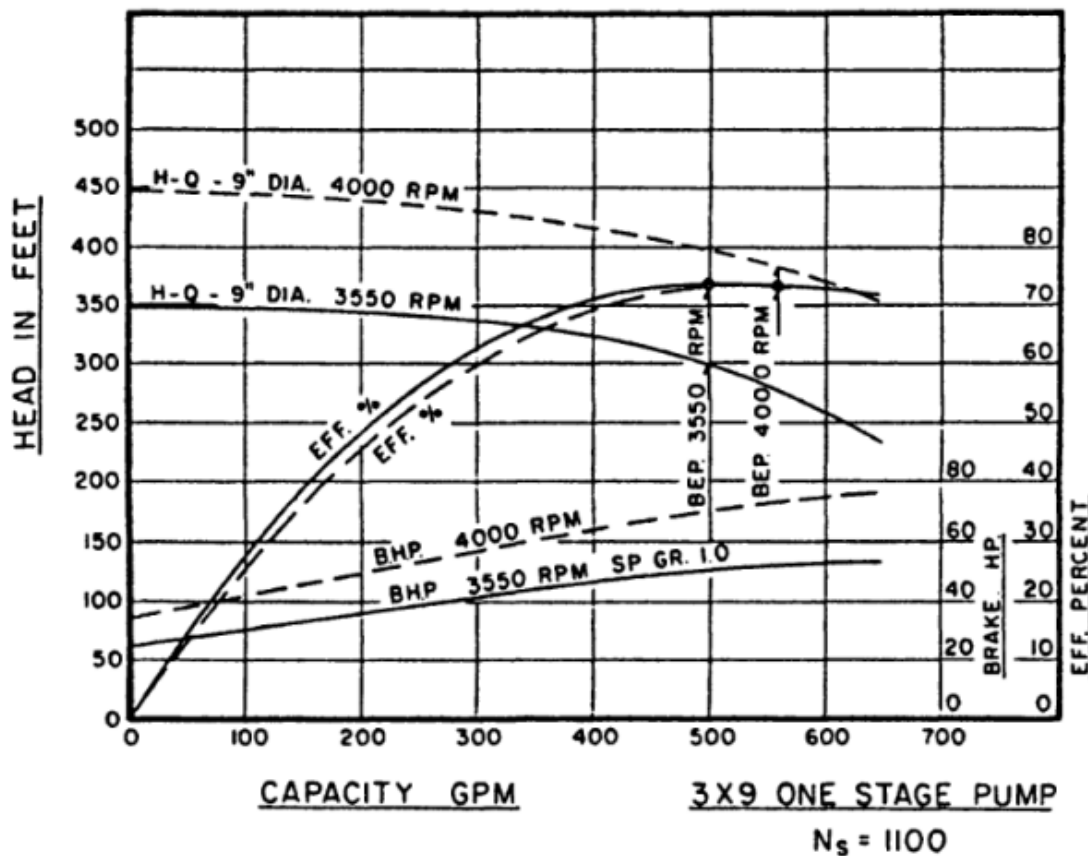
Figure 2.5. Schematic head-flow rate curve of a centrifugal pump. Taken from Lobanoff and Ross (1992), with permission.

The characteristic curve of a specific pump at a specific speed (such as that shown in Figure 2.5) can then be scaled using the pump affinity laws (Karassik, 2008; Talmon, 2016). As the flow rate is calculated as velocity of the fluid multiplied by the area, and the velocity of the fluid is proportional to the impeller rotational speed multiplied by the impeller radius, the pump affinity laws (or laws of

similitude) are as follows (Karassik, 2008; Simpson and Marchi, 2013; Talmon, 2016):

$$\frac{Q_1}{Q_2} = \frac{N_1}{N_2}$$

(2.17)

$$\frac{H_1}{H_2} = \left(\frac{N_1}{N_2}\right)^2$$

This gives rise to a series of characteristic pump curves, describing the relationship between head developed, and volumetric flow rate. These curves are provided by pump manufacturers and are derived by performing tests on the specific pump, at different speeds and efficiencies (Karassik, 2008; Talmon, 2016).

2.4.2 Dynamic models

Steady-state models are generally fit for purpose for the design phase of a DMS circuit, but due to changes in the process over time, dynamic modelling can provide much greater insight into the process as a whole (Napier-Munn, 2018; Scott, 2017), and are also necessary for the purposes of control, which require information on the evolution of variables over time in order to be effective (Meyer, 2015; Scott, 2017). Moreover, Napier-Munn et al. (1995) as well as Dardis (1989) both identified that medium losses often occur in short periods of time, in surging events. These events are not detectable by a steady-state model, hence the advantage of dynamic models.

2.4.2.1 Empirical dynamic models

Lyman et al. (1982) developed a dynamic model for a full DMS circuit in a coal processing plant, including the dense medium cyclone, correct and dilute medium tanks, drain-and-rinse screens, and magnetic separator. The model developed relied on several key assumptions:

- The dense medium cyclone was modelled as a pipe (as it was found to have negligible residence time).
- The correct and dilute medium tanks were modelled as variable volume plug flow devices.
- The drain-and-rinse screens were assumed to have ideal medium recovery on the rinse section. Rinse water rates were assumed as constant, and the volume of medium adhering to the coal from the drain section to the rinse section was calculated as a function of the coal surface area (Scott, 2017), and therefore did not consider medium properties (such as density and viscosity) or ore porosity in the adhesion of the medium.

- The magnetic separator was modelled using an empirically determined percentage recovery determined by the mass flow to the magnetic separator, as developed by Davis and Lyman (1983).

The focus of Lyman's work (Lyman et al., 1982) was on the density control, and was used to model various options for water addition locations into the correct medium circuit (Scott, 2017). The model also assumes a linear relationship between the medium density and the product coal ash content, which results in the model only being valid over a fairly narrow density band (Meyer, 2015). A further limitation is that the effect and behaviour of non-magnetic components in the medium was not considered, and the medium was rather modelled as a slurry of magnetite and water (Scott, 2017). Furthermore, the models of the individual units (dense medium cyclone, tanks, screens, etc) were simplified and required tuning parameters to fit to plant data (Lyman et al., 1982).

In 2017, with the benefit of more work having been done on steady-state models of various components (such as Clarkson and Wood (1993) and Rayner and Napier-Munn (2003a), described in Section 2.4.1), Scott (2017) developed another empirical dynamic model of the circuit. This model uses steady-state empirical models for individual units in an iterative loop, with the user able to select a run time of the simulation. In each iteration, the material balance in each unit is recalculated. Delays are also incorporated into the model.

Scott's dynamic model (Scott, 2017) utilised Wood's model (Clarkson and Wood, 1993) for the dense medium cyclone, Firth and O'Brien's model (Firth and O'Brien, 2010) for the drain-and-rinse screen, and Rayner's model (Rayner and Napier-Munn, 2003a,b) for the wet drum magnetic separators. The tanks in the circuit were modelled dynamically using the respective tank geometry. The mixing box (called the 'wing tank' in Scott (2017)) was also modelled using its geometry. The flow rate through the orifice of the mixing box was calculated as:

$$Q = Ca\sqrt{2gH} \qquad (2.18)$$

where Q is the volumetric flow rate out of the orifice of the mixing box, C is a constant dependent on the geometry of the orifice, a is the area of the orifice opening, g is the gravity constant, and H is the height of slurry in the mixing box. This relationship concurs with work done by Jang (2016) on gravity drained tanks (which the mixing box can be presumed to be, as slurry drains out of it, rather than being

pumped), which absorbs the constants C, a, and g in (2.18) into a lumped constant k such that:

$$Q = k\sqrt{H} \tag{2.19}$$

Scott's full DMS circuit model (Scott, 2017) therefore included most components of a typical DMS circuit: the desliming screen, the correct medium tank, the dense medium cyclone, the drain-and-rinse screens, the dilute medium tank and the magnetic separators. The model was verified with actual plant data from New Acland coal handling and preparation plant, and was found to acceptably predict plant behaviour.

2.4.2.2   First principles dynamic models

Meyer and Craig (2010) developed and verified a dynamic model of a coal preparation plant at Leeuwpan Colliery in South Africa, from first principles. As with Lyman's model (Lyman et al., 1982), and Scott's model (Scott, 2017), the model divided the circuit into specific units and developed individual models for each of these units.

The first unit considered is the medium water addition, which in the case of the Leeuwpan Colliery is in-line (as opposed to added to the correct medium tank). Water is therefore injected into the recovered medium line (which comes from the correct medium tank), and the corrected medium is taken to the mixing box. The principle of the conservation of overall mass was used to develop this model. The model assumes that the valve is linear with a constant pressure drop, and valve dynamics are neglected (and thus $Q_w = C_v \frac{l_p}{100} \sqrt{\frac{\Delta p}{1000}}$ is the flow rate of water through the valve). Using these assumptions, the following model was formed:

$$\frac{d\rho_{p,med}}{dt} = \frac{-Q_{p,med}}{V_p}\rho_{p,med} + \frac{1000K_p}{V_p}\frac{l}{100} + \frac{Q_{p,i}}{V_p}\rho_{p,i} \tag{2.20}$$

where Q_w is the volumetric flow rate of the water, C_v and l_p are the valve coefficient and position respectively, $K_p = C_v\sqrt{\frac{\Delta p}{1000}}$, Δ_p is the pressure drop over the valve, $\rho_{p,i}$ is the density of the recovered medium, $Q_{p,med}$ is the volumetric flow rate of the corrected magnetite medium, and V_p is the volume required until the solution is perfectly mixed.

The next unit considered by Meyer and Craig (2010) is the mixing box. Ore and medium is fed into the mixing box, and the slurry mixture then exits the mixing box. The principle of the conservation of overall mass was used to develop the model. The model assumes that the medium and ore feed is well-mixed in a constant mixing box volume, and that the volumetric flow rates of the correct medium into the mixing box and the slurry mix of medium ore are instantaneous before and after a step in the medium density or in the mass feed rate of the ore. Using these assumptions, the rate of change of

density of the slurry mix is:

$$\frac{d\rho_{mb}}{dt} = \frac{-Q_{mb}}{V_{mb}}\rho_{mb} + \frac{Q_{mb,med}}{V_{mb}}\rho_{mb,med} + \frac{1}{V_{mb}}W_{ore} \tag{2.21}$$

where ρ_{mb}, Q_{mb}, V_{mb} are the density, volumetric flow rate and volume of the mixing box respectively, $Q_{mb,med}$ and $\rho_{mb,med}$ are the volumetric flow rate and density of medium flow into the mixing box, and W_{ore} is the volumetric flow of ore into the mixing box. Unlike in Scott (2017) - see (2.18) - the flow rate of material out of the mixing box, Q_{MB}, is assumed known and thus not modelled.

The third unit considered by Meyer and Craig (2010) is the dense medium cyclone. Again, the conservation of overall mass is used, as well as the conservation of mass of individual components (such as ash percentage) of the coal product. For brevity, only the total mass flows will be detailed here (the individual component volumes and flow rates will not be explored). A diagram of this unit is shown in Figure 2.6.
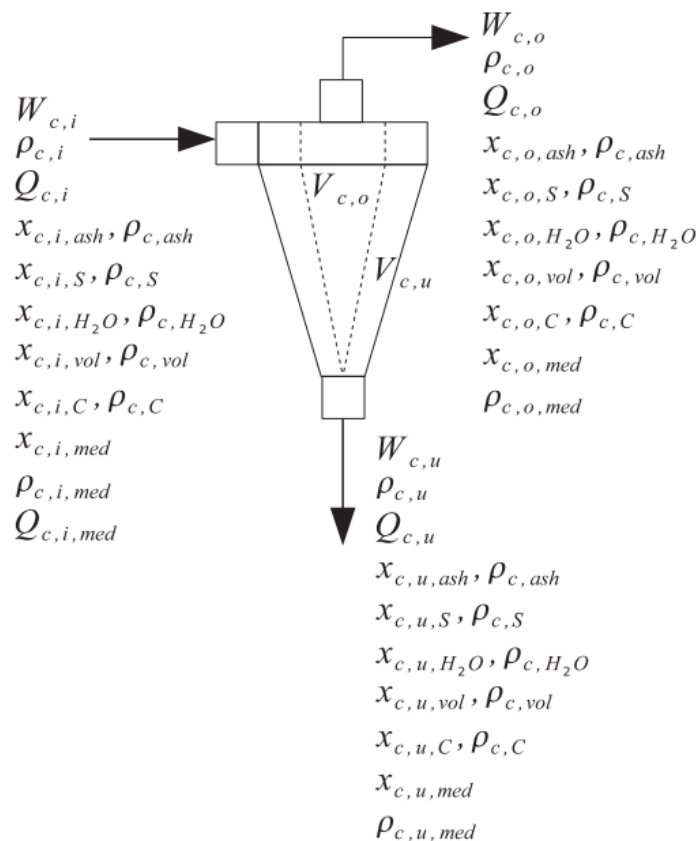
Figure 2.6. Diagram of the dense medium cyclone unit. Taken from Meyer and Craig (2010), with permission.

A number of assumptions were made in the formation of the model, and these have been listed here, along with comments on these assumptions as compared to others in the literature.

- The volume of the slurry in the cyclone is constant.

  This assumption is common to most models of the dense medium cyclone as seen in the literature, including the most commonly used steady-state models such as that in Clarkson and Wood (1993).

- The overflow and underflow volumes and volume flow rates of the cyclone are split at a constant ratio α.

  According to Wood's model, the volumetric flow split is affected by multiple factors, most notably the medium feed density (Clarkson and Wood, 1993). This was also noted by Scott (2017).

- The volumetric flow rates of the feed, overflow and underflow are constant before and after a step in the medium density or feed rate of the ore.

  Again, according to Wood's model (Clarkson and Wood, 1993), the volumetric flow rates are affected by a change in medium feed density as well as by a change in the feed rate of the ore.

- Only ash, sulphur, moisture, volatile, medium and fixed carbon components are considered for the conservation of mass components in the feed.

  Non-magnetics in the medium are not included in this list of components, and can have a large effect on the circuit (Scott, 2017). Additionally, this assumption of feed components to the dense medium cyclone is, of course, specific to a coal beneficiation circuit, and would need to be adapted for an iron ore application.

- The overflow and underflow mass rates of change are proportional to the difference in their respective densities to the medium density, the centrifugal force and the percentage of ash or carbon in the feed.

  This assumption agrees with Wood's model (Clarkson and Wood, 1993).

Following these assumptions, the following equation is obtained using the conservation of overall mass:

$$V_{c,o}\frac{d\rho_{c,o}}{dt} + V_{c,u}\frac{d\rho_{c,u}}{dt} = W_{c,i} - Q_{c,o}\rho_{c,o} - Q_{c,u}\rho_{c,u} \tag{2.22}$$

where $W_{c,i}$, $V_{c,o}$, $V_{c,u}$, $\rho_{c,o}$, $\rho_{c,u}$, $Q_{c,o}$, $Q_{c,u}$ are the cyclone inlet mass flow rate, and the cyclone overflow and underflow volumes, densities, and volumetric flow rates respectively.

To model the dynamics of the density response of the cyclone, the acceleration due to the centrifugal force was used, as it gives insight into the rates of change of mass in the overflow and underflow (which are proportional to their relative differences to the medium density):

$$V_{c,o}\frac{d\rho_{c,o}}{dt} = K_{c,o}(\rho_{c,i,med} - \rho_{c,o})x_{c,i,C} \tag{2.23}$$

$$V_{c,u}\frac{d\rho_{c,o}}{dt} = K_{c,u}(\rho_{c,i,med} - \rho_{c,u})x_{c,i,ash} \tag{2.24}$$

where $K_{c,o}$ and $K_{c,u}$ are the cyclone overflow and underflow proportionality constants, respectively. $\rho_{c,i,med}$ is the feed medium density, $x_{c,i,C}$ is the percentage carbon in the feed, and $x_{c,i,ash}$ is the percentage ash in the feed.

From (2.22) and (2.23), the overflow and underflow density differential equations can be developed. The same is done for each component of the feed, but as mentioned previously, for brevity these will not be repeated here.

The final unit considered by Meyer and Craig (2010) is the correct medium tank. As with Scott (2017), the tank geometry and the conservation of overall mass was used to model the behaviour of the tank.

Meyer and Craig (2010) did not model the medium recovery circuit (components such as the magnetic separator), but rather assumed that the recovery process was 100% efficient, and thus that no medium losses occurred. It should also be noted that Meyer and Craig (2010) did not include the medium drain-and-rinse screens. As mentioned in Section 2.3, medium recovery is not 100% efficient, and adhesion losses occur at the drain-and-rinse screens, when medium adheres to the underflow and overflow products of the cyclone (Dardis, 1989; Napier-Munn et al., 1995; Rayner and Napier-Munn, 2003a).

In work done to model the DMS circuit at Sishen Iron Ore Mine, Tom (2015) made use of Meyer and Craig (2010), and incorporated it into Wood's steady-state model of the dense medium cyclone (Clarkson and Wood, 1993), to produce a dynamic simulation of the circuit. In this work, the relationships derived by Meyer and Craig (2010) for a coal circuit were generalised to an iron ore

circuit, such that (2.23) and (2.24) become

$$V_{c,o}\frac{d\rho_{c,o}}{dt} = K_{c,o}(\rho_{c,i,med} - \rho_{c,o})x_{c,i,waste} \qquad (2.25)$$

$$V_{c,u}\frac{d\rho_{c,o}}{dt} = K_{c,u}(\rho_{c,i,med} - \rho_{c,u})x_{c,i,product} \qquad (2.26)$$

Tom (2015) included dynamic modelling of the dense medium cyclone and the correct medium tank, and did not model the drain-and-rinse screens, and also neglected the medium recovery process.

2.4.2.3 Pump dynamic models

The dynamic models of the DMS circuit surveyed in Sections 2.4.2 and 2.4.2.2 do not include modelling of the circuit pumps, as the flow rate within the circuit are assumed known. For the circuit studied in this work, the flow rates are not measured, and so it is necessary to review pump models in the literature.

While pumps are extensively studied in steady-state (see Section 2.4.1.5), less work is reported on modelling pumps dynamically. Kallesoe et al. (2006) presents a dynamic model of a pump system, for the purposes of model based fault detection. The system is defined such that:

$$\dot{x} = f(x) + Gu + m(x,d) \qquad (2.27)$$

$$y = h(x)$$

with the state vector as $x = \begin{bmatrix} i_{sd} & i_{sq} & \psi_{rd} & \psi_{rq} & \omega_r & Q \end{bmatrix}^T$, where i_{sd} and i_{sd} are the motor currents, ψ_{rd} and ψ_{rd} are the rotor fluxes, ω_r is the rotational speed of the pump, and Q is the volumetric flow rate through the pipe.

The input and disturbance vectors are $u = \begin{bmatrix} v_{sd} & v_{sq} \end{bmatrix}^T$, and $d = \begin{bmatrix} p_{in} & K_v \end{bmatrix}^T$, where v_{sd} and v_{sq} are the motor supply voltages, p_{in} is the inlet pressure and K_v, which is the valve opening. The output vector of the system is $y = \begin{bmatrix} i_{sd} & i_{sq} & H \end{bmatrix}^T$.

In the work by Kallesoe et al. (2006), the head $f_H(Q, \omega_r)$ and torque $f_T(Q, \omega_r)$ produced by the pump is modelled as follows:

$$f_H(Q, \omega_r) = -a_{h2}Q^2 + a_{h1}Q\omega_r + a_{h0}\omega_r^2 \qquad (2.28)$$

$$f_T(Q, \omega_r) = -a_{t2}Q^2 + a_{t1}Q\omega_r + a_{t0}\omega_r^2 \qquad (2.29)$$

where a_{h2}, a_{h1}, a_{h0} and a_{t2}, a_{t1}, a_{t0} are constant parameters from the physical properties of the pump. The quadratic form of these equations agrees with the steady-state models described in Section 2.4.1.5. Using the equations for the pressure and torque of the pump, given in (2.28) and (2.29) respectively, the model of the pump is formed such that f, G, m and h in (2.27) are as follows:

$$f(\boldsymbol{x}) = \begin{bmatrix} -\frac{R'_s}{L'_s}i_{sd} + \frac{L_m}{L'_s L_r}(R'_r \psi_{rd} + z_p \omega_r \psi_{rq}) \\ -\frac{R'_s}{L'_s}i_{sq} + \frac{L_m}{L'_s L_r}(R'_r \psi_{rq} + z_p \omega_r \psi_{rd}) \\ -(R'_r \psi_{rd} + z_p \omega_r \psi_{rq}) + R'_r L_m i_{sd} \\ -(R'_r \psi_{rq} + z_p \omega_r \psi_{rd}) + R'_r L_m i_{sq} \\ 1.5\frac{1}{J}z_q \frac{L_m}{L_r}(\psi_{rd}i_{sq} - \psi_{rq}i_{sd}) - \frac{B}{J}\omega_r - \frac{1}{J}f_T(Q,\omega_r) \\ \frac{1}{K_J}f_H(Q,\omega_r) - \frac{1}{K_J}(p_{out} + \rho g(z_{out} - z_{in})) - \frac{K_t}{K_J}Q^2 \end{bmatrix} \tag{2.30}$$

$$G = \begin{bmatrix} \frac{1}{L'_s} & 0 \\ 0 & \frac{1}{L'_s} \\ 0 & 0 \\ 0 & 0 \\ 0 & 0 \\ 0 & 0 \end{bmatrix} \qquad m(\boldsymbol{x},\boldsymbol{d}) = \begin{bmatrix} 0 \\ 0 \\ 0 \\ 0 \\ 0 \\ \frac{1}{K_J}p_{in} - \frac{K_v}{K_J}Q^2 \end{bmatrix} \tag{2.31}$$

$$h(\boldsymbol{x}) = \begin{bmatrix} i_{sd} \\ i_{sq} \\ f_H(Q,\omega_r) \end{bmatrix} \tag{2.32}$$

Ghafouri et al. (2012) then expanded on this work done by Kallesoe et al. (2006), also for the purposes of fault detection. The work modelled all aspects of the pump system: the three phase motor, the mechanical pump system, and the hydraulic application.

2.5   DMS AND MEDIUM LOSSES CONTROL

There has been significant work in the literature on the control of the DMS circuit in general, with work exploring the automation of the circuit, as well as focused on control of the yield and quality optimisation of the product. There is little work reported in the literature on online control of the medium, and none on the reduction of losses through online control, although there has been much focus on reducing losses through design and operational means.

2.5.1   Automation

Tom (2015), in work on the Sishen Iron Ore Mine in South Africa, implemented automation of a number of sub-processes in the cyclone DMS circuits. This was not for the purposes of online process control in the true sense, but rather involved monitoring various parameters (such as cyclone inlet pressure), and implementing automated warnings to operators when these parameters were outside the optimal range. In the case of the correct medium tank level, an interlock was introduced to stop the circuit when the level went below a certain value, to ensure circuit stability. Additionally, a 'soft-sensor' was developed to monitor the medium to feed ratio, and alert the operator when this was out of the recommended range. The cyclone overflow and underflow density was also measured online (with newly installed densitometers), and this resulted in better insight into the operation of the circuit, and the detection of abnormalities.

2.5.2   Yield control

Yield is defined as the percentage of the feed to a DMS circuit that is produced as product from the dense medium cyclone (Maré et al., 2015). As such, it is a good candidate for control as it directly affects the profitability of a plant: a small increase in yield at high feed tonnages can result in a significant increase in product (Tom, 2015).

Meyer (2015), using the work done by Meyer and Craig (2010) to model the DMS circuit (explored extensively in Section 2.4.2), developed a nonlinear model predictive controller (NMPC) to maximise the yield of a coal DMS circuit, while ensuring that the ash content of the product did not exceed a certain maximum defined by the plant's client. The density setpoint of the circuit was used to achieve this. The objective function of the NMPC was therefore to maximise the yield while keeping the ash content as close as possible to an input target value. The NMPC was not tested on an actual plant; however the model was validated using real plant data, and the simulation results with the NMPC showed a yield increase of 5.1% and ash content decrease of 0.4% through the use of the controller.

Zhang and Xia (2014) produced a similar NMPC, this time focused on optimising the percentage of carbon in the product (ie. the quality of the product), while reducing the energy costs of the circuit, again manipulating the density setpoint to achieve this. The pumping effort of the correct medium pump (which pumps correct medium to the mixing box) was assumed to be the main energy consumer of the circuit, and this was stated to be a linear function of the medium density. Thus the objective

function of the NMPC was to optimise the percentage of fixed carbon, by keeping it as close to the desired value as possible, while minimising the density setpoint of the circuit. Feedforward information, by means of the quality of the feed to the circuit, was also used in the control. Again, the NMPC was not tested on a live plant, but showed significant improvement in quality in simulations.

2.5.3 Medium losses control

There is a fair amount of literature available on the reduction of medium losses through design means. Dardis (1989) investigated and reported on trends in DMS circuit design as they pertain to the reduction of medium losses. These include introducing recycle circuits, in which, during medium dosing (where fresh medium is dosed into the correct medium tank), the magnetic separator effluent is returned to the dilute medium tank, so that the effluent is processed multiple times during medium make-up, where the feed density to the magnetic separator is above the supplier recommendation. Dardis (1989) also investigated magnetic separator settings and their effect on losses, and found that the pulp height, magnetic position and drum speed have a significant effect on the recovery. Rayner, in work done to model magnetic separators (Rayner and Napier-Munn, 2003a,b), concurred with Dardis (1989) on the effect of these parameters.

In terms of online medium control, O'Brien et al. (2016) investigated a coal plant in Australia. While not specifically focused on medium losses, the work gives insight into control of medium density, stability and quantity of the medium. Through studies of the plant, significant changes in the underflow density were detected, which were attributed to a lack of control of non-magnetics in the medium, in turn contributing to stability issues of the medium. This is because instability in the medium increases the separation size and the partition E_p, which results in significant changes in the underflow density of the cyclone. O'Brien et al. (2016) therefore concluded that the controlled addition of non-magnetics into the circuit could be beneficial as it has a marked effect on the stability of the medium. Additionally, it was found that the overflow and underflow densities of the cyclone need to be monitored, as this indicates the quality of the medium in the circuit. This concurred with work done by Tom (2015), mentioned in Section 2.5.1, which also investigated the benefits of monitoring the underflow and overflow densities of the cyclone. The general observation was also made by O'Brien et al. (2016) that medium quality is not actively controlled or monitored, and as such stability issues can go unnoticed by operational teams, until it is picked up in quality problems in the product of the circuit, or in events such as surging.

2.6 CONCLUSION

The aim of this chapter is to review the literature on the DMS circuit, with specific focus on the modeling and detection of medium losses within the circuit. There is consensus in the literature that medium losses can occur at two points in the circuit: adhered to the product and tails that are passed out the circuit over the drain-and-rinse screens, and in the effluent of the magnetic separator. These medium losses can contribute between 20% and 39% of the total running costs of a DMS circuit (Dardis, 1989). Many authors have worked to model the DMS circuit and its components, with steady-state models receiving much attention in the literature, and dynamic models less attention. While medium behaviour was included in most models explored here, no work that specifically focused on the detection of medium losses using models developed has been reported in the literature. Much work has been done on the control of the DMS circuit. This ranges from automation of various elements of the circuit, with the intent to stabilise the operation of the circuit, to NMPC aimed at improving the quality of the product while either maximising yield or reducing energy consumption. Again, the literature lacks work focused on the reduction of medium losses in the circuit, although there is consensus amongst various authors that increasing screen velocity of the drain-and-rinse screens and minimising the operating density decreases medium losses.

CHAPTER 3   MODEL DEVELOPMENT

3.1   CHAPTER OVERVIEW

In this chapter, a full model of the DMS circuit is developed, for the purposes of simulation. In Section 3.2 the DMS circuit is first divided into individual units, namely the circuit tanks (correct medium, secondary and dilute medium tanks), the mixing box, the primary and secondary densifiers, the dense medium cyclone and drain-and-rinse screens, and the magnetic separator. In Section 3.3, a model for the circuit pumps is presented. This is then incorporated into models developed for the correct medium, secondary and dilute medium tanks in Sections 3.4, 3.5, and 3.6 respectively. In Sections 3.7, 3.8, 3.9 and 3.10, a model for the remaining units (the mixing box, dense medium cyclone and drain-and-rinse screens, primary and secondary densifiers, and the magnetic separator) is presented.

3.2   CIRCUIT UNITS

In order to model the DMS circuit of the plant studied in this dissertation (seen in Figure 1.1), the circuit must be divided into units which can then be modelled separately. For this work, the circuit is divided into the following individual units:

(i) Correct medium tank - comprising of the correct medium tank, correct medium pump, and primary densifier pump

(ii) Secondary tank - comprising of the secondary tank and secondary densifier pump

(iii) Dilute medium tank - comprising of the dilute medium tank, dilute medium pump, and dilute medium tank water addition valve

(iv) Mixing box

(v) DMC + drain-and-rinse screens - comprising of the dense medium cyclone, and the product and waste drain-and-rinse screens

(vi) Primary densifier

(vii) Secondary densifier

(viii) Magnetic separator

The division of the circuit into the individual units is illustrated in Figure 3.1.
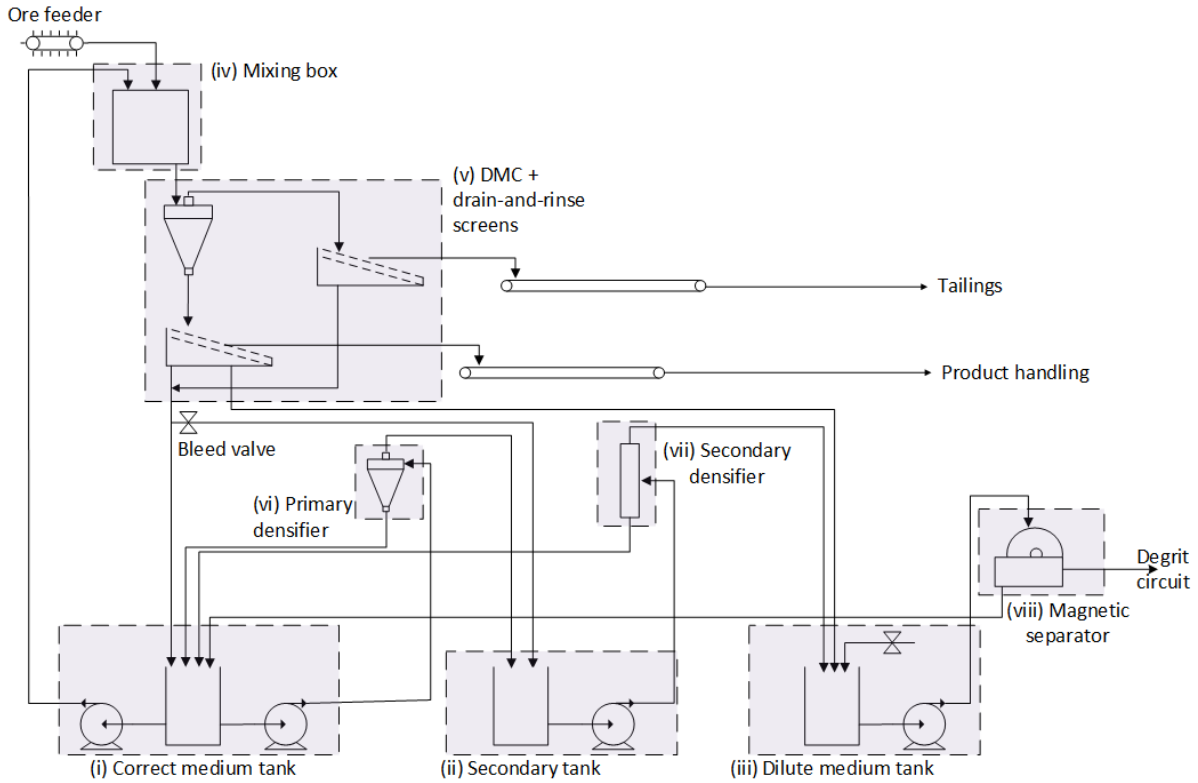
Figure 3.1. Diagram of a dense medium separation circuit at an iron ore plant, with individual units highlighted.

These individual units are modelled individually. The model units are presented in state-space as:

$$
\begin{aligned}
\dot{\boldsymbol{x}} &= f(t,\boldsymbol{x},\boldsymbol{u},\boldsymbol{d}) \\
\boldsymbol{y} &= g(t,\boldsymbol{x},\boldsymbol{u},\boldsymbol{d}),
\end{aligned}
\tag{3.1}
$$

where $\boldsymbol{x} \in \Re^{n_x}$, $\boldsymbol{u} \in \Re^{n_u}$, $\boldsymbol{d} \in \Re^{n_d}$ and $\boldsymbol{y} \in \Re^{n_y}$ are the model states, inputs, process disturbances and measured outputs respectively. The unit models are then combined into a model of the full circuit, on simulation platform Simulink.

3.3   PUMP MODELS

For the circuit tank models, a general model for the pumps used in the circuit shown in Figure 3.1 is required. For each pump, the flow rate is not measured and only the pump speed is known. Furthermore,

for this work, the principle of the conservation of volume is used. It is assumed that the material flows are similar to liquids and consequently incompressible. The pump speed, discharge flow rate and discharge pressure are measured variables. Only the hydraulic part of the pump is modelled.

3.3.1   Pump characteristic curves

The pump characteristic curves, provided by the pump manufacturers, gives an indication of the relationship between total dynamic head, and the volumetric flow rate produced by a pump, at a specific speed. Figure 3.2 gives an example of the characteristic curve for a pump with a maximum speed of 4000 rpm.
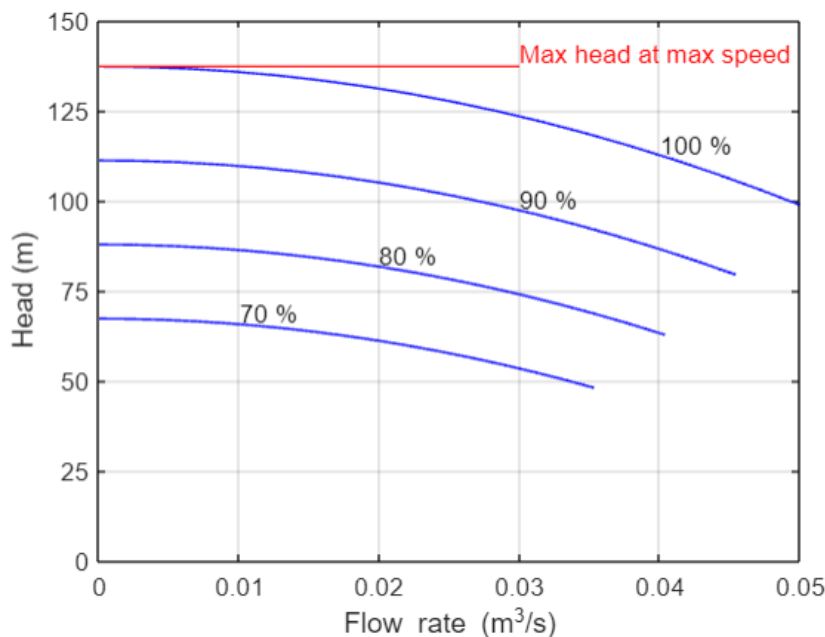
Figure 3.2. Characteristic pump curves for a centrifugal pump. The curves are given as percentages of the maximum speed. Adapted from Lobanoff and Ross (1992), with permission.

The curves in Figure 3.2 can be fitted to a quadratic function over normal operating ranges for a specific pump speed. Furthermore, according to the pump affinity laws, the head developed by a pump at zero flow rate is proportional to the square of the speed of the pump (Karassik, 2008). The respective curves at all speeds can therefore be constructed as follows:

$$H_p = H_{max}n^2 - SQ^2, \tag{3.2}$$

where H_p [m] is the pump head, H_{max} [m] is the maximum head when there is no flow and the pump is at maximum speed, n is the ratio of the current speed to the maximum speed of the pump, S [s^2/m^5]

is the curve parameter obtained from the pump curves, and Q [m^3/s] is the volumetric flow rate of slurry.

3.3.2   Discharge pressure

The pump characteristic curves, while determined from measurements by the suppliers, arise from Bernoulli's equation (Karassik, 2008) which asserts that the combination of pressure and the sum of kinetic and potential energy is constant over time and along a stream. Therefore, the total head developed by a pump at a specific speed is defined as:

$$H_{max}n^2 = \frac{P}{\rho g} + \frac{Q^2}{2gA^2} + h, \tag{3.3}$$

where P [kPa] is the pump discharge pressure, ρ [t/m^3] is the density of the pumped slurry, g [m/s^2] is the gravitational acceleration constant, A [m^2] is the cross-sectional area of the discharge pipe, and h [m] is the total static head. From (3.3), the discharge pressure can be written as:

$$P = \rho g \left(H_{max}n^2 - \frac{Q^2}{2gA^2} - h \right), \tag{3.4}$$

where the static head $h = h_{dis} - h_{lev}$ can be expressed in terms of the height to which the slurry is pumped (h_{dis}) and the height of slurry in the tank (h_{lev}).

3.4   CORRECT MEDIUM TANK MODEL

The correct medium tank in Figure 1.1 is redrawn in Figure 3.3. The correct medium tank unit consists of the tank, with two pumps pumping slurry: the correct medium pump (which pumps medium to the mixing box), and the primary densifier pump (which pumps medium to the primary densifier). It is assumed that the material flows are similar to liquids and consequently incompressible.
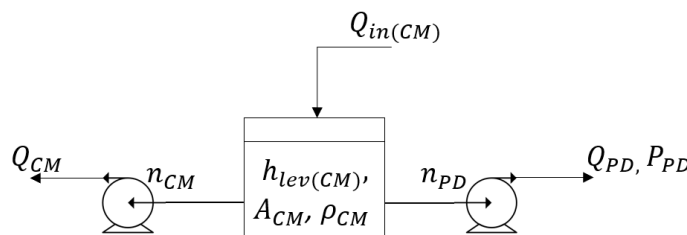
Figure 3.3. Correct medium tank unit.

In Figure 3.3 $h_{lev(CM)}$ is the height of correct medium in the tank, A_{CM} is the cross-sectional area of the tank, ρ_{CM} is the density of slurry in the tank, $Q_{in(CM)}$ is the sum of the volumetric flow of medium returned to the correct medium tank, Q_{CM} and Q_{PD} are the volumetric flows of correct medium tank being pumped out by the correct medium pump and the primary densifier pump respectively, n_{CM} and

n_{PD} are the speed fractions of the correct medium and primary densifier pumps respectively, and P_{PD} is the discharge pressure of the primary densifier pump. The density of the slurry in the correct medium tank is considered well-mixed, and so the density of the medium tank inflow, ρ_{in}, is not considered in the model. Note that the quantities Q_{CM} and Q_{PD} will need to be modelled from the speeds of the correct medium and primary densifier pumps respectively.

Table 3.1 describes the process variables in terms of measured and unmeasured variables, where subscript CM refers to the correct medium and PD refers to the primary densifier.

<p align="center">**Table 3.1.** Correct medium tank model variables.</p>

Variable	Unit	Description
	Measured at the plant	
$h_{lev(CM)}$	m	Correct medium tank level
P_{PD}	kPa	Primary densifier pump pressure
n_{CM}	-	Correct medium pump speed
n_{PD}	-	Primary densifier pump speed
ρ_{CM}	t/m^3	Density of slurry in correct medium tank
	Not measured at the plant	
Q_{CM}	m^3/s	Correct medium pump flow rate
Q_{PD}	m^3/s	Primary densifier pump flow rate
P_{CM}	kPa	Correct medium pump pressure
$Q_{in(CM)}$	m^3/s	Flow into correct medium tank

The dynamics of the level of the correct medium tank can be obtained using the principle of the conservation of volume. Therefore:

$$\frac{dh_{lev(CM)}}{dt} = \frac{1}{A_{CM}}\left(Q_{in(CM)} - Q_{CM} - Q_{PD}\right),\tag{3.5}$$

where Q_{CM} and Q_{PD} are the volumetric flow rates of the correct medium pump and the primary densifier pump respectively, and A_{CM} is the cross-sectional area of the correct medium tank. These

volumetric flow rates are modelled as (Kallesoe et al., 2006):

$$\frac{dQ_{CM}}{dt} = \frac{1}{k_{j(CM)}}\left(\rho_{CM}g(H_{p(CM)} - (h_{dis(CM)} - h_{lev(CM)})) - k_p Q_{CM}^2\right) \tag{3.6}$$

$$\frac{dQ_{PD}}{dt} = \frac{1}{k_{j(PD)}}\left(\rho_{CM}g(H_{p(PD)} - (h_{dis(PD)} - h_{lev(CM)})) - k_p Q_{PD}^2\right), \tag{3.7}$$

where k_p is the resistance coefficient of the pipe, $k_{j(CM)}$ and $k_{j(PD)}$ [t m^2] are the inertia of the fluid for the correct medium tank and primary densifier respectively, and $H_{p(CM)}$ and $H_{p(PD)}$ are given by (3.2) adapted for the respective pumps:

$$H_{p(CM)} = H_{max(CM)}n_{CM}^2 - S_{CM}Q_{CM}^2, \tag{3.8}$$

$$H_{p(PD)} = H_{max(PD)}n_{PD}^2 - S_{PD}Q_{PD}^2$$

Using (3.2), (3.4), (3.5), (3.6), and (3.7), the full model for the correct medium tank system can be formed. The model states are the level of slurry in the tank, $h_{lev(CM)}$, the flow produced by the correct medium pump Q_{CM}, and the flow produced by the primary densifier pump Q_{PD}:

$$\boldsymbol{x}_{CM} = \begin{bmatrix} h_{lev(CM)} & Q_{CM} & Q_{PD} \end{bmatrix}^T. \tag{3.9}$$

The inputs to the model are the speeds of the correct medium and primary densifier pumps (n_{CM} and n_{PD} respectively), as ratios to their respective maximum speeds:

$$\boldsymbol{u}_{CM} = \begin{bmatrix} n_{CM} & n_{PD} \end{bmatrix}^T. \tag{3.10}$$

The density of the slurry in the tank ρ_{CM} is measured, and included as an uncontrolled disturbance. Note that while the flow of material into the tank, $Q_{in(CM)}$, is not measured in the plant (as seen in Table 3.1), it is measured in the simulation. For the simulation model, it is therefore included as a measured process disturbance. Similarly, ρ_{CM} is measured, but is an uncontrolled disturbance:

$$\boldsymbol{d}_{CM} = \begin{bmatrix} \rho_{CM} & Q_{in(CM)} \end{bmatrix}^T. \tag{3.11}$$

The model outputs, which are available for measurement, are the height of slurry in the correct medium tank, $h_{lev(CM)}$, and the discharge pressure of the primary densifier pump, P_{PD}. Note that the correct medium pump discharge pressure is not measured and so, while the primary densifier pump pressure (measured) is included as an output, the correct medium pump pressure is not:

$$\boldsymbol{y}_{CM} = \begin{bmatrix} h_{lev(CM)} & P_{PD} & \rho_{CM} \end{bmatrix}^T. \tag{3.12}$$

A state-space model of the correct medium tank is therefore:

$$\dot{\boldsymbol{x}}_{CM} = f_{CM}(t, \boldsymbol{x}_{CM}, \boldsymbol{u}_{CM}, \boldsymbol{d}_{CM}) \tag{3.13}$$

$$= \begin{bmatrix} \frac{1}{A_{CM}} \left(Q_{in(CM)} - Q_{CM} - Q_{PD} \right) \\ \frac{1}{k_{j(CM)}} \left(\rho_{CM} g (H_{p(CM)} - h_{dis(CM)} + h_{lev(CM)}) - k_p Q_{CM}^2 \right) \\ \frac{1}{k_{j(PD)}} \left(\rho_{CM} g (H_{p(PD)} - h_{dis(PD)} + h_{lev(CM)}) - k_p Q_{PD}^2 \right) \end{bmatrix},$$

$$\boldsymbol{y}_{CM} = g_{CM}(t, \boldsymbol{x}_{CM}, \boldsymbol{u}_{CM}, \boldsymbol{d}_{CM}) \tag{3.14}$$

$$= \begin{bmatrix} h_{lev(CM)} \\ \rho_{CM} g \left(H_{max(PD)} n_{PD}^2 - \frac{Q_{PD}^2}{2A_{PD}^2 g} - h_{dis(PD)} + h_{lev(CM)} \right) \\ \rho_{CM} \end{bmatrix}.$$

Table 3.2 shows the values of the parameters required for the model. Note that $H_{max(CM)}$, $H_{max(PD)}$, S_{CM}, and S_{PD} are obtained from the manufacturer provided pump curve at the given maximum speeds of the pumps. Parameters $k_{j(CM)}$ and $k_{j(PD)}$ are functions of the measured density of the fluid ρ_{CM}, as well as the length and cross-sectional area of the correct medium and primary densifier pumps' discharge pipes, respectively.

Table 3.2. Correct medium tank model parameters.

Variable	Value	Description
$H_{max(CM)}$	34.5 m	Maximum head of correct medium pump
$H_{max(PD)}$	17.0 m	Maximum head of primary densifier pump
S_{CM}	0.072 s^2/m^5	Quadratic term of correct medium pump curve
S_{PD}	0.36 s^2/m^5	Quadratic term of primary densifier pump curve
$k_{j(CM)}$	961 t·m^2	Hydraulic inertia of fluid for correct medium pump
$k_{j(PD)}$	721 t · m^2	Hydraulic inertia of fluid for primary densifier pump
A_{CM}	8 m^2	Cross-sectional area of correct medium tank
k_p	140	Resistance coefficient of pipe (steel)
A_{PD}	0.011 m^2	Area of primary densifier pump pipe
$h_{dis(CM)}$	10.83 m	Height slurry is pumped to by correct medium pump
$h_{dis(PD)}$	4.5 m	Height slurry is pumped to by primary densifier pump

3.5   SECONDARY TANK MODEL

The secondary tank shown in Figure 1.1 is redrawn in Figure 3.4. It can be modelled very similarly to the correct medium tank. The model is in fact simpler, as the secondary tank has only one pump extracting slurry to pump it to the secondary densifier.

Figure 3.4. Secondary tank unit.

Table 3.3 describes the process variables for the secondary tank in terms of measured and unmeasured variables, where subscript SD refers to the secondary densifier.

Table 3.3. Secondary tank model variables.

Variable	Unit	Description
Measured at the plant		
$h_{lev(sec)}$	m	Secondary tank level
P_{SD}	kPa	Secondary densifier pump pressure
n_{SD}	-	Secondary densifier pump speed
ρ_{sec}	t/m^3	Density of slurry in secondary tank
Not measured at the plant		
Q_{SD}	m^3/s	Secondary densifier pump flow rate
$Q_{in(sec)}$	m^3/s	Flow into secondary tank

As with the correct medium tank, the total flow into the secondary tank, $Q_{in(sec)}$, is not measured in the plant, but is measured in the simulation (as it is the sum of outputs from other units). Therefore, for the simulation model developed in this chapter, it is modelled as a measured uncontrolled disturbance. The density, ρ_{sec}, is measured both in the plant and in the simulation, and is therefore also included as

a measured uncontrolled disturbance. A state-space model for the secondary tank is:

$$\dot{\boldsymbol{x}}_{sec} = f_{sec}(t, \boldsymbol{x}_{sec}, \boldsymbol{u}_{sec}, \boldsymbol{d}_{sec}) \tag{3.15}$$

$$= \begin{bmatrix} \frac{1}{A_{sec}} \left(Q_{in(sec)} - Q_{SD} \right) \\ \frac{1}{k_{j(SD)}} \left(\rho_{sec} g (H_{p(SD)} - h_{dis(SD)} + h_{lev(sec)}) - k_p Q_{SD}^2 \right) \end{bmatrix}$$

$$\boldsymbol{y}_{sec} = g_{sec}(t, \boldsymbol{x}_{sec}, \boldsymbol{u}_{sec}, \boldsymbol{d}_{sec}) \tag{3.16}$$

$$= \begin{bmatrix} h_{lev(sec)} \\ \rho_{sec} g \left(H_{max(SD)} n_{SD}^2 - \frac{Q_{SD}^2}{2 A_{SD}^2 g} - h_{dis(SD)} + h_{lev(sec)} \right) \\ \rho_{sec} \end{bmatrix},$$

where $\boldsymbol{x}_{sec} = \begin{bmatrix} h_{lev(sec)} & Q_{SD} \end{bmatrix}^T$, $\boldsymbol{u}_{sec} = n_{SD}$, $\boldsymbol{d}_{sec} = \begin{bmatrix} \rho_{sec} & Q_{in(sec)} \end{bmatrix}^T$, and $\boldsymbol{y}_{sec} = \begin{bmatrix} h_{lev(sec)} & P_{SD} & \rho_{sec} \end{bmatrix}^T$. Note that $H_{p(SD)}$ is obtained from (3.2) applied to the secondary densifier pump.

Table 3.4 shows the values of the parameters required for the model. Note that $H_{max(SD)}$ and S_{SD} are obtained from the manufacturer provided pump curve at the given maximum speed of the pump. Parameter $k_{j(SD)}$ is a function of the measured density of the fluid, ρ_{sec}, as well as the length and cross-sectional area of the secondary densifier pump discharge pipe.

Table 3.4. Secondary tank model parameters.

Variable	Value	Description
$H_{max(SD)}$	32.1 m	Maximum head of secondary densifier pump
S_{SD}	0.324 s^2/m^5	Quadratic term of secondary densifier pump curve
$k_{j(SD)}$	721 t · m^2	Hydraulic inertia of fluid for secondary densifier pump
A_{sec}	2.73 m^2	Cross-sectional area of secondary tank
k_p	140	Resistance coefficient of steel pipe
$h_{dis(SD)}$	11 m	Height slurry is pumped to by secondary densifier pump
A_{SD}	0.011 m^2	Area of secondary densifier pump pipe

3.6   DILUTE MEDIUM TANK

The dilute medium tank in Figure 1.1 is redrawn in Figure 3.5. The model differs from the secondary tank model, as the discharge pressure of the dilute medium tank is not measured. Furthermore, water is added to the dilute medium tank via a control valve.
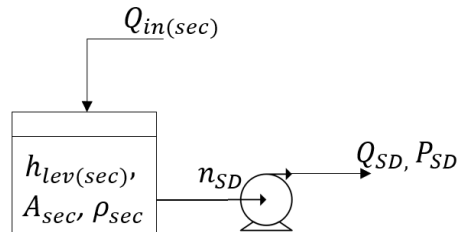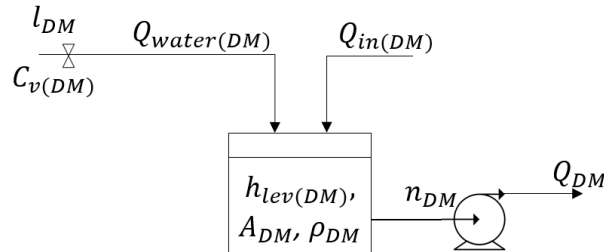

Figure 3.5. Dilute medium tank unit.

Table 3.5 describes the process variables for the dilute medium tank in terms of measured and unmeasured variables, where subscript DM refers to the dilute medium tank.

Table 3.5. Dilute medium tank model variables.

Variable	Unit	Description
		Measured at the plant
$h_{lev(DM)}$	m	Dilute medium tank level
n_{DM}	-	Dilute medium pump speed
l_{DM}	-	Dilute medium tank water valve opening
		Not measured at the plant
Q_{DM}	m³/s	Dilute medium pump flow rate
P_{DM}	kPa	Dilute medium pump pressure
$Q_{water(DM)}$	m³/s	Water addition via water valve to dilute medium tank
$Q_{in(DM)}$	m³/s	Flow of slurry into dilute medium tank
ρ_{DM}	t/m³	Density of slurry in dilute medium tank

The flow rate of water through the control valve ($Q_{water(DM)}$) is modelled as:

$$Q_{water(DM)} = C_v f(l_{DM}) \sqrt{\frac{\Delta P_v}{g_s}}, \tag{3.17}$$

where C_v [m^3/s] is the valve size coefficient supplied by manufacturers, ΔP_v [kPa] is the pressure drop across the valve, g_s is the liquid specific gravity of the fluid, and l_{DM} is the fraction opening of the valve bound between 0 (fully closed) and 1 (fully opened). The function $f(l_{DM})$ is dependent on the control valve characteristic curve, that is, if it is fast opening, linear or equal percentage (Seborg et al., 2016). For this work, it is assumed that the pressure drop across the valve, ΔP_v is constant, while the specific gravity g_s is known to be constant (and equal to 1). Therefore, the $\sqrt{\frac{\Delta P_v}{g_s}}$ term is therefore absorbed with the coefficient $C_{v(DM)}$ into coefficient k_v. Furthermore, the valve is assumed to be linear. Therefore (3.17) is simplified as:

$$Q_{water(DM)} = k_v l_{DM}, \tag{3.18}$$

A state-space model of the dilute medium tank is:

$$\dot{x}_{DM} = f_{DM}(t, x_{DM}, u_{DM}) \tag{3.19}$$

$$= \begin{bmatrix} \frac{1}{A_{DM}} \left(Q_{in(DM)} - Q_{DM} + k_v l_{DM} \right) \\ \frac{1}{k_{j(DM)}} \left(\rho_{DM} g (H_{p(DM)} - h_{dis(DM)} + h_{lev(DM)}) - k_p Q_{DM}^2 \right) \end{bmatrix}$$

$$y_{DM} = g_{DM}(t, x_{DM}, u_{DM}) \tag{3.20}$$

$$= h_{lev(DM)},$$

with $x_{DM} = \begin{bmatrix} h_{lev(DM)} & Q_{DM} \end{bmatrix}^T$, $u_{DM} = \begin{bmatrix} n_{DM} & l_{DM} \end{bmatrix}^T$, $d_{DM} = \begin{bmatrix} \rho_{DM} & Q_{in(DM)} \end{bmatrix}^T$, and $y_{DM} = h_{lev(DM)}$. Note that $H_{p(DM)}$ is obtained from (3.2) applied to the dilute medium pump.

As with the correct medium and secondary tanks, the total flow into the dilute medium tank, $Q_{in(DM)}$, is not measured in the plant, but is measured in the simulation (as it is the sum of outputs from other units). Therefore, for the simulation model developed in this chapter, it is modelled as a measured uncontrolled disturbance.

Table 3.6 shows the values of the parameters required for the model. Note that $H_{max(DM)}$ and S_{DM} are obtained from the manufacturer provided pump curve at the given maximum speed of the pump. Parameter $k_{j(DM)}$ is a function of the density of the fluid ρ_{DM}, as well as the length and cross-sectional area of the dilute medium pump discharge pipe.

Table 3.6. Dilute medium tank model parameters.

Variable	Value	Description
$H_{max(DM)}$	5.14 m	Maximum head of dilute medium pump
S_{DM}	0.36 s^2/m^5	Quadratic term of dilute medium pump curve
$k_{j(DM)}$	481 t · m^2	Hydraulic inertia of fluid for dilute medium pump
A_{DM}	4.13 m^2	Cross-sectional area of dilute medium tank
k_p	140	Resistance coefficient of pipe (steel)
$h_{dis(DM)}$	3.4 m	Height slurry is pumped to by dilute medium pump
k_v	unknown	Dilute medium water valve combined coefficient

3.7   MIXING BOX

The mixing box system depicted in Figure 1.1 is redrawn in Figure 3.6.
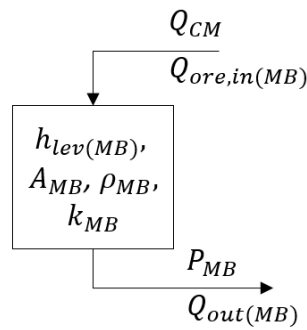
Figure 3.6. Mixing box unit.

The mixing box receives both ore from the feeder and medium from the correct medium pump. It is elevated above the dense medium cyclone, which is either gravity-fed from the mixing box (as in the case of this circuit), or pump-fed. The mixing box is modelled as a gravity-drained tank, and the conservation of volume is used to model the level:

$$\frac{dh_{lev(MB)}}{dt} = \frac{1}{A_{MB}}\left(Q_{CM} + Q_{ore,in(MB)} - Q_{out(MB)}\right),\tag{3.21}$$

where Q_{CM} is the medium flowing from the correct medium pump to the mixing box (delayed by the relevant time delay), $Q_{ore,in(MB)}$ is the ore entering the mixing box, $Q_{out(MB)}$ is the mixture of ore and medium draining out of the mixing box by gravity, $h_{lev(MB)}$ is the height of slurry in the mixing box,

and A_{MB} is the cross-sectional area of the mixing box. Note that the material in the mixing box is assumed well-mixed, and therefore the ratio of medium to ore in the flow out of the mixing box is considered equal to that of the flow in. The flow of the mixture gravity-draining out can be modelled as follows (Jang, 2016):

$$Q_{out(MB)} = k_{MB}\sqrt{h_{lev(MB)}}.$$ (3.22)

Note that the outlet coefficient, k_{MB} [m$^{5/2}$/s], is a function of the mixing box opening geometry, and is therefore a constant. It can, however, be used to model disturbances, such as a blockage in the mixing box which is not uncommon. Blockages cause overflows which lead to the loss of medium.

The level of the mixing box is measured; however the reading is notoriously unreliable at the plant in question due to the geometry of the mixing box, as well as the nature of the environment: the medium entering the mixing box causes significant splashes that interfere with the instrument. Therefore, for this work, the mixing box level is considered unmeasured. The feed pressure to the dense medium cyclone is measured, and this is a function of the difference in height between the dense medium cyclone and the slurry level in the mixing box. This pressure, P_{MB} [kPa], can be calculated as follows:

$$P_{MB} = \rho_{MB}g(H_{MB} + h_{lev(MB)}),$$ (3.23)

where ρ_{MB} [t/m^3] is the density of the ore and medium mixture in the mixing box, and H_{MB} [m] is the height differential between the mixing box outlet and the pressure gauge.

Table 3.7 describes the process variables for the mixing box in terms of measured and unmeasured variables, where subscript MB refers to the mixing box.

Table 3.7. Mixing box tank model variables.

Variable	Unit	Description
Measured at the plant		
$Q_{ore,in(MB)}$	m^3/s	Ore flow rate to mixing box
P_{MB}	kPa	Mixing box discharge pressure
ρ_{MB}	t/m^3	Density of slurry in mixing box
Not measured at the plant		
$h_{lev(MB)}$	m	Mixing box level
$Q_{out(MB)}$	m^3/s	Flow rate out of mixing box

Note that while the flow of medium into the mixing box from the correct medium tank is not directly measured, it is an output of the correct medium tank system (see (3.14)), and is therefore available, either directly in the simulation, or via state estimation of the correct medium tank system. Additionally, ρ_{MB} is not known, but can be calculated using the ratio of ore to medium in the feed, as well as the known bulk density of the ore, ρ_{ore}, and the measured density of the correct medium being pumped from the correct medium tank, ρ_{CM}, as follows:

$$\rho_{MB} = \frac{Q_{CM}\rho_{CM} + Q_{ore,in(MB)}\rho_{ore}}{Q_{CM} + Q_{ore,in(MB)}} \tag{3.24}$$

A state-space model of the mixing box is:

$$\dot{x}_{MB} = f_{MB}(t, x_{MB}, u_{MB}, \boldsymbol{d}_{MB}) \tag{3.25}$$

$$= \frac{Q_{CM} + Q_{ore,in(MB)} - k_{MB}\sqrt{h_{lev(MB)}}}{A_{MB}}$$

$$\boldsymbol{y}_{MB} = g_{MB}(t, x_{MB}, u_{MB}, \boldsymbol{d}_{MB}) \tag{3.26}$$

$$= \begin{bmatrix} \rho_{MB}g(H_{MB} + h_{lev(MB)}) \\ \rho_{MB} \\ Q_{CM} \end{bmatrix},$$

where the model states, inputs, disturbances and outputs are given by $x_{MB} = h_{lev(MB)}$, $u_{MB} = Q_{ore,in(MB)}$, $\boldsymbol{d}_{MB} = [\rho_{MB}, Q_{CM}]^T$, and $\boldsymbol{y}_{MB} = [P_{MB}, \rho_{MB}, Q_{CM}]^T$ respectively.

Table 3.8 shows the values of the parameters required for the mixing box model.

Table 3.8. Mixing box model parameters.

Variable	Value	Description
A_{MB}	0.429 m^2	Cross-sectional area of mixing box
H_{MB}	5.7 m	Height differential of mixing box outlet and pressure gauge
k_{MB}	unknown	Mixing box outlet coefficient

3.8   DENSE MEDIUM CYCLONE AND DRAIN-AND-RINSE SCREENS

For the purposes of modelling the flow of medium through the DMS circuit, the dense medium cyclone and drain-and-rinse screens, shown in Figure 1.1, is simplified as shown in Figure 3.7.
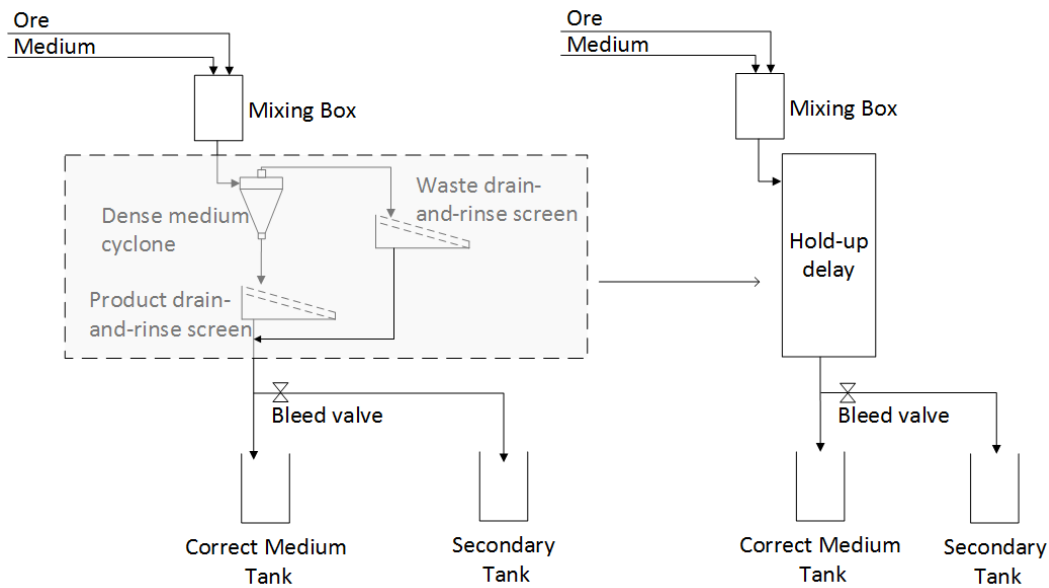
Figure 3.7. Model simplification of the dense medium cyclone and drain-and-rinse screens. Only the drained medium flow is shown. The flow of rinsed medium, which reports to the dilute medium tank, is not depicted, and is considered negligible.

The flow of material from the dense medium cyclone and the product and waste drain-and-rinse screens is therefore modelled as:

$$Q_{drain} = k_{DMC}Q_{in(DMC)}(t - d_{DMC}), \tag{3.27}$$

for $t > d_{DMC}$, where Q_{drain} is the flow of medium out of the unit to the correct medium tank, $Q_{in(DMC)}$ is the flow of medium out of the mixing box (obtained from the flow of medium and ore out of the mixing box, assuming the same ore-to-medium ratio in the mixing box discharge as that of the mixing box feed) to the dense medium cyclone, and d_{DMC} is the delay term. The inclusion of the parameter k_{DMC} is to accommodate any instances where the flow of medium out of the system might differ from the flow into the system. This can be used to model instances of medium losses at the drain-and-rinse screens (see Section 7.4).

3.9   DENSIFIERS

3.9.1   Primary densifier

The primary densifier is a battery of six hydrocyclones fed from the primary densifier pump. The hydrocyclones separate feed based on density into the overflow (lower density) and underflow (higher density). For this work, a steady-state model of the volumetric split is used, as the dynamics of

this process is assumed to be fast relative to the rest of the circuit. The volumetric split of a single hydrocyclone is given by ([Bueno](), 2021; [Flintoff et al.](), 1987):

$$S_{cyc} = \frac{Q_{UF}}{Q_{OF}} = k_{cyc}h_{cyc}^{0.19}\left(\frac{d_{apex}}{d_{vortex}}\right)^{2.64}\frac{e^{-4.33\alpha+8.77\alpha^2}}{P_{feed}^{0.54}d_{cyc}^{0.38}}, \tag{3.28}$$

where d_{apex} is the diameter of the cyclone apex, d_{vortex} is the diameter of the cyclone vortex, d_{cyc} is the diameter of the cyclone, h_{cyc} is the height of the cyclone, α is the solids fraction in the feed, per volume unit, P_{feed} is the feed pressure to the hydrocyclone, and Q_{UF} and Q_{OF} is the cyclone under- and overflow respectively. The parameter k_{cyc} is a fitting parameter ([Sepúlveda](), 2004). Table [3.9]() gives the values of the parameters for ([3.28]()).

Table 3.9. Primary densifier parameters.

Variable	Value	Description
d_{apex}	45 mm	Hydrocyclone apex
d_{vortex}	70 mm	Hydrocyclone vortex
d_{cyc}	165 mm	Hydrocyclone diameter
h_{cyc}	350 mm	Hydrocyclone height
k_{cyc}	54.96	Hydrocyclone fitting coefficient

Because the primary densifier consists of a battery of six hydroclones, the overall volume split S_{PD} is assumed to be equal to the individual volumetric split S_{cyc} of a single hydrocyclone. The overflow and underflow of the primary densifier can therefore be modelled as:

$$Q_{OF(PD)} = \frac{Q_{feed(PD)}}{S_{PD}+1} \tag{3.29}$$

$$Q_{UF(PD)} = Q_{feed(PD)} - Q_{OF(PD)},$$

where $Q_{OF(PD)}$ and $Q_{UF(PD)}$ are the volumetric flow rates of the primary densifier overflow (which reports to the secondary tank) and underflow (which reports to the correct medium tank) respectively, and $Q_{feed(PD)}$ is the volumetric flow rate of the primary densifier feed.

3.9.2 Secondary densifier

The secondary densifier, in contrast to the primary densifier, is a pipe densifier. This type of densifier is not well explored in the literature. [Legault-Seguin et al.]() ([2017]()) gives typical mass balance values for a pipe densifier found in a DMS circuit, and so for this work these typical values will be used. Therefore, the volumetric split of the secondary densifier is assumed to be $S_{SD} = 2.3$. The volumetric flow rates of

the secondary densifier overflow and underflow are therefore given as:

$$Q_{OF(SD)} = \frac{Q_{feed(SD)}}{S_{SD} + 1} \tag{3.30}$$

$$Q_{UF(SD)} = Q_{feed(SD)} - Q_{OF(SD)}$$

where $Q_{OF(SD)}$ and $Q_{UF(SD)}$ are the volumetric flow rates of the secondary densifier overflow (which reports to the dilute medium tank) and underflow (which reports to the correct medium tank) respectively, and $Q_{feed(SD)}$ is the volumetric flow rate of the secondary densifier feed.

3.10   MAGNETIC SEPARATOR

The magnetic separator is modelled in steady-state, as the dynamics of the volumetric split between the concentrate and the effluent outputs of the magnetic separator are considered much faster than the rest of the circuit. The magnetic separator is modelled according to Rayner and Napier-Munn (2003b), in which a mathematical model of the concentrate solids content for a wet drum magnetic separator was developed. The model includes an equation for the volumetric flow rate through the drainage area which then becomes the concentrate flow to the correct medium tank:

$$Q_D = k_1 Q_f \left(\frac{D^2 \omega}{Q_f} \right)^{k_2} \left(\frac{x_p}{D} \right)^{k_3} \left(\frac{x_D}{D} \right)^{k_4} \alpha_f^{k_5} \left(\frac{\rho_s Q_f}{M_f} \right)^{k_6}, \tag{3.31}$$

where $k_1, k_2, k_3, k_4, k_5, k_6$ are parameters to be fitted, D is the drum diameter, ω is the drum rotational velocity, x_p and x_D are the pickup and discharge gaps respectively, α_f is the feed moisture, Q_f and M_f are the volumetric and mass feed rates per unit length respectively, and ρ_s is the solids density.

The magnetic separator in operation at the DMS plant studied here is not well instrumented. The feed density and flow are not measured, and neither are the drainage flow rate or density. Fitting the parameters in (3.31) is therefore impractical, and not the focus of this work. For the purposes of this work, (3.31) is simplified as follows:

$$Q_{MS} = Q_{feed(MS)} k_{MS}, \tag{3.32}$$

where Q_{MS} is the flow rate of concentrate from the magnetic separator to the correct medium tank, $Q_{feed(MS)}$ is the feed flow rate from the dilute medium pump to the magnetic separator, and k_{MS} is given a nominal value of 0.048 (obtained from mass balances of magnetic separators given in Legault-Seguin et al. (2017)). The value of k_{MS} can be changed in order to simulate medium losses to the magnetic separator effluent (see Section 7.5), which are generally significant contributors to medium losses (Dardis, 1989).

3.11   CHAPTER SUMMARY

In this chapter, the DMS circuit was divided into individual units: the circuit tanks (correct medium, secondary and dilute medium tanks), the mixing box, the dense medium cyclone and drain-and-rinse screens (simplified into a single unit), the primary and secondary densifiers, and the magnetic separator. The individual unit models were developed and presented. The circuit tanks and mixing box were modelled dynamically, while the densifiers, the DMC and drain-and-rinse screens, and the magnetic separator were modelled in steady-state.

CHAPTER 4 MODEL SIMULATION AND VALIDATION

4.1 CHAPTER OVERVIEW

In this chapter, the individual unit models of the DMS circuit, presented in Chapter 3, are implemented on a simulation platform (Simulink) in Section 4.2. In Sections 4.2.1, 4.2.2, 4.2.3 and 4.2.4 the results of the simulation are presented for the correct medium tank, the secondary tank, the dilute medium tank, and the mixing box respectively.

In Section 4.3, the model is validated using plant data for the correct medium tank and the mixing box in Sections 4.3.1 and 4.3.2 respectively. The steady-state models of units such as the magnetic separator and the densifiers are not instrumented, and so model validation is not possible for these units. The model performance is evaluated using the root-mean-square error between the model outputs and the plant outputs.

4.2 DMS CIRCUIT SIMULATION

The full model of the flow of medium through the DMS circuit, described in Section 3, is constructed in Simulink and simulated. Figure 4.1 shows this model. Note that in Figure 4.1 Q_{rinse} refers to the flow rate of rinsed medium passing from the drain-and-rinse screens to the dilute medium tank. The model was simulated using representative initial pump speeds. A step change in the primary densifier pump speed was then introduced at $t = 230$ s. The following sections show the results of this simulation for individual dynamic units.
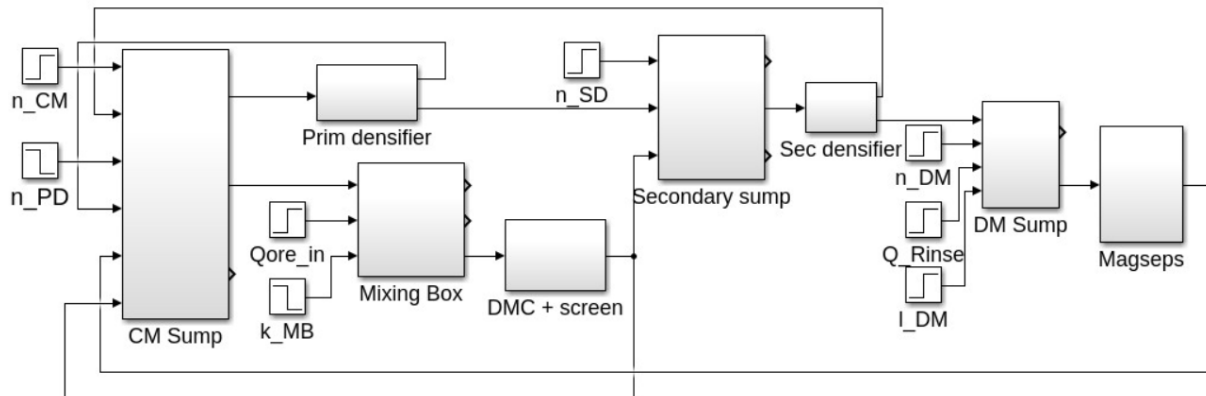
Figure 4.1. Model of DMS circuit in Simulink.

4.2.1   Correct medium tank simulation results

Figure 4.2 shows the inputs and uncontrolled disturbances to the correct medium tank simulation. The pump speeds (at top in Figure 4.2), are inputs to the system. The density (ρ_{CM}) is an uncontrolled disturbance, while the flows into the correct medium tank model ($Q_{UF(SD)}$, Q_{drain}, $Q_{UF(PD)}$, and Q_{MS} in Figure 4.2) are state outputs of other unit models, and combined form $Q_{in(CM)}$ in (3.13), which is also an uncontrolled disturbance to the correct medium tank system.

Figure 4.2. Inputs and uncontrolled disturbances to correct medium tank system simulation.

Note that at $t = 230$ s the primary densifier pump speed (n_{PD}) is decreased from 0.79 to 0.74. Figure 4.3 shows the response of the correct medium tank system states and outputs.
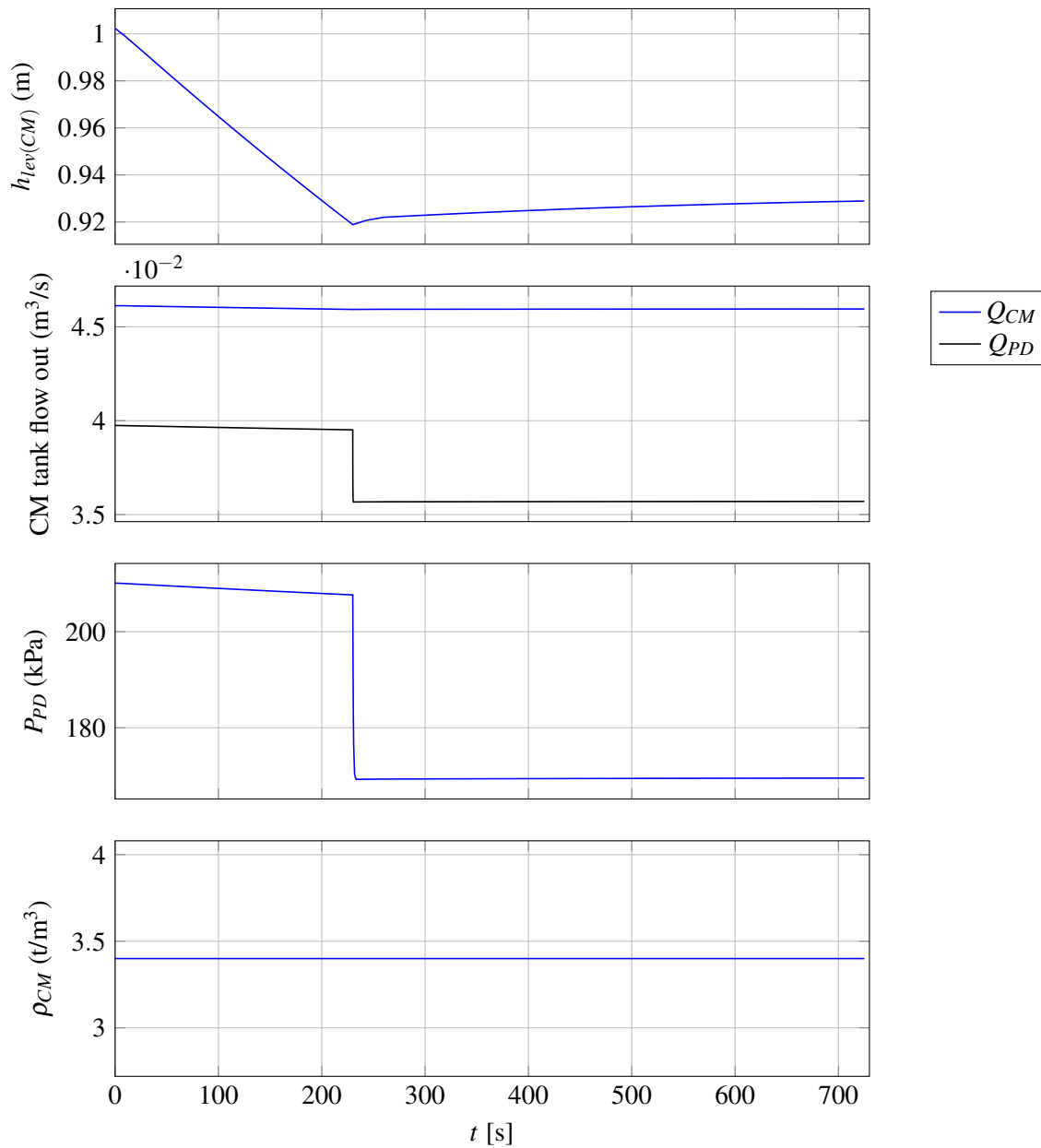
Figure 4.3. States and outputs of correct medium tank system simulation.

At $t = 230$ s, when the primary densifier pump speed is decreased, the primary densifier pump flow rate (Q_{PD} in Figure 4.3) decreases as expected, and consequently the primary densifier underflow ($Q_{UF(PD)}$ in Figure 4.2) also decreases. This is consistent with the theory because the primary densifier pump flow is the primary densifier feed flow, and a reduction in the feed flow is expected to result in a reduction in both the overflow and the underflow of the densifier. The rate of change of the level of the

correct medium tank ($h_{lev(CM)}$ in Figure 4.3) increases as expected, and the primary densifier pump discharge pressure (P_{PD} in Figure 4.3) also decreases as expected.

4.2.2   Secondary tank simulation results

The inputs and uncontrolled disturbances to the secondary tank system simulation are shown in Figure 4.4. The secondary densifier pump speed (at top in Figure 4.4) is an input to the system. The density (ρ_{sec}) is an uncontrolled disturbance, while the flows into the secondary tank model ($Q_{OF(PD)}$ and Q_{bleed} in Figure 4.4) are state outputs of other unit models, and combined form $Q_{in(sec)}$ in (3.15), which is an uncontrolled disturbance to the secondary tank system.
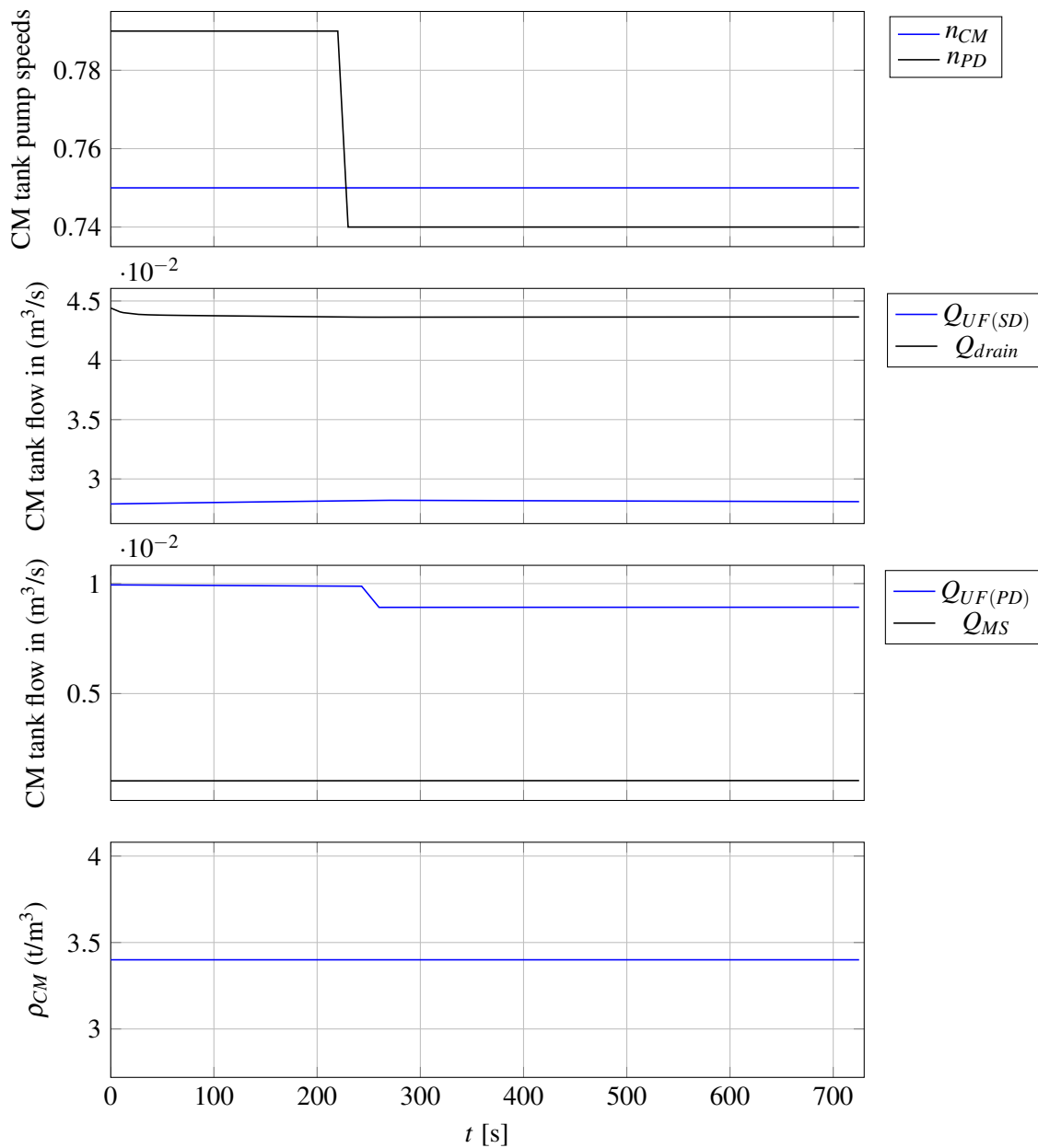

Figure 4.4. Inputs and uncontrolled disturbances to secondary tank system simulation.

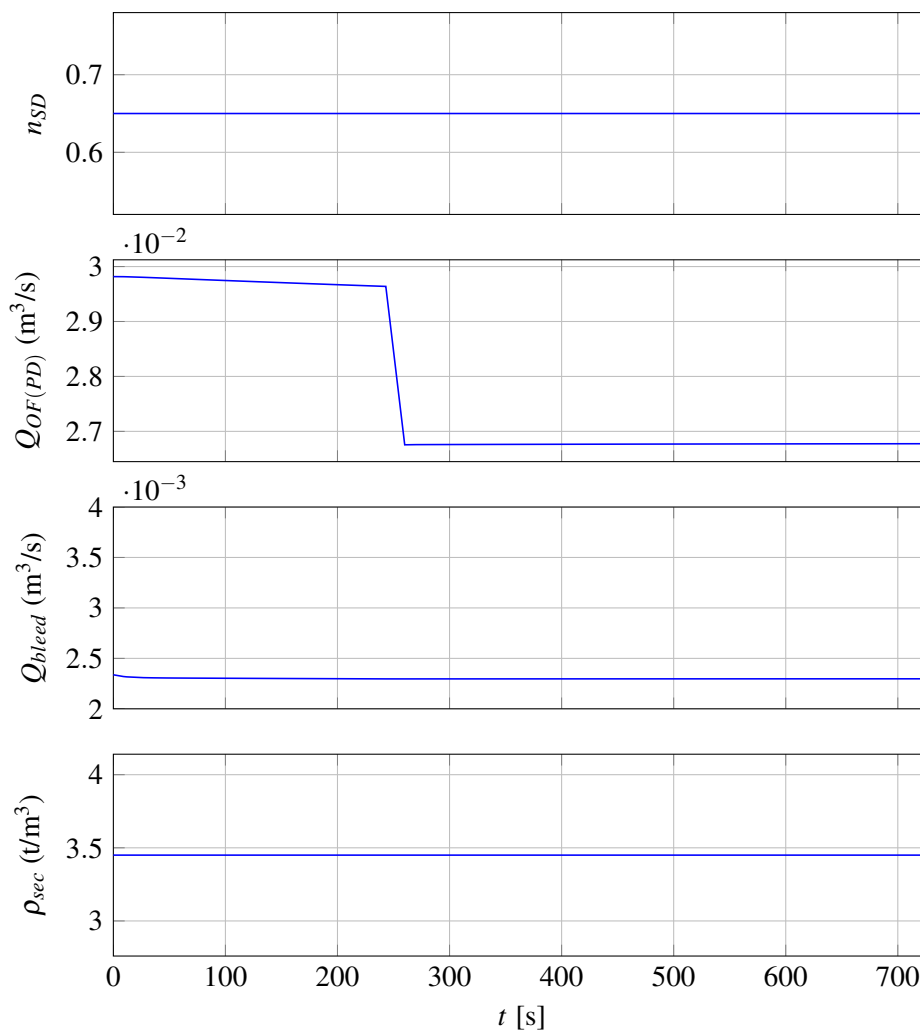After $t = 230$ s (after the transport delay in the model), the primary densifier overflow ($Q_{OF(PD)}$ in Figure 4.4) decreases. This is expected as the primary densifier pump flow (Q_{PD} - see Figure 4.3) is

the primary densifier feed flow, and a reduction in the feed flow is expected to result in a reduction in both the overflow and the underflow of the densifier. Figure 4.5 shows the response of the secondary tank system states and outputs to the inputs and uncontrolled disturbances seen in Figure 4.4.

Figure 4.5. States and outputs of secondary tank system simulation.

Following the decrease in primary densifier overflow ($Q_{OF(PD)}$, at middle in Figure 4.4), the rate of change of the level of the secondary tank ($h_{lev(sec)}$, at top in Figure 4.5) decreases as expected. The secondary densifier pump flow rate (Q_{SD}, at middle in Figure 4.5) remains fairly constant due to the constant n_{SD}, while the discharge pressure (P_{SD}, at bottom in Figure 4.5) at first increases slightly with increasing $h_{lev(sec)}$, and then stabilises as $h_{lev(sec)}$ becomes more stable.

4.2.3 Dilute medium tank simulation results

The inputs and uncontrolled disturbances to the dilute medium tank system simulation are shown in Figure 4.6. The dilute medium pump speed is an input to the system, and since the dilute medium pump is a fixed speed pump, $n_{DM} = 1$ throughout the simulation. The dilute medium tank water valve opening, l_{DM}, is also an input. The density of the dilute medium tank, ρ_{DM}, is an uncontrolled

disturbance, while the flows into the tank (Q_{rinse} and $Q_{OF(SD)}$) are outputs from other units, and combined form $Q_{in(DM)}$ in (3.19).
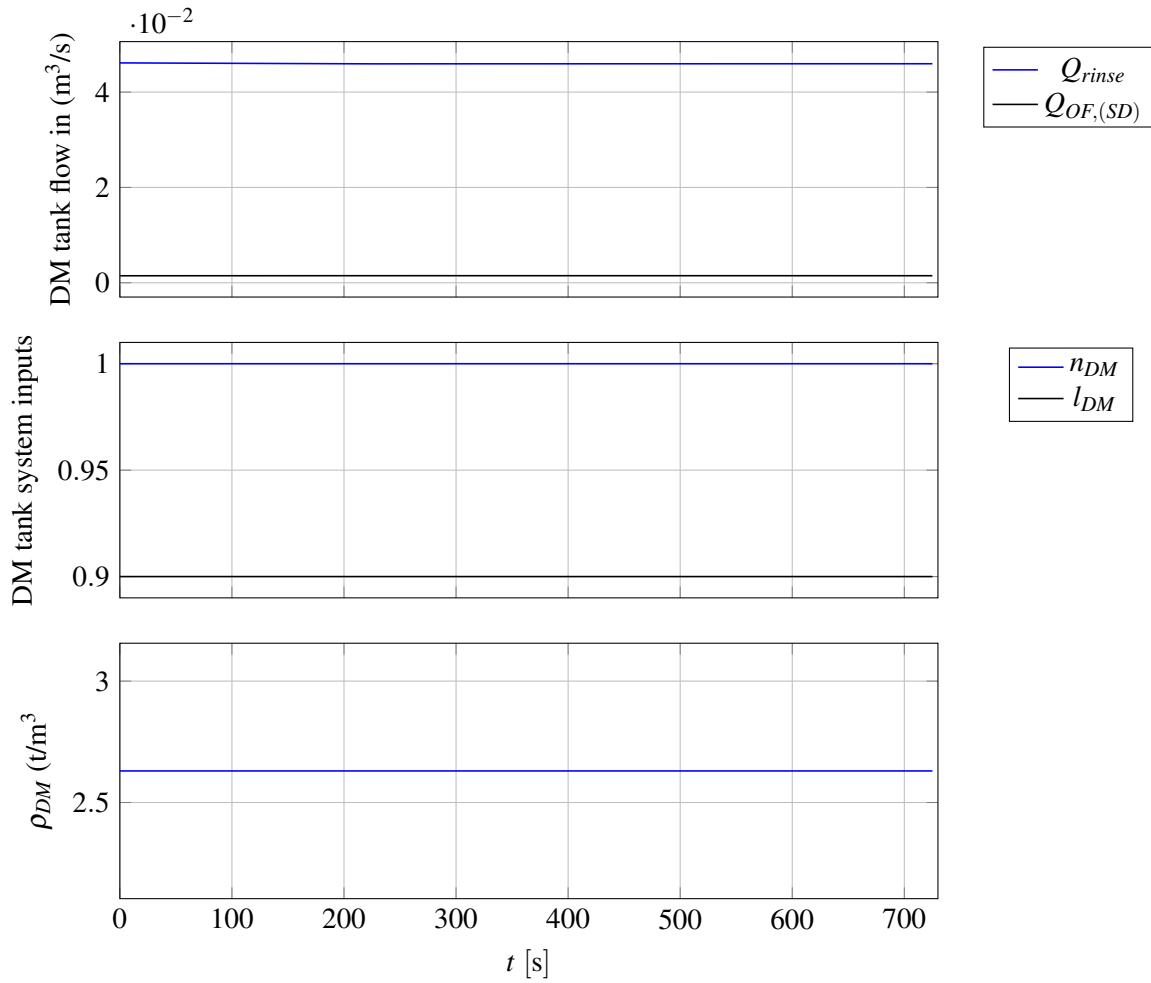
Figure 4.6. Inputs and uncontrolled disturbances to dilute medium tank system simulation.

Figure 4.7 shows the response of the dilute medium tank system states and outputs to the inputs and uncontrolled disturbances in Figure 4.6.
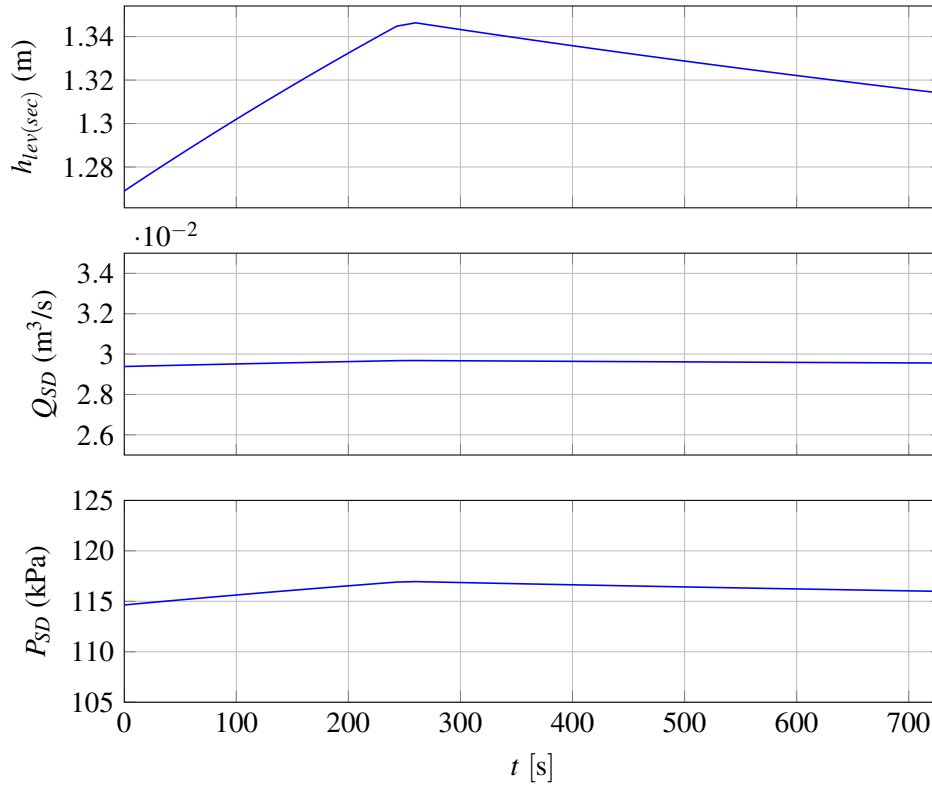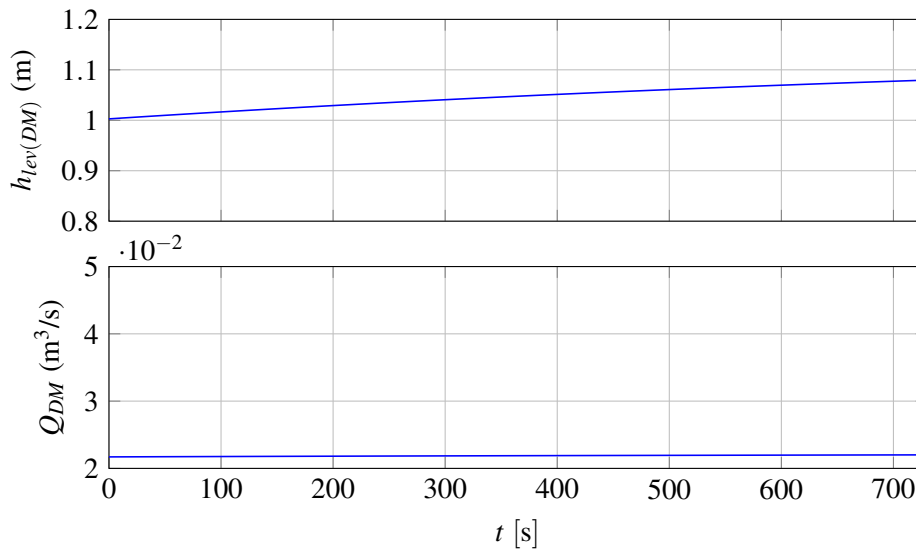
Figure 4.7. States and outputs of dilute medium tank system simulation.

4.2.4   Mixing box simulation results

The inputs and uncontrolled disturbances to the mixing box system simulation are shown in Figure 4.8. The mixing box outlet coefficient (k_{MB} in Figure 4.8), as well as the volumetric flow of ore into the mixing box ($Q_{ore,in(MB)}$ in Figure 4.8), are inputs to the system. The density ρ_{MB}, calculated as in 3.24, is an uncontrolled disturbance, as is the flow of medium into the mixing box (Q_{CM} in Figure 4.8), which is a state output of the correct medium tank model.
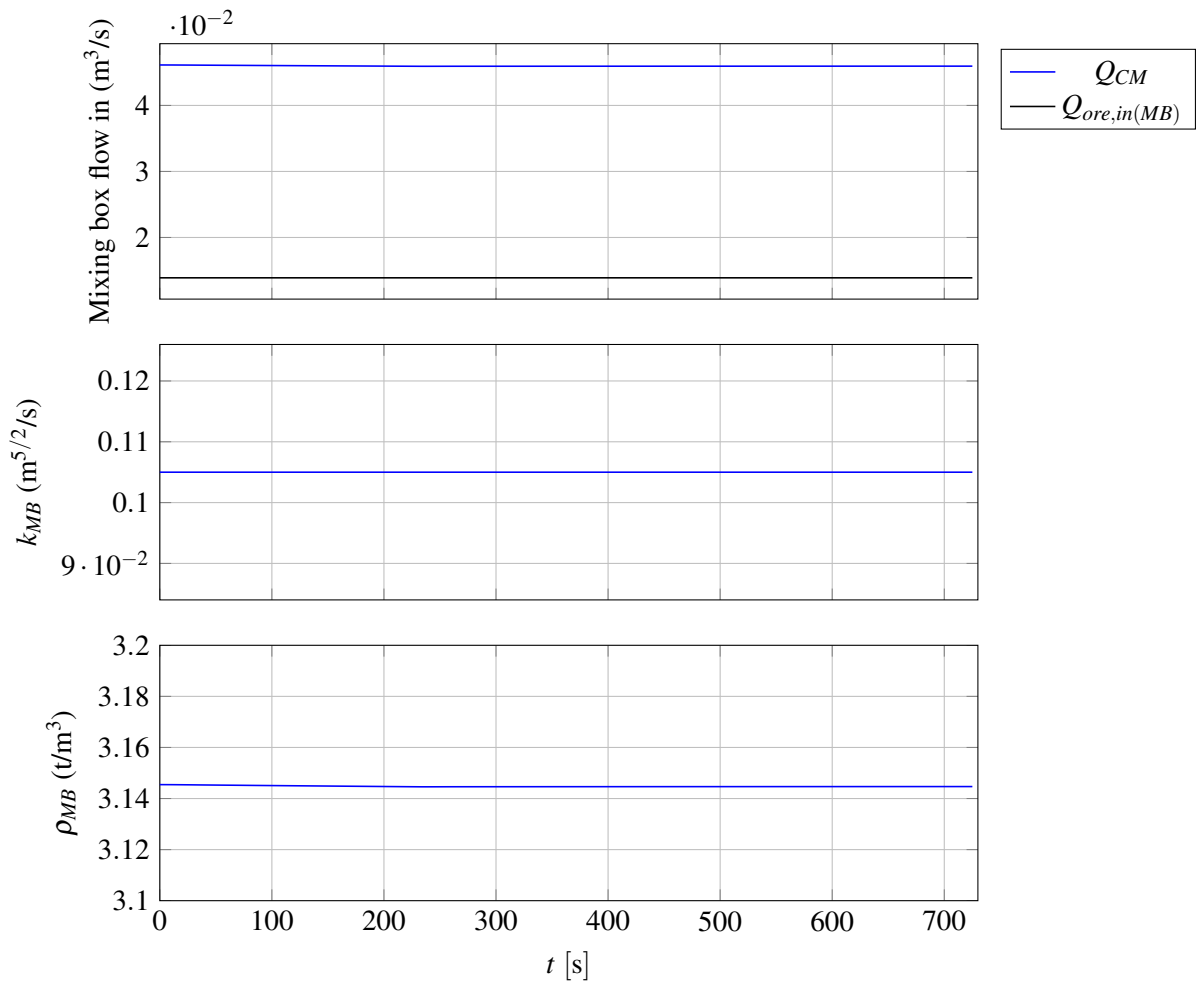
Figure 4.8. Inputs and uncontrolled disturbances to mixing box system simulation.

The inputs and uncontrolled disturbances to the mixing box unit (seen in Figure 4.8) were constant during the simulation. The response of the mixing box system states and outputs are seen in Figure 4.9. Also shown are the volumetric flow rates of ore and medium out of the mixing box.
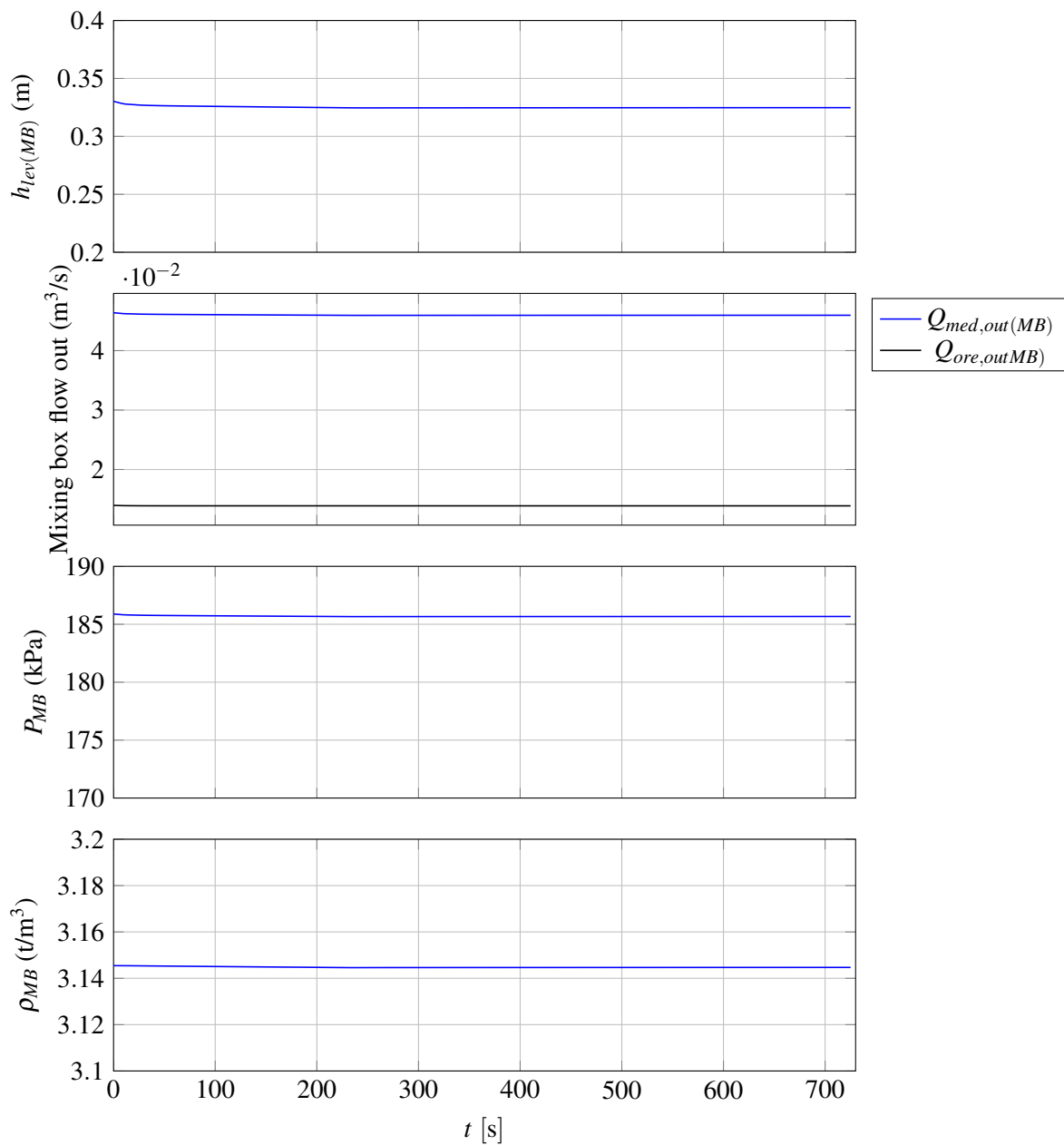
Figure 4.9. States, outputs, and volumetric out-flows of mixing box system simulation.

As expected (due to the inputs and disturbances to the mixing box unit model simulation being constant for the duration of the simulation), the simulated mixing box level and discharge pressure ($h_{lev(MB)}$ and P_{MB} in Figure 4.9, respectively) remain constant.

4.3 MODEL VALIDATION

The process of model validation is not straight forward, because the correct medium model requires knowledge of the flow into the correct medium tank (see (3.13)). While this is known in the simulation, this is not known in the plant, as the true split of flow between the primary and secondary densifier over- and underflows, as well as the magnetic separator concentrate flow, are unknown, and cannot be confirmed given the current level of instrumentation in the plant.

Similarly, the value of the mixing box outlet coefficient (k_{MB}) in the mixing box model (see (3.25)) is unknown. Therefore, to validate the correct medium tank and mixing box systems, the plant data for the model inputs was fed to the model, which yielded an approximation of the flow of material into the correct medium tank. Additionally, the value of k_{MB} was tuned to fit the data for the mixing box model. Note that Section 6 develops state estimation of these unknown quantities.

To indicate the accuracy of the model, the root-mean-square of the error (RMSE) between the model outputs and the plant outputs is used, and the RMSE value is then normalised using the mean ($\bar{y}$) to enable comparison between different outputs. The RMSE and normalised RMSE (NRMSE) are calculated as follows (Willmott, 1981):

$$RMSE = \sqrt{\frac{1}{N}\sum_{i=1}^{N}(P_i - O_i)^2}$$

$$NRMSE = \frac{RMSE}{\bar{y}} \tag{4.1}$$

where P is the model predicted output, O is the observed plant output, and N is the total number of samples.

4.3.1 Correct medium tank model validation

Figure 4.10 shows the inputs to the plant and model used for the data validation. Note that the correct medium and primary densifier pump speeds (n_{CM} and n_{PD} respectively - see the top two trends in Figure 4.10) are plant data, while the flow of slurry into the correct medium tank ($Q_{in(CM)}$ in Figure 4.10) is obtained from the simulation, due to the fact that this quantity is not measured.
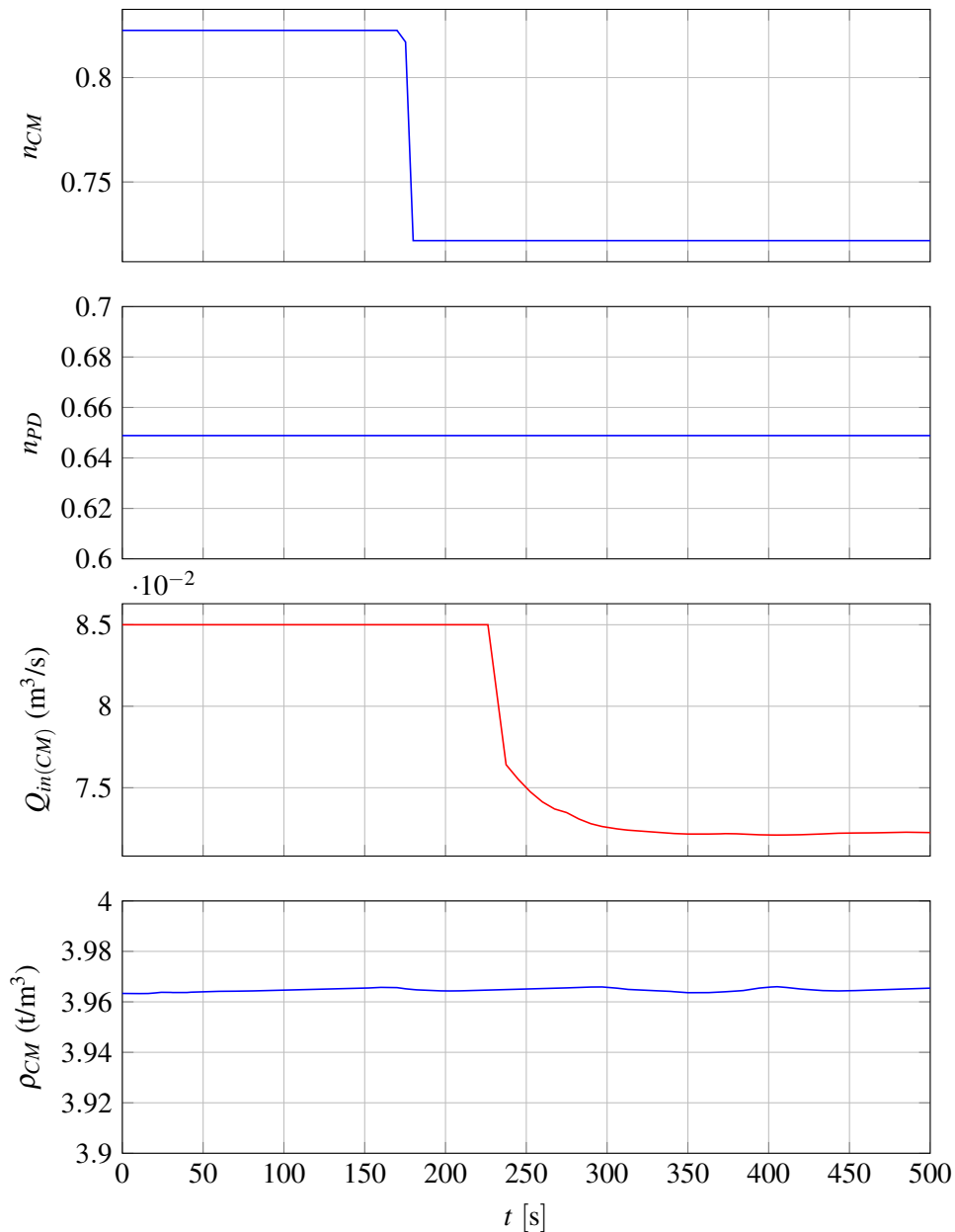
Figure 4.10. Inputs and uncontrolled disturbances to correct medium tank simulation. The correct medium pump speed n_{CM}, primary densifier pump speed n_{PD}, and correct medium tank density ρ_{CM} are plant data, while the flow into the correct medium tank $Q_{in(CM)}$ is an output from the simulation model for the remaining units (calculated using the mixing box model outputs, primary and secondary densifier model outputs, and magnetic separator model outputs). Blue indicates plant data, while red indicates simulation data.

At $t = 175$ s, the speed of the correct medium pump (n_{CM}, at top in Figure 4.10) is decreased from 0.82

to 0.72. The response of the flow rate of medium into the correct medium tank ($Q_{in(CM)}$, at bottom in Figure 4.10) follows as expected: it is constant until $t = 230$ s (following a transport delay after $t = 175$ s when n_{CM} is decreased) at which point it decreases. This is expected as decreasing n_{CM} results in an decrease of the flow of medium to the mixing box, and subsequently to the drain-and-rinse screens, thus decreasing the drain flow rate to the correct medium tank (see Figure 2.2).

The response of the correct medium tank system states to the inputs in Figure 4.10 is seen in Figure 4.11.
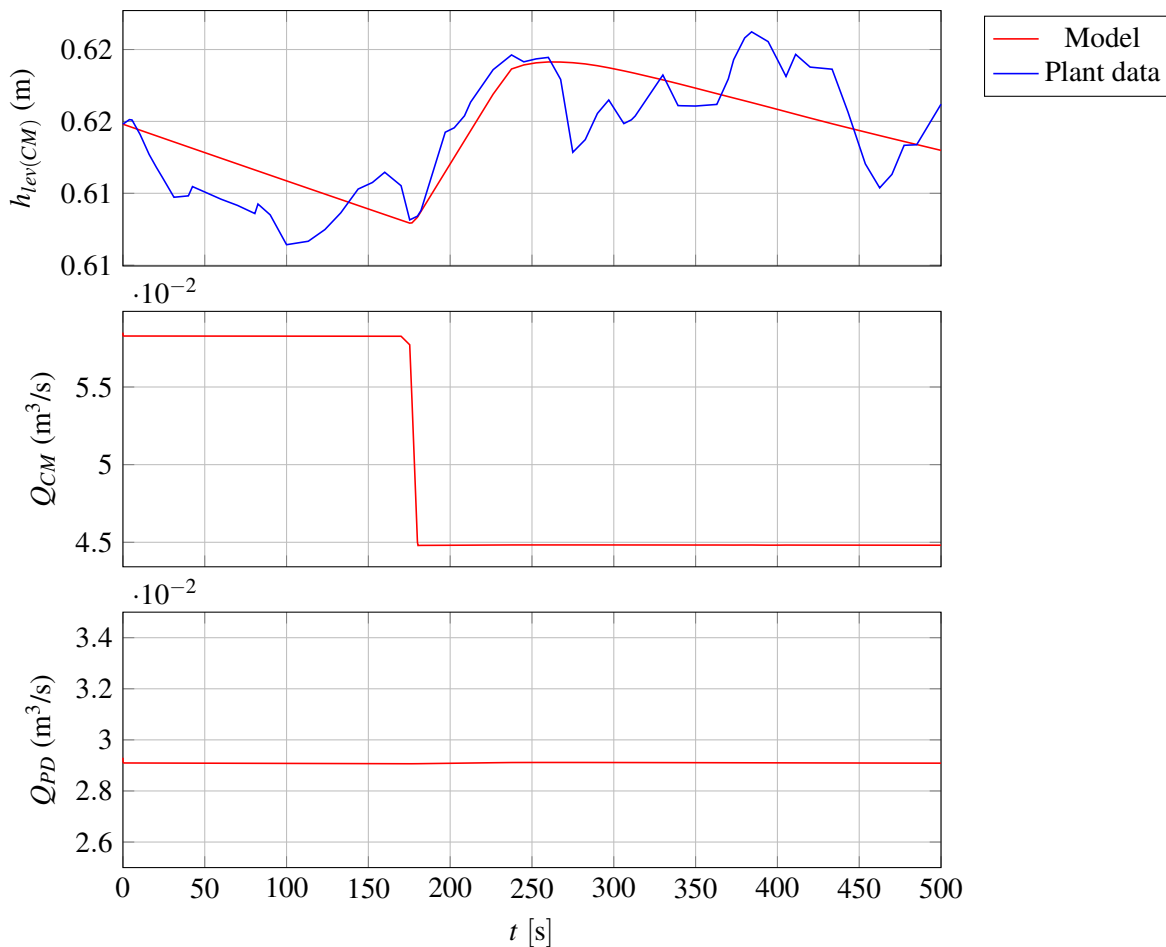
Figure 4.11. States of correct medium tank simulation and plant data.

The correct medium and primary densifier pump flow rates (Q_{CM} and Q_{PD}, at middle and bottom of Figure 4.11 respectively) respond as expected: Q_{CM} decreases with n_{CM} (in Figure 4.10), and Q_{PD} remains constant with constant n_{PD} (in Figure 4.10). The correct medium tank level ($h_{lev(CM)}$, at top in Figure 4.11) model response (blue) and plant response (red) respond accordingly, with the model

response tracking the plant response adequately. The rate of change of the level increases briefly following the decrease in Q_{CM}. The rate of change then returns to its previous rate as $Q_{in(CM)}$ decreases to match the decrease in Q_{CM}, after the transport delay.

Figure 4.12 shows the response in the primary densifier pump discharge pressure.
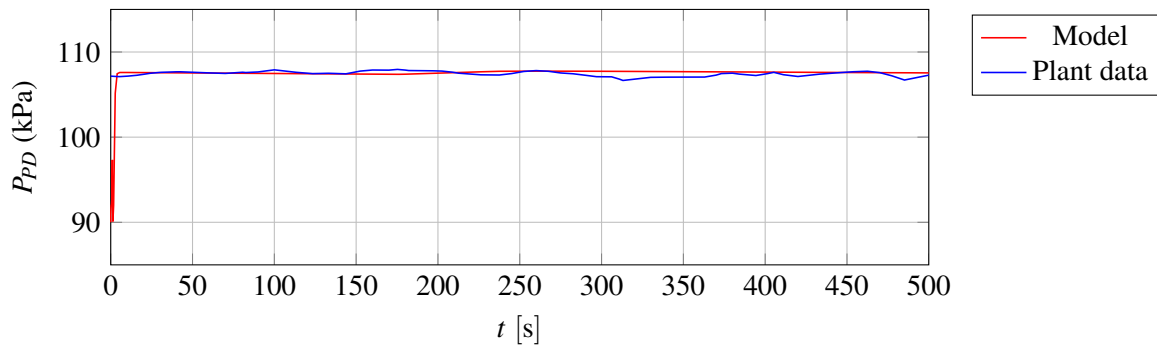
Figure 4.12. Primary densifier pump discharge pressure simulation and plant data.

The primary densifier discharge pressure (P_{PD}) in Figure 4.12 remains constant as expected as n_{PD} seen in Figure 4.10 remains constant. Note that the model output (in red) tracks the plant output (in blue) adequately.

Table 4.2 gives the RMSE and NRSME for the outputs in the correct medium tank model validation.

Table 4.1. RMSE and NRMSE values for correct medium tank model validation.

Circuit unit	Output	RMSE	NRMSE
Correct medium tank	$h_{lev(CM)}$	0.0022 m	0.0037
	P_{PD}	0.3824 kPa	0.0037

4.3.2 Mixing box model validation

Figure 4.13 shows the inputs to the plant and model used for the data validation. The mixing box outlet coefficient (k_{MB}, see (3.25)) is tuned to fit the data as this is not measurable on site. Furthermore, the flow of medium into the mixing box is obtained from the correct medium tank model (see Figure 4.11),

using the correct medium pump volumetric flow rate (with a transport delay incorporated). The ore feed is obtained from plant data.
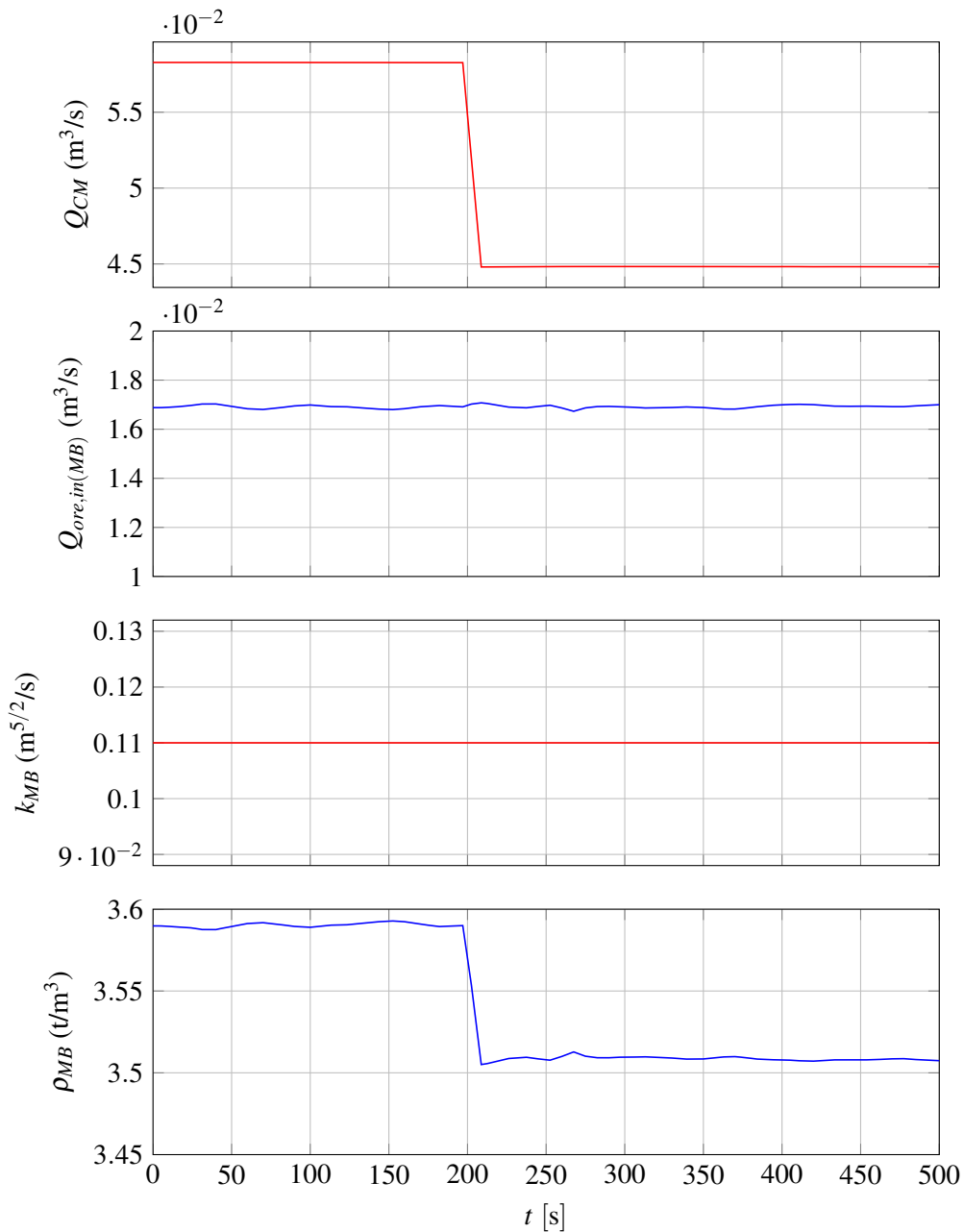
Figure 4.13. Inputs and uncontrolled disturbances to mixing box Simulink model. $Q_{ore,in(MB)}$ is plant data, while Q_{CM} is an output from the correct medium tank model, and k_{MB} is a tuned value. ρ_{MB} is calculated from plant data of ρ_{CM}, the known ore bulk density, and the volumetric flow rates of Q_{CM} and $Q_{ore,in(MB)}$. Blue indicates plant data, while red indicates simulation data.

At $t = 200$ s, the flow rate of medium into the mixing box (Q_{CM}, at top in Figure 4.13) decreases. This is as expected, as this follows Q_{CM} seen in Figure 4.11, with a transport delay. The flow rate of ore into the mixing box ($Q_{ore,in(MB)}$, at middle in Figure 4.13) is relatively constant, while k_{MB} (at bottom in Figure 4.13) is kept constant in the simulation.

Figure 4.14 shows the response of the mixing box system states and outputs to the inputs in Figure 4.13.
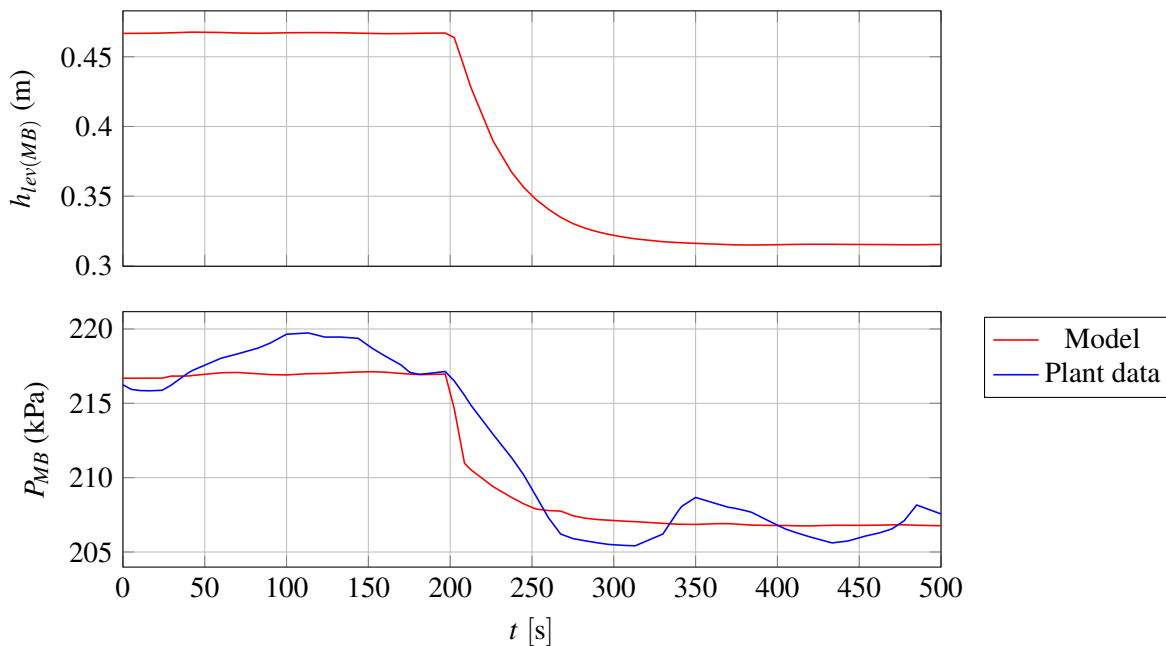
Figure 4.14. States and outputs of mixing box simulation and plant data.

The model response of the mixing box level ($h_{lev(MB)}$, at top in Figure 4.14) is as expected, with the level decreasing when Q_{CM} decreases (at top in Figure 4.13). The level then stabilises, as the flow out of the mixing box decreases to balance the decrease in the flow into the mixing box (see (3.22)).

The model response and the plant response of the mixing box discharge pressure (P_{MB}, at bottom in Figure 4.14) is also as expected, with the pressure decreasing with $h_{lev(MB)}$. Note the model response tracks the plant response adequately, although the plant data for P_{MB} is quite noisy.

Table 4.2 gives the RMSE and NRSME for the outputs in the mixing box model validation.

Table 4.2. RMSE and NRMSE values for mixing box model validation.

Circuit unit	Output	RMSE	NRMSE
Mixing box	P_{MB}	1.6079 kPa	0.0077

4.4 CHAPTER SUMMARY

In this chapter, the individual models of the units within the DMS circuit (described in Section 3) were combined into a full circuit model, and implemented on a simulation platform, Simulink. The results of the simulation were then presented for the correct medium tank, secondary tank, and mixing box. The simulation results were consistent with the expected response.

The model was then validated using plant data for the correct medium tank and mixing box. The correct medium model requires knowledge of the flow into the correct medium tank, and while this is known in the simulation, this is not known in the plant, given the current level of instrumentation. Similarly, the value of the mixing box outlet coefficient (k_{MB}) in the mixing box model is unknown. Therefore, plant data for the model inputs was fed to the model, which yielded an approximation of the flow of material into the correct medium tank, and the value of k_{MB} was tuned to fit the data for the mixing box model.

The root-mean-square error and normalised root-mean-square error were used to assess the performance of the model, which was found to be adequate.

CHAPTER 5 OBSERVABILITY ANALYSIS

5.1 CHAPTER OVERVIEW

The model of the DMS circuit, developed in Section 3, is now analysed for observability. This analysis will be used to determine if the level of instrumentation and consequent observability of the circuit is sufficient for identifying medium losses. The observability analysis is performed on the dynamic models described in Section 3. Sections 5.3, 5.4, 5.5, and 5.6 analyse the observability of the correct medium tank, secondary tank, dilute medium tank, and mixing box systems respectively. For all these units, unmeasured inputs (which are necessarily modelled either as process disturbances or as parameters for the purposes of simulation) are identified and included in augmented models of the units as unmeasured states. The augmented models are then assessed for observability. If model states and parameters are unknown but observable, these states and parameters can potentially be estimated using for example an EKF, as is shown in Chapter 6.

Note that the units modelled in steady-state (the drain-and-rinse screens, primary and secondary densifiers, and magnetic separator) are not instrumented, and are not assessed for observability.

5.2 OBSERVABILITY THEORY

For the observability analysis, the unmeasured disturbances in the unit process models developed in Chapter 3 can be included in an observer by including the unmeasured disturbances as constant states in the state-vector in (3.1). The augmented system is:

$$
\dot{z} = \begin{bmatrix} \dot{x} \\ \dot{d} \end{bmatrix} = \begin{bmatrix} f(t, z, u) \\ 0 \end{bmatrix}
$$

$$
y = g(t, z, u).
$$

(5.1)

where $z \in \mathfrak{R}^n$ and $n = n_x + n_d$.

The model in (5.1) can be linearised around an equilibrium point using a small signal approach (Seborg et al., 2016). For small deviations around an equilibrium point $(\boldsymbol{z}_q, \boldsymbol{u}_q)$ where $\dot{\boldsymbol{z}} = 0$, the linearised system can be written as:

$$
\begin{aligned}
\delta \dot{\boldsymbol{z}} &= A\delta \boldsymbol{z} + B\delta \boldsymbol{u} \\
\delta \boldsymbol{y} &= C\delta \boldsymbol{z} + D\delta \boldsymbol{u},
\end{aligned}
\tag{5.2}
$$

where

$$
A = \frac{\partial}{\partial \boldsymbol{z}} f(t, \boldsymbol{z}, \boldsymbol{u})|_{(\boldsymbol{z}_q, \boldsymbol{u}_q)}, \; B = \frac{\partial}{\partial \boldsymbol{u}} f(t, \boldsymbol{z}, \boldsymbol{u})|_{(\boldsymbol{z}_q, \boldsymbol{u}_q)},
$$

$$
C = \frac{\partial}{\partial \boldsymbol{z}} g(t, \boldsymbol{z}, \boldsymbol{u})|_{(\boldsymbol{z}_q, \boldsymbol{u}_q)}, \text{ and } D = \frac{\partial}{\partial \boldsymbol{u}} g(t, \boldsymbol{z}, \boldsymbol{u})|_{(\boldsymbol{z}_q, \boldsymbol{u}_q)}.
$$

The deviation variables are defined as $\delta \boldsymbol{z} = \boldsymbol{z} - \boldsymbol{z}_q$, and $\delta \boldsymbol{u} = \boldsymbol{u} - \boldsymbol{u}_q$.

The dynamical system (5.2) is state observable if and only if the observability matrix $\mathcal{O}$ has full column rank n, where (Skogestad and Postlethwaite, 2005):

$$
\mathcal{O} = \left[C^T, A^T C^T, \dots A^{T^{n-1}} C^T \right]^T.
\tag{5.3}
$$

5.3   CORRECT MEDIUM TANK MODEL OBSERVABILITY

Note that in the model for the correct medium tank described in (3.13) and (3.14), the flow into the tank $Q_{in(CM)}$ is included as an uncontrolled disturbance. From Figure 1.1, it is clear that this comprises of multiple streams:

- Drained medium from the drain-and-rinse screens

- Underflow from the primary densifier

- Underflow from the secondary densifier

- Concentrate flow from the magnetic separator

None of these streams flowing into the correct medium tank are directly measured. Furthermore, as the drain-and-rinse screens, primary and secondary densifiers, and magnetic separator flows are not measured, their model outputs cannot be verified online. Therefore, although the flow into the correct medium tank, $Q_{in(CM)}$, is a process disturbance to the model described in Section 3.4, for the purposes of analysing observability it is necessary to include $Q_{in(CM)}$ as a state. This additional state is assumed constant. The density ρ_{CM} is similarly included. The correct medium tank nonlinear model in (3.13) and (3.14) is augmented such that $\boldsymbol{z}_{CM} = [\boldsymbol{x}_{CM}^T, \boldsymbol{d}_{CM}^T]^T$. The augmented state-space model is

therefore:

$$\dot{z}_{CM} = f'_{CM}(t, z_{CM}, u_{CM}) \tag{5.4}$$

$$= \begin{bmatrix} \frac{1}{A_{CM}}\left(Q_{in(CM)} - Q_{CM} - Q_{PD}\right) \\ \frac{1}{k_{j(CM)}}\left(\rho_{CM}g(H_{p(CM)} - h_{dis(CM)} + h_{lev(CM)}) - k_p Q_{CM}^2\right) \\ \frac{1}{k_{j(PD)}}\left(\rho_{CM}g(H_{p(PD)} - h_{dis(PD)} + h_{lev(CM)}) - k_p Q_{PD}^2\right) \\ 0 \\ 0 \end{bmatrix}$$

$$y_{CM} = g_{CM}(t, z_{CM}, u_{CM}) \tag{5.5}$$

$$= \begin{bmatrix} h_{lev(CM)} \\ \rho_{CM}g\left(H_{max(PD)}n_{PD}^2 - \frac{Q_{PD}^2}{2A_{PD}^2 g} - h_{dis(PD)} + h_{lev(CM)}\right) \\ \rho_{CM} \end{bmatrix}$$

where $z_{CM} = \left[h_{lev(CM)}, Q_{CM}, Q_{PD}, \rho_{CM}, Q_{in(CM)}\right]^T$, $u_{CM} = [n_{CM}, n_{PD}]^T$, and $y_{CM} = \left[h_{lev(CM)}, P_{PD}, \rho_{CM}\right]^T$.

The model described in (5.4) and (5.5) is non-linear. For an observability study to be performed, the model is therefore first linearised about an operating point using the Taylor series expansion (Skogestad and Postlethwaite, 2005):

$$f(x, u) = f(x_0, u_0) + \left.\frac{\delta f}{\delta x}\right|_{x_0, u_0} x + \left.\frac{\delta f}{\delta u}\right|_{x_0, u_0} u + H.O.T. \tag{5.6}$$

where f is the set of nonlinear first order differential equations that represent the correct medium tank, shown in (3.13).

The augmented linearized model matrices as per (5.2) is given below after substitution of the known

parameter values in Table 3.2:

$$
A_{CM} =
\begin{bmatrix}
0 & -0.125 & -0.125 & 0 & 0.125 \\
0.0102\rho_{CM} & a_{22(CM)} & 0 & a_{24(CM)} & 0 \\
0.0136\rho_{CM} & a_{32(CM)} & -280Q_{PD} & a_{34(CM)} & 0 \\
0 & 0 & 0 & 0 & 0 \\
0 & 0 & 0 & 0 & 0
\end{bmatrix}
\tag{5.7}
$$

$$
B_{CM} =
\begin{bmatrix}
0 & 0 \\
0.704n_{CM}\rho_{CM} & 0 \\
0.939n_{CM}\rho_{CM} & 0 \\
0 & 0 \\
0 & 0
\end{bmatrix}
\tag{5.8}
$$

$$
C_{CM} =
\begin{bmatrix}
1 & 0 & 0 & 0 & 0 \\
9.81\rho_{CM} & 0 & -31.85Q_{PD}\rho_{CM} & c_{24(CM)} & 0 \\
0 & 0 & 0 & 1 & 0
\end{bmatrix}
$$

where

$$a_{22(CM)} = -280Q_{CM} - 4.08 \times 10^{-7}Q_{CM}\rho_{CM}$$

$$a_{24(CM)} = -2.04 \times 10^{-7}Q_{CM}^2 + 0.352n_{CM}^2 + 0.0102h_{lev(CM)} - 0.213$$

$$a_{32(CM)} = -5.44 \times 10^{-7}Q_{CM}\rho_{CM}$$

$$a_{34(CM)} = -2.72 \times 10^{-7}Q_{CM}^2 + 0.469n_{CM}^2 + 0.0136h_{lev(CM)} - 0.283$$

$$c_{24(CM)} = -15.92Q_{PD}^2 + 122.6n_{PD}^2 + 9.81h_{lev(CM)} - 111$$

The observability matrix $\mathcal{O}_{CM}$ as determined from (5.3) is calculated for the linear system, and can be

seen in Appendix A (A.1).The observability matrix has a full rank of 5, i.e., all states and parameters

are observable. The determinant

$$\det\left(\mathcal{O}_{CM5\times5}\right) = 6.9 \times 10^5 Q_{CM}Q_{PD}^2\rho_{CM}^3$$

will only be zero if Q_{CM} Q_{PD}, or ρ_{CM} is zero. Therefore, the system is expected to be observable for

normal operating conditions. This result is significant as it means that the unmeasured flow of medium

into the correct medium tank ($Q_{in(CM)}$) is observable.

5.4 SECONDARY TANK MODEL OBSERVABILITY

As with the correct medium tank, the flow into the secondary tank, $Q_{in(sec)}$, is not measured, and comprises of the following streams (neither of which is measured):

- Overflow from the primary densifier

- Medium from the bleed stream of the drain-and-rinse screens drain flow

For the observer model, $Q_{in(sec)}$ is therefore included as a state. Similarly, the density ρ_{sec} is also included as a state. The secondary tank model in (3.15) and (3.16) is thus augmented such that $\boldsymbol{z}_{sec} = [\boldsymbol{x}_{sec}^T, \boldsymbol{d}_{sec}]^T$. The augmented state-space model is therefore:

$$\dot{\boldsymbol{z}}_{sec} = f'_{sec}(t, \boldsymbol{z}_{sec}, \boldsymbol{u}_{sec}) \tag{5.9}$$

$$= \begin{bmatrix} \frac{1}{A_{sec}}\left(Q_{in(sec)} - Q_{SD}\right) \\ \frac{1}{k_{j(SD)}}\left(\rho_{sec}g(H_{p(SD)} - h_{dis(SD)} + h_{lev(sec)}) - k_p Q_{SD}^2\right) \\ 0 \\ 0 \end{bmatrix}$$

$$\boldsymbol{y}_{sec} = g_{sec}(t, \boldsymbol{x}_{sec}, \boldsymbol{u}_{sec}) \tag{5.10}$$

$$= \begin{bmatrix} h_{lev(sec)} \\ \rho_{sec}g\left(H_{max(SD)}n_{SD}^2 - \frac{Q_{SD}^2}{2A_{SD}^2 g} - h_{dis(SD)} + h_{lev(sec)}\right) \\ \rho_{sec} \end{bmatrix}$$

where $\boldsymbol{z}_{sec} = \left[h_{lev(sec)},\ Q_{SD},\ \rho_{sec},\ Q_{in(sec)}\right]^T$, $\boldsymbol{u}_{sec} = n_{SD}$, and $\boldsymbol{y}_{sec} = \left[h_{lev(sec)},\ P_{SD},\ \rho_{sec}\right]^T$. The linearized model matrices as per (5.2) is given below after substitution of the known parameter values in

Table 3.4:

$$\boldsymbol{A}_{sec} = \begin{bmatrix} 0 & -0.366 & 0 & 0.366 \\ 0.0136\,\rho_{sec} & a_{22(sec)} & a_{23(sec)} & 0 \\ 0 & 0 & 0 & 0 \\ 0 & 0 & 0 & 0 \end{bmatrix} \tag{5.11}$$

$$\boldsymbol{B}_{sec} = \begin{bmatrix} 0 \\ 0.874\,n_{SD}\,\rho_{sec} \\ 0 \\ 0 \end{bmatrix} \tag{5.12}$$

$$\boldsymbol{C}_{sec} = \begin{bmatrix} 1 & 0 & 0 & 0 \\ 9.81\,\rho_{sec} & -31.8\,Q_{SD}\,\rho_{sec} & c_{23(sec)} & 0 \\ 0 & 0 & 1 & 0 \end{bmatrix},$$

where

$$a_{22(sec)} = -280\,Q_{SD} - 2.45e - 6\,Q_{SD}\,\rho_{sec}$$

$$a_{23(sec)} = -1.22 \times 10^{-6}\,Q_{SD}{}^2 + 0.437\,n_{SD}{}^2 + 0.0136\,h_{lev(sec)} - 0.265$$

$$c_{23(sec)} = -15.9\,Q_{SD}{}^2 + 315\,n_{SD}{}^2 + 9.81\,h_{lev(sec)} - 191$$

The observability matrix $\mathcal{O}_{sec}$ as determined from (5.3) has a full rank of 4, i.e., all states and parameters are observable. The determinant

$$\det\left(\mathcal{O}_{sec4\times4}\right) = -11.7\,Q_{SD}\,\rho_{sec}$$

will only be zero if Q_{SD} or ρ_{sec} is zero. Therefore, the system is expected to be observable for normal operating conditions. This result is significant as it means that the unmeasured flow of medium into the secondary tank, $Q_{in(sec)}$, is observable.

5.5   DILUTE MEDIUM TANK MODEL OBSERVABILITY

Similarly, the model for the dilute medium tank was linearised and assessed for observability. For this observability analysis, the value of k_v in (3.19) is not unknown, and is therefore included as an additional state in the observability analysis. Additionally, as with the correct medium and secondary tanks, the flow into the dilute medium tank, $Q_{in(DM)}$, is not known, and so can be included as an additional state. Similarly, the unmeasured density of the dilute medium tank is also modelled as an additional state. The dilute medium tank model in (3.19) and (3.20) is thus augmented such that

$z_{DM} = [x_{DM}^T, k_v, d_{DM}^T]^T$. The augmented state-space model is therefore:

$$\dot{z}_{DM} = f'_{DM}(t, z_{DM}, u_{DM}) \tag{5.13}$$

$$= \begin{bmatrix} \frac{1}{A_{DM}} \left(Q_{in(DM)} - Q_{DM} + k_v l_{DM} \right) \\ \frac{1}{k_{j(DM)}} \left(\rho_{DM} g(H_{p(DM)} - h_{dis(DM)} + h_{lev(DM)}) - k_p Q_{DM}^2 \right) \\ 0 \\ 0 \\ 0 \end{bmatrix}$$

$$y_{DM} = g_{DM}(t, z_{DM}, u_{DM}) \tag{5.14}$$

$$= h_{lev(DM)}$$

where $z_{DM} = \left[h_{lev(DM)}, \ Q_{DM}, \ k_v, \ \rho_{DM}, \ Q_{in(DM)} \right]^T$, $u_{DM} = [n_{DM}, \ l_{DM}]^T$, and $y_{DM} = h_{lev(DM)}$. The linearized model matrices as per (5.2) is given below after substitution of the known parameter values in Table 3.6:

$$A_{DM} = \begin{bmatrix} 0 & -0.24 & 0.24\,l_{DM} & 0 & 0.24 \\ 0.02\,\rho_{DM} & a_{22(DM)} & 0 & a_{24(DM)} & 0 \\ 0 & 0 & 0 & 0 & 0 \\ 0 & 0 & 0 & 0 & 0 \\ 0 & 0 & 0 & 0 & 0 \end{bmatrix} \tag{5.15}$$

$$B_{DM} = \begin{bmatrix} 0 & 0.242\,k_v \\ 0.21\,n_{DM}\,\rho_{DM} & 0 \\ 0 & 0 \\ 0 & 0 \\ 0 & 0 \end{bmatrix} \tag{5.16}$$

$$C_{DM} = \begin{bmatrix} 1 & 0 & 0 & 0 & 0 \end{bmatrix},$$

where

$$a_{22(DM)} = -280.0\,Q_{DM} - 4.08 \times 10^{-6}\,Q_{DM}\,\rho_{DM}$$

$$a_{24(DM)} = -2.04 \times 10^{-6}\,Q_{DM}^2 + 0.105\,n_{DM}^2 + 0.0204\,h_{lev(DM)} - 0.295$$

The observability matrix $\mathcal{O}_{DM}$ as determined from (5.3) has a rank of 3, i.e., the dilute medium tank system is not observable if the medium flow into the dilute medium tank ($Q_{in(DM)}$), the combined valve coefficient (k_v), and the dilute medium density (ρ_{DM}) are all not definitively known. The model is,

therefore, further simplified by combining the flow rate of water into the tank from the dilute valve (Q_{water}) with the flow of medium into the tank $Q_{in(DM)}$ such that:

$$\dot{\boldsymbol{x}}_{DM} = f_{DM}(t, \boldsymbol{x}_{DM}, \boldsymbol{u}_{DM}) \tag{5.17}$$

$$= \begin{bmatrix} \frac{1}{A_{DM}}\left(Q_{in(DM)} - Q_{DM}\right) \\ \frac{1}{k_{j(DM)}}\left(\rho_{DM}g(H_{p(DM)} - h_{DM}) - k_p Q_{DM}^2\right) \end{bmatrix}$$

$$\boldsymbol{y}_{DM} = g_{DM}(t, \boldsymbol{x}_{DM}, \boldsymbol{u}_{DM}) \tag{5.18}$$

$$= h_{lev(DM)},$$

with the model states, input, disturbances and outputs given by $\boldsymbol{x}_{DM} = \left[h_{lev(DM)}, Q_{DM}\right]^T$, $\boldsymbol{u}_{DM} = n_{DM}$, $\boldsymbol{d}_{DM} = \left[\rho_{DM}, Q_{in(DM)}\right]^T$, and $\boldsymbol{y}_{DM} = h_{lev(DM)}$. The unmeasured variables, $Q_{in(DM)}$ and ρ_{DM}, are modelled as process disturbances. Augmenting this model such that $\boldsymbol{z}_{DM} = [\boldsymbol{x}_{DM}^T, \boldsymbol{d}_{DM}^T]^T$, the determinant of the resultant matrix

$$\det\left(\mathcal{O}_{DM4\times4}\right) = 1.2 \times 10^{-32} Q_{DM}{}^2 h_{lev(DM)} \tag{5.19}$$

$$- 1.8 \times 10^{-35} Q_{DM}{}^2 \rho_{DM} + 1.6 \times 10^{-36} Q_{DM}{}^2 h_{lev(DM)}\rho_{DM} - 1.6 \times 10^{-36} Q_{DM}{}^4 \rho_{DM}$$

$$- 1.9 \times 10^{-31} Q_{DM}{}^2 - 1.2 \times 10^{-32} Q_{DM}{}^4$$

$$- 1.4 \times 10^{-31} Q_{DM}{}^2 n_{DM}{}^2 + 6.7 \times 10^{-39} Q_{DM}{}^2 \rho_{DM}{}^2$$

$$+ 4.9 \times 10^{-40} Q_{DM}{}^4 \rho_{DM}{}^2 - 4.9 \times 10^{-40} Q_{DM}{}^2 h_{lev(DM)}\rho_{DM}{}^2$$

$$+ 6.6 \times 10^{-35} Q_{DM}{}^2 n_{DM}{}^2 \rho_{DM} - 6.7 \times 10^{-39} Q_{DM}{}^2 n_{DM}{}^2 \rho_{DM}{}^2$$

is very near zero for all operating conditions, and, thus, the further simplified dilute medium system in (5.17) is also unobservable.

5.6 MIXING BOX MODEL OBSERVABILITY

The mixing box model (seen in (3.25) and (3.26)) includes the parameter k_{MB}, which is unknown and may change depending on conditions in the mixing box, such as blockages. To determine if k_{MB} is observable, it is included as a state in the model. The mixing box model in (3.25) and (3.26) is thus

augmented such that $\mathbf{z}_{MB} = [\mathbf{z}_{DM}^T, k_{MB}, \mathbf{d}_{MB}^T]^T$. The augmented state-space model is therefore:

$$\dot{\mathbf{z}}_{MB} = f'_{MB}(t, \mathbf{z}_{MB}, u_{MB}) \tag{5.20}$$

$$= \begin{bmatrix} \frac{1}{A_{MB}}\left(Q_{CM} + Q_{ore,in(MB)} - k_{MB}\sqrt{h_{lev(MB)}}\right) \\ 0 \\ 0 \\ 0 \end{bmatrix}$$

$$\mathbf{y}_{MB} = g_{MB}(t, \mathbf{z}_{MB}, u_{MB}) \tag{5.21}$$

$$= \begin{bmatrix} \rho_{MB}g(H_{MB} + h_{lev(MB)}) \\ \rho_{MB} \\ Q_{CM} \end{bmatrix}$$

where $\mathbf{z}_{MB} = \begin{bmatrix} h_{lev(MB)}, & k_{MB}, & \rho_{MB}, & Q_{CM} \end{bmatrix}^T$, $\mathbf{u}_{DM} = Q_{ore,in(MB)}$, and $\mathbf{y}_{MB} = [P_{MB}, \rho_{MB}, Q_{CM}]^T$. The linearized model matrices as per (5.2) is given below after substitution of the known parameter values in Table 3.8:

$$\mathbf{A}_{MB} = \begin{bmatrix} -\frac{1.17\,k_{MB}}{\sqrt{h_{lev(MB)}}} & -2.33\sqrt{h_{lev(MB)}} & 0 & 2.33 \\ 0 & 0 & 0 & 0 \\ 0 & 0 & 0 & 0 \\ 0 & 0 & 0 & 0 \end{bmatrix} \tag{5.22}$$

$$\mathbf{B}_{MB} = \begin{bmatrix} 2.33 \\ 0 \\ 0 \end{bmatrix} \tag{5.23}$$

$$\mathbf{C}_{MB} = \begin{bmatrix} 9.81\,\rho_{MB} & 0 & 9.81\,h_{lev(MB)} + 14.7 & 0 \\ 0 & 0 & 1 & 0 \\ 0 & 0 & 0 & 1 \end{bmatrix}. \tag{5.24}$$

The observability matrix $\mathcal{O}_{MB}$ as determined from (5.3) has a full rank of 3, i.e., all states and parameters are observable. The determinant

$$\det\left(\mathcal{O}_{MB3\times3}\right) = -224\sqrt{h_{lev(MB)}}\,\rho_{MB}^2$$

will only be zero if $h_{lev(MB)}$ or ρ_{MB} is zero. Therefore, the system is expected to be observable for normal operating conditions. This result is significant as it means that the unknown mixing box outlet coefficient constant, k_{MB}, is observable, as is the unmeasured mixing box level $h_{lev(MB)}$.

5.7   CHAPTER SUMMARY

The individual unit models were assessed for observability. The models of the primary and secondary densifiers, the drain-and-rinse screens, and the magnetic separator (modelled in steady-state) have very limited instrumentation, and thus it is not possible to confirm the outputs of these models online. Additionally, the dilute medium tank model is not observable. However, the observability analysis indicates that the correct medium and secondary tank models are fully observable, including for the augmented models where the flows into these tanks ($Q_{in(CM)}$ and $Q_{in(sec)}$ respectively) are considered as unmeasured states. The mixing box model is also fully observable, including for the augmented model where the parameter k_{MB} (see (5.20)) is not known and included as an unmeasured state. This dissertation aims to determine if medium losses in the circuit are observable, and so future chapters will investigate if the level of observability in the circuit is adequate to detect losses, and what additional instrumentation may be required to fully allow for this.

CHAPTER 6   MODEL STATE ESTIMATION

6.1   CHAPTER OVERVIEW

Due to the presence of process and measurement noise present in real systems, as well as the fact that not all states are directly measured (Schneider and Georgakis, 2013), it is necessary to design an observer so that the state variables can be estimated at all times. This is to allow for the analysis of medium flows within the circuit, and the detection of medium losses in the circuit (as described in Chapter 7). Furthermore, most model-based control systems require full state feedback, and if all the states are not measured, then the unmeasured states need to be estimated for a controller to function. While development of a controller is not included in this dissertation, this could be the focus of future work.

In this chapter, the extended Kalman filter (EKF) is used as the state estimator for the DMS tanks and mixing box. Section 6.2 gives an overview of the EKF, and Sections 6.3, 6.4, 6.5, and 6.6 present the estimation results of the implemented EKFs for the correct medium tank, secondary tank, dilute medium tank, and mixing box, respectively. For all of these units, the EKF is applied first to simulation data, and then to plant data.

6.2   EXTENDED KALMAN FILTER IMPLEMENTATION

The observability analysis conducted in Chapter 5 indicates that all states for the correct medium tank, secondary tank, and mixing box are observable, and therefore state estimation is feasible for these augmented models. The augmented models for these DMS circuit units (see Chapter 5) are non-linear, and therefore the EKF is used as the observer for these models.

The EKF, as the name suggests, is a version of the Kalman filter adapted for non-linear systems, and provides an estimate using a discretised, linearised version of the system at every time instance

(Ribeiro, 2004). The linearised continuous time system and output equations for the correct medium tank, secondary tank, and mixing box systems, given in Chapter 5, therefore need to be discretised for use in the EKF. The discrete system and measurement equations are:

$$
\begin{aligned}
z_k &= f_{k-1}(z_{k-1}, u_{k-1}, w_{k-1}) \\
y_k &= g_k(z_k, u_k, v_k),
\end{aligned}
\tag{6.1}
$$

where the process noise $w_k \sim (0, Q_k)$ is white noise with covariance $Q_k > 0$ and the measurement noise $v_k \sim (0, R_k)$ is white noise with covariance $R_k > 0$.

The trapezoidal rule is used to discretize each nonlinear model in Chapter 3 as presented in continuous time form by (5.1):

$$
z_k = z_{k-1} + \frac{T_s}{2}[f(t_k, z, u)\,|_{z_k, u_k} + w_k + f(t_{k-1}, z, u)\,|_{z_{k-1}, u_{k-1}} + w_{k-1}],
\tag{6.2}
$$

where T_s is the sampling time. The discretisation equation in (6.2) is solved using the Newton-Raphson method (Ungarala, 2012).

At each iteration of the EKF, a time update followed by a measurement update of the general state estimate $\hat{z}_k$ and estimation-error covariance matrix $\boldsymbol{P}_k$ is performed. For these updates, the Jacobian of the general system state equations is required:

$$
\boldsymbol{F}_{k-1} = \left. \frac{\delta f_{k-1}}{\delta z_{k-1}} \right|_{\hat{z}_{k-1}^+, u_{k-1}, 0},
\tag{6.3}
$$

$$
\boldsymbol{L}_{k-1} = \left. \frac{\delta f_{k-1}}{\delta w_{k-1}} \right|_{\hat{z}_{k-1}^+, u_{k-1}, 0}.
$$

As the system is discretised using the trapezoidal rule, the Jacobians in (6.3) are calculated as:

$$
\boldsymbol{F}_{k-1} = \frac{\delta f_{k-1}}{\delta z_{k-1}} = -\left[\boldsymbol{I} - \frac{T_s}{2}\frac{\delta f}{\delta z_k}\Big|_{\hat{z}_k^-, u_k}\right]^{-1}\left[-\boldsymbol{I} - \frac{T_s}{2}\frac{\delta f}{\delta z_k}\Big|_{\hat{z}_{k-1}^+, u_{k-1}}\right],
\tag{6.4}
$$

$$
\boldsymbol{L}_{k-1} = \frac{\delta f_{k-1}}{\delta w_{k-1}} = -\left[\boldsymbol{I} - \frac{T_s}{2}\frac{\delta f}{\delta z_k}\Big|_{\hat{z}_k^-, u_k}\right]^{-1}\left[-\frac{T_s}{2}\boldsymbol{I}\right].
\tag{6.5}
$$

Using the Jacobian matrices, the state estimate $\hat{z}_k$ and estimation-error covariance matrix $\boldsymbol{P}_k$ are initialised, and the time update of these is performed:

$$
\hat{z}_k^- = f_{k-1}(\hat{z}_{k-1}^+, u_{k-1}, 0)
\tag{6.6}
$$

$$
\boldsymbol{P}_k^- = \boldsymbol{F}_{k-1}\boldsymbol{P}_{k-1}^+\boldsymbol{F}_{k-1}^T + \boldsymbol{L}_{k-1}\boldsymbol{Q}_{k-1}\boldsymbol{L}_{k-1}^T
$$

For the measurement update, the Jacobian of the output equations is required:

$$\boldsymbol{S}_k = \frac{\delta g_k}{\delta \boldsymbol{z}_k}\bigg|_{\hat{\boldsymbol{z}}_k^-,\boldsymbol{u}_k,0} \tag{6.7}$$

$$\boldsymbol{M}_k = \frac{\delta g_k}{\delta \boldsymbol{v}_k}\bigg|_{\hat{\boldsymbol{z}}_k^-,\boldsymbol{u}_k,0}.$$

The measurement update for the EKF is therefore:

$$\boldsymbol{K}_k = \boldsymbol{P}_k^- \boldsymbol{S}_k^T (\boldsymbol{S}_k \boldsymbol{P}_k^- \boldsymbol{S}_k^T + \boldsymbol{M}_k R_k \boldsymbol{M}_k^T)^{-1} \tag{6.8}$$

$$\hat{\boldsymbol{z}}_k^+ = \hat{\boldsymbol{z}}_k^- + \boldsymbol{K}_k[\boldsymbol{y}_k - g_k(\hat{\boldsymbol{z}}_k^-,\boldsymbol{u}_k,0)]$$

$$\boldsymbol{P}_k^+ = (\boldsymbol{I} - \boldsymbol{K}_k \boldsymbol{C}_k)\boldsymbol{P}_k^- (\boldsymbol{I} - \boldsymbol{K}_k \boldsymbol{C}_k)^T + \boldsymbol{K}_k R_k \boldsymbol{K}_k^T.$$

6.3   CORRECT MEDIUM TANK STATE ESTIMATION

To implement the EKF on the correct medium tank, the discretisation in (6.2) is applied to the correct medium tank augmented model equations in (5.4). Using the sampling time of T_s, the discretised correct medium tank system equations are therefore as follows:

$$\boldsymbol{z}_{CM,k} = \boldsymbol{z}_{CM,k-1} + \frac{T_s}{2}\big[f'_{CM}(t_k,\boldsymbol{z}_{CM},\boldsymbol{u}_{CM})\,|_{\boldsymbol{z}_{CM,k},\boldsymbol{u}_{CM,k}} + \boldsymbol{w}_{CM,k} + f'_{CM}(t_{k-1},\boldsymbol{z}_{CM},\boldsymbol{u}_{CM})\,|_{\boldsymbol{z}_{CM,k-1},\boldsymbol{u}_{CM,k-1}} + \boldsymbol{w}_{CM,k-1}\big]$$

$$\tag{6.9}$$

$$\boldsymbol{z}_{CM,k} = \boldsymbol{z}_{CM,k-1} + \frac{T_s}{2}\begin{bmatrix} \frac{1}{A_{CM}}\left(Q_{in(CM),k} - Q_{CM,k} - Q_{PD,k}\right) \\ \frac{1}{k_{j(CM)}}\left(\rho_{CM,k}g(H_{p(CM),k} - h_{dis(CM)} + h_{lev(CM),k}) - k_p Q_{CM,k}^2\right) \\ \frac{1}{k_{j(PD)}}\left(\rho_{CM,k}g(H_{p(PD),k} - h_{dis(PD)} + h_{lev(CM),k}) - k_p Q_{PD,k}^2\right) \\ 0 \\ 0 \end{bmatrix} + \frac{T_s}{2}\boldsymbol{w}_{CM,k}$$

$$+ \frac{T_s}{2}\begin{bmatrix} \frac{1}{A_{CM}}\left(Q_{in(CM),k-1} - Q_{CM,k-1} - Q_{PD,k-1}\right) \\ \frac{1}{k_{j(CM)}}\left(\rho_{CM,k-1}g(H_{p(CM),k-1} - h_{dis(CM)} + h_{lev(CM),k-1}) - k_p Q_{CM,k-1}^2\right) \\ \frac{1}{k_{j(PD)}}\left(\rho_{CM,k-1}g(H_{p(PD),k-1} - h_{dis(PD)} + h_{lev(CM),k-1}) - k_p Q_{PD,k-1}^2\right) \\ 0 \\ 0 \end{bmatrix} + \boldsymbol{w}_{CM,k-1}$$

$$\boldsymbol{y}_{CM,k} = \begin{bmatrix} h_{lev(CM),k} \\ \rho_{CM,k}g\left(H_{max,PD}n_{PD,k}^2 - \frac{Q_{PD,k}^2}{2A_{PD}^2 g} - h_{dis(PD)} + h_{lev(CM),k}\right) \\ \rho_{CM,k} \end{bmatrix}$$

Similarly, the Jacobians of the discrete system state equations for the correct medium tank system are calculated as in (6.3), and are as follows:

$$\boldsymbol{F}_{CM,k-1} = -\left[\boldsymbol{I} - \frac{T_s}{2}\boldsymbol{A}_{CM}\,|_{\hat{\boldsymbol{z}}_{CM,k}^-,\boldsymbol{u}_{CM,k}}\right]^{-1}\left[\boldsymbol{I} - \frac{T_s}{2}\boldsymbol{A}_{CM}\,|_{\hat{\boldsymbol{z}}_{CM,k-1}^-,\boldsymbol{u}_{CM,k-1}}\right] \tag{6.10}$$

$$\boldsymbol{L}_{CM,k-1} = T_s\left[\boldsymbol{I} - T_s\boldsymbol{A}_{CM}\,|_{\hat{\boldsymbol{z}}_{CM,k}^-,\boldsymbol{u}_{CM,k}}\right]^{-1}\left[-\frac{T_s}{2}\boldsymbol{I}\right], \tag{6.11}$$

where $\boldsymbol{A}_{CM}$ is as defined in (5.7). The Jacobians of the discrete system output equations for the correct medium tank system (calculated as in (6.7)) are as follows:

$$\boldsymbol{S}_{CM,k} = \left.\frac{\delta g_{CM,k}}{\delta \boldsymbol{z}_{CM,k}}\right|_{\hat{\boldsymbol{z}}_{CM,k}^-,\boldsymbol{u}_{CM,k},0} \tag{6.12}$$

$$\boldsymbol{S}_{CM,k} = \begin{bmatrix} 1 & 0 & 0 & 0 & 0 \\ \rho_{CM,k}g & 0 & -\rho_{CM,k}\frac{2Q_{PD,k}}{2A_{PD}^2} & g\left(H_{max,PD}n_{PD,k}^2 - \frac{Q_{PD,k}^2}{2A_{PD}^2 g} - h_{dis(PD)} + h_{lev(CM)}\right) & 0 \\ 0 & 0 & 0 & 1 & 0 \end{bmatrix}$$

$$\boldsymbol{M}_{CM,k} = \left.\frac{\delta g_{CM,k}}{\delta \boldsymbol{v}_{CM,k}}\right|_{\hat{\boldsymbol{z}}_{CM,k}^-,\boldsymbol{u}_{CM,k},0} \tag{6.13}$$

$$\boldsymbol{M}_{CM,k} = \begin{bmatrix} 1 & 0 & 0 \\ 0 & 1 & 0 \\ 0 & 0 & 1 \end{bmatrix}.$$

Data was sampled at a rate of $T_s = 5$ s. The filter was initialized at:

$$\boldsymbol{z}_{CM,0} = \begin{bmatrix} 1 & 0.017 & 0.017 & 3.4 & 0.02 \end{bmatrix}^T$$

$$\boldsymbol{P}_{CM,0} = \text{diag}\begin{bmatrix} 1 & 0.1 & 0.1 & 10 & 0.1 \end{bmatrix}$$

The measurement noise covariance matrix $\boldsymbol{R}_{CM}$ is based on the noise seen in the instrumentation. The process noise covariance matrix $\boldsymbol{Q}_{CM}$ assumes equal uncertainty in $h_{lev(CM)}$, Q_{CM}, and Q_{PD}, while ρ_{CM} and $Q_{in(CM)}$ are both assumed to have uncertainty one order of magnitude greater. $\boldsymbol{Q}_{CM}$ is also scaled according to the range of each process variable.

$$\boldsymbol{R}_{CM} = \text{diag}\begin{bmatrix} 7.87 \times 10^{-4} & 0.0125 & 2.03 \times 10^{-6} \end{bmatrix}$$

$$\boldsymbol{Q}_{CM} = \text{diag}\begin{bmatrix} 0.1 & 0.01 & 0.01 & 100 & 1 \end{bmatrix}$$

6.3.1 EKF implementation on correct medium tank simulation

The EKF algorithm was applied to the simulated correct medium tank system. Band-limited additive Gaussian measurement and process noise were added to the simulation states and outputs (that is, to

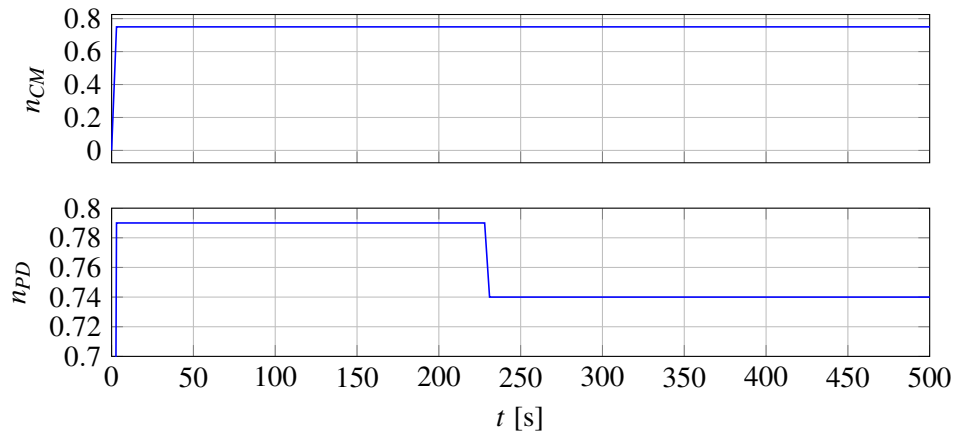$h_{lev(CM)}$, Q_{CM} and Q_{PD}). The inputs to the simulation are given in Figure 6.1.

Figure 6.1. Simulation data of inputs to correct medium tank system.

The results of the EKF implementation on the simulated correct medium tank system states and outputs are shown in Figure 6.2. The EKF estimates of the correct medium tank level, the correct medium and primary densifier pump flow rates, the correct medium tank density, and the primary densifier pump discharge pressure ($h_{lev(CM)}$, Q_{CM}, Q_{PD}, ρ_{CM}, and P_{PD} respectively in Figure 6.2) track the simulation data well. The EKF estimate of the flow rate of slurry into the correct medium tank ($Q_{in(CM)}$, in Figure 6.2) is less accurate, as there is noise (of greater magnitude than the additive Gaussian noise added to the simulation) present in the estimate. This noise can be seen in Figure 6.2. It should be noted, however, that the y-axis scale is small in magnitude.
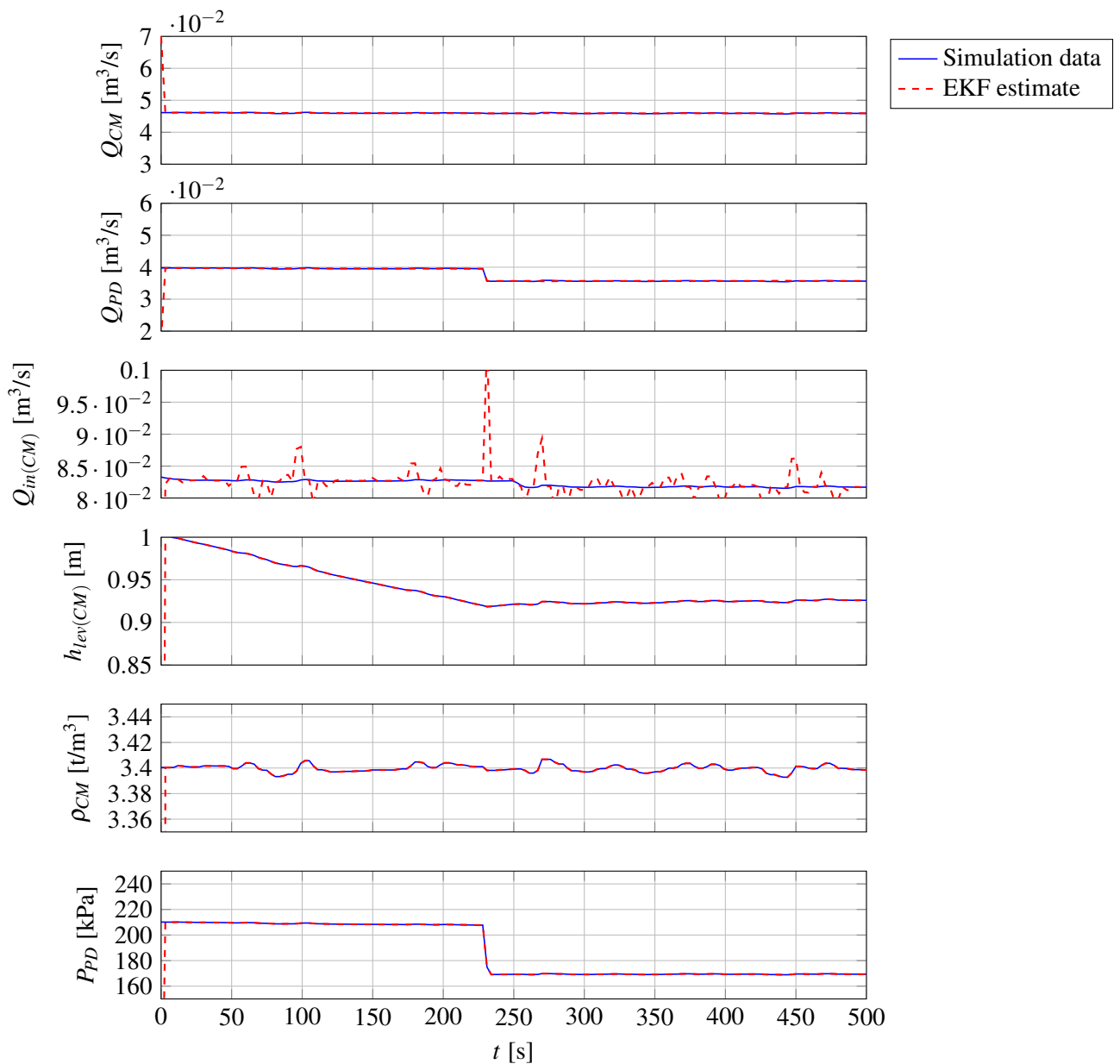
**Figure 6.2.** Simulation data and EKF estimates of correct medium tank system states and outputs.

Table 6.1 gives the RMSE and NRMSE for the EKF predictions of the outputs and states of the simulation.

Table 6.1. RMSE and NRMSE values for correct medium tank EKF on simulation.

Variable	RMSE	NRMSE
$h_{lev(CM)}$	0.00035 m	7.6087×10^{-5}
P_{PD}	0.3348 kPa	0.0025
Q_{CM}	3.154×10^{-4} m^3/s	0.0052
Q_{PD}	3.131×10^{-4} m^3/s	0.0068
$Q_{in(CM)}$	0.002 m^3/s	0.0189

6.3.2 EKF implementation on correct medium tank plant data

The EKF algorithm was then applied to the correct medium tank system, using plant data. The inputs to the system are seen in Figure 6.3:
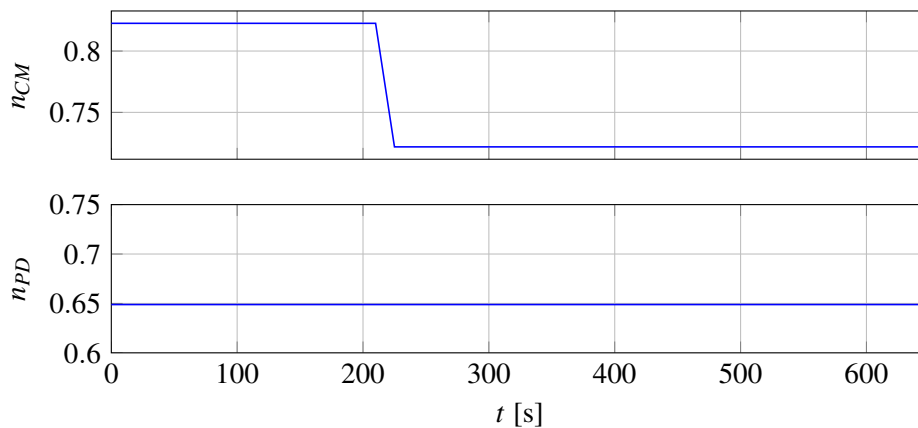
Figure 6.3. Plant data of inputs to correct medium tank system.

The EKF state estimation of the correct medium tank system states and outputs are seen in Figure 6.4.
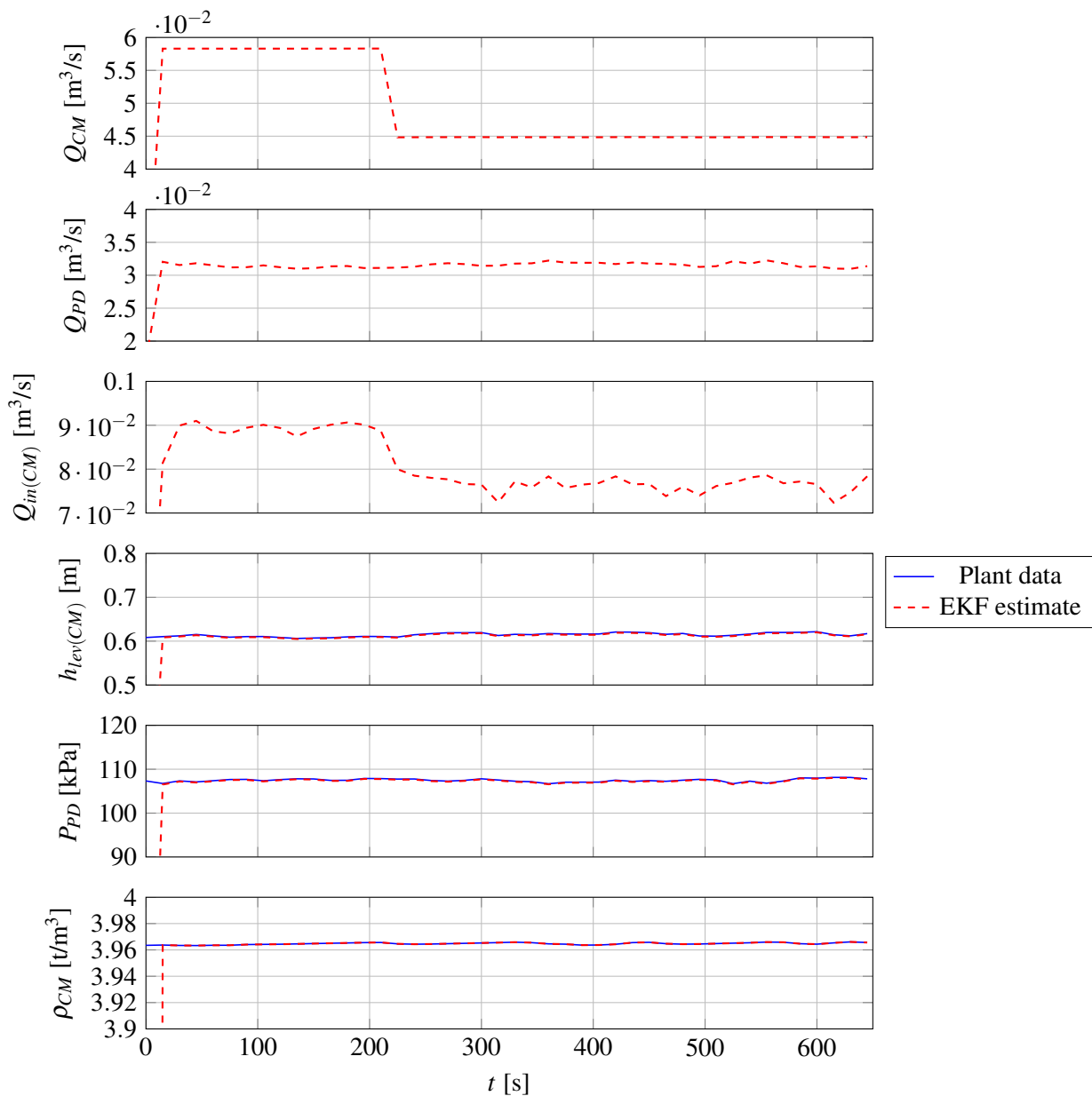
Figure 6.4. EKF state estimates of correct medium tank system.

The response in the flow rates to the system inputs (in Figure 6.3) is as expected: the correct medium pump flow rate estimation (Q_{CM} in Figure 6.4) decreases with n_{CM} (at top in Figure 6.3). The primary densifier pump flow rate (Q_{PD} in Figure 6.4) estimation remains constant with n_{PD} (at bottom in Figure 6.3). The estimate of $Q_{in(CM)}$ is also as expected: $Q_{in(CM)}$ decreases when Q_{CM} decreases, as the medium flow from the mixing box to the correct medium tank decreases.

The EKF estimates (red) of the system outputs tracks the plant data (blue) effectively, for both the correct medium tank level and the primary densifier pump discharge pressure ($h_{lev(CM)}$ and P_{PD} in Figure 6.4). Table 6.2 gives the RMSE and NRMSE for the EKF predictions of the plant data of the correct medium tank system outputs.

Table 6.2. RMSE and NRMSE values for correct medium tank EKF on plant data.

Variable	RMSE	NRMSE
$h_{lev(CM)}$	$2.7 \times 10^{-7}\%$	6.43×10^{-9}
P_{PD}	2.5702 kPa	0.0190

6.4   SECONDARY TANK STATE ESTIMATION

To implement the EKF on the secondary tank system, the discretisation in (6.2) is applied to the augmented model equations in (5.9). Using the sampling time of T_s, the discretised secondary tank system equations are therefore as follows:

$$\mathbf{z}_{sec,k} = \mathbf{z}_{sec,k-1} + \frac{T_s}{2}\left[f'_{sec}(t_k, \mathbf{z}_{sec}, \mathbf{u}_{sec})\,|_{\mathbf{z}_{sec,k}, \mathbf{u}_{sec,k}} + \mathbf{w}_{sec,k} + f'_{sec}(t_{k-1}, \mathbf{z}_{sec}, \mathbf{u}_{sec})\,|_{\mathbf{z}_{sec,k-1}, \mathbf{u}_{sec,k-1}} + \mathbf{w}_{sec,k-1} \right]$$

$$(6.14)$$

$$\mathbf{z}_{sec,k} = \mathbf{z}_{sec,k-1} + \frac{T_s}{2}\begin{bmatrix} \frac{1}{A_{sec}}\left(Q_{in(sec),k} - Q_{SD,k}\right) \\ \frac{1}{k_{j(SD)}}\left(\rho_{sec,k}g(H_{p(SD),k} - h_{dis(SD)} + h_{lev(sec),k}) - k_p Q^2_{SD,k}\right) \\ 0 \\ 0 \end{bmatrix}$$

$$+ \mathbf{w}_{sec,k} + \frac{T_s}{2}\begin{bmatrix} \frac{1}{A_{sec}}\left(Q_{in(sec),k-1} - Q_{SD,k-1}\right) \\ \frac{1}{k_{j(SD)}}\left(\rho_{sec,k-1}g(H_{p(SD),k-1} - h_{dis(SD)} + h_{lev(sec),k-1}) - k_p Q^2_{SD,k-1}\right) \\ 0 \\ 0 \end{bmatrix} + \mathbf{w}_{sec,k-1}$$

$$\mathbf{y}_{sec,k} = \begin{bmatrix} h_{lev(sec),k} \\ \rho_{sec,k}g\left(H_{SD}n^2_{SD,k} - \frac{Q^2_{SD,k}}{2A^2_{SD}g} - h_{dis(SD)} + h_{lev(sec),k}\right) \\ \rho_{sec,k} \end{bmatrix} \qquad (6.15)$$

Similarly, the Jacobians of the discrete system state equations for the secondary tank system are calculated as in (6.3), and are as follows:

$$\boldsymbol{F}_{sec,k-1} = -\left[\boldsymbol{I} - \frac{T_s}{2}\boldsymbol{A}_{sec}\mid_{\hat{\boldsymbol{z}}^-_{sec,k},\boldsymbol{u}_{sec,k}}\right]^{-1}\left[\boldsymbol{I} - \frac{T_s}{2}\boldsymbol{A}_{sec}\mid_{\hat{\boldsymbol{z}}^-_{sec,k-1},\boldsymbol{u}_{sec,k-1}}\right] \tag{6.16}$$

$$\boldsymbol{L}_{sec,k-1} = T_s\left[\boldsymbol{I} - T_s\boldsymbol{A}_{sec}\mid_{\hat{\boldsymbol{z}}^-_{sec,k},\boldsymbol{u}_{sec,k}}\right]^{-1}\left[-\frac{T_s}{2}\boldsymbol{I}\right], \tag{6.17}$$

where $\boldsymbol{A}_{sec}$ is as defined in (5.11). The Jacobians of the discrete system output equations for the secondary tank system (calculated as in (6.7)) are as follows:

$$\boldsymbol{S}_{sec,k} = \frac{\delta g_{sec,k}}{\delta z_{sec,k}}\bigg|_{\hat{\boldsymbol{z}}^-_{sec,k},\boldsymbol{u}_{sec,k},0} \tag{6.18}$$

$$\boldsymbol{S}_{sec,k} = \begin{bmatrix} 1 & 0 & 0 & 0 \\ g\rho_{sec,k} & -\rho_{sec,k}\frac{2Q_{SD,k}}{2A_{SD}^2} & g\left(H_{max,SD}n_{SD,k}^2 - \frac{Q_{SD,k}^2}{2A_{SD}^2 g} - h_{dis(SD)} + h_{lev(sec)}\right) & 0 \\ 0 & 0 & 0 & 1 \end{bmatrix}$$

$$\boldsymbol{M}_{sec,k} = \frac{\delta g_{sec,k}}{\delta v_{sec,k}}\bigg|_{\hat{\boldsymbol{z}}^-_{sec,k},\boldsymbol{u}_{sec,k},0} \tag{6.19}$$

$$\boldsymbol{M}_{sec,k} = \begin{bmatrix} 1 & 0 & 0 \\ 0 & 1 & 0 \\ 0 & 0 & 1 \end{bmatrix}.$$

Data was sampled at a rate of $T_s = 5$ s. The filter was initialized at:

$$\boldsymbol{z}_{sec,0} = \begin{bmatrix} 0.825 & 0.017 & 3.4 & 0.02 \end{bmatrix}^T$$

$$\boldsymbol{P}_{sec,0} = \text{diag}\begin{bmatrix} 1 & 0.1 & 10 & 0.1 \end{bmatrix}$$

The measurement noise covariance matrix $\boldsymbol{R}_{sec}$ is based on the noise seen in the instrumentation. The process noise covariance matrix $\boldsymbol{Q}_{sec}$ assumes equal uncertainty in $h_{lev(sec)}$ and Q_{SD}, while ρ_{sec} and $Q_{in(sec)}$ are both assumed to have uncertainty one order of magnitude greater. $\boldsymbol{Q}_{sec}$ is also scaled according to the range of each process variable.

$$\boldsymbol{R}_{sec} = \text{diag}\begin{bmatrix} 5.7 \times 10^{-3} & 1.94 & 2.15 \times 10^{-5} \end{bmatrix}$$

$$\boldsymbol{Q}_{sec} = \text{diag}\begin{bmatrix} 0.1 & 0.01 & 100 & 1 \end{bmatrix}$$

6.4.1 EKF implementation on secondary tank simulation

The EKF algorithm described in Section 6.2 was applied to the simulated secondary tank system. Band-limited additive Gaussian measurement and process noise were added to the simulation states

and outputs (i.e. to $h_{lev(sec)}$, Q_{SD}, and P_{SD}). The input to the simulation is seen in Figure 6.5.
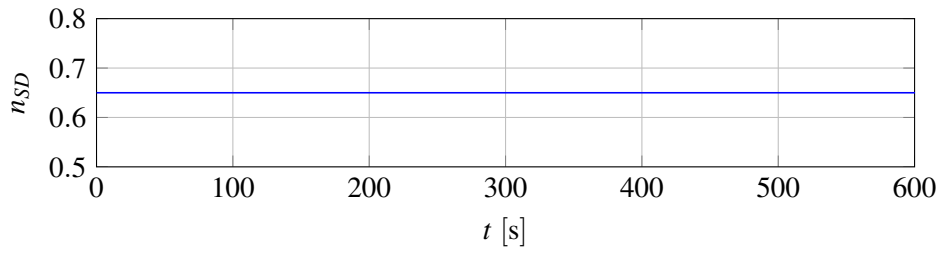

Figure 6.5. Simulation data of input to secondary tank system.

The EKF estimation of the secondary tank system states is seen in Figure 6.6.
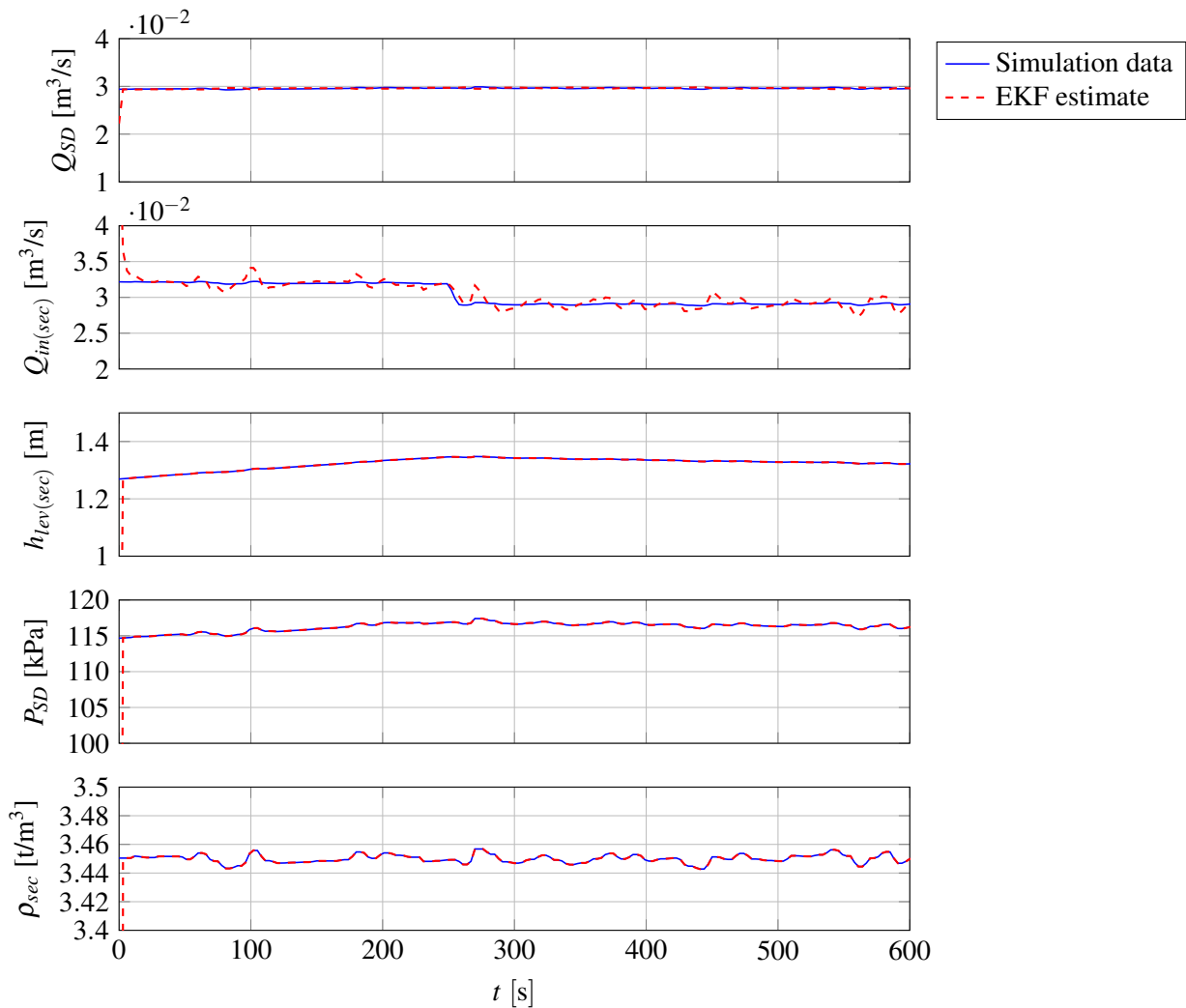

Figure 6.6. Simulation data and EKF estimates of secondary tank system states and outputs.

The EKF estimate (red) of the secondary densifier pump flow rate (Q_{SD} in Figure 6.6) adequately tracks the simulation (blue), as does that of the secondary tank level, and the secondary tank density ($h_{lev(sec)}$, and ρ_{sec} in Figure 6.6 respectively). As with the correct medium tank system (see Figure 6.2), the estimate of the flow rate of slurry into the secondary tank ($Q_{in(sec)}$ in Figure 6.6) is quite noisy. The noise present in the estimation is of greater magnitude than the additive Gaussian noise added to the simulation. Table 6.3 gives the RMSE and NRMSE for the EKF estimations of the outputs and states of the simulation.

Table 6.3. RMSE and NRMSE values for secondary tank EKF on simulation data.

Variable	RMSE	NRMSE
$h_{lev(sec)}$	0.00033 m	8.25×10^{-5}
P_{SD}	0.3264 kPa	0.0023
Q_{SD}	3.14×10^{-4} m^3/s	0.0071
$Q_{in(sec)}$	0.0013 m^3/s	0.0295

6.4.2 EKF implementation on secondary tank plant data

The EKF algorithm was then applied to the secondary tank system, using plant data. The input to the system (n_{SD}, the speed of the SD pump) is seen in Figure 6.7.
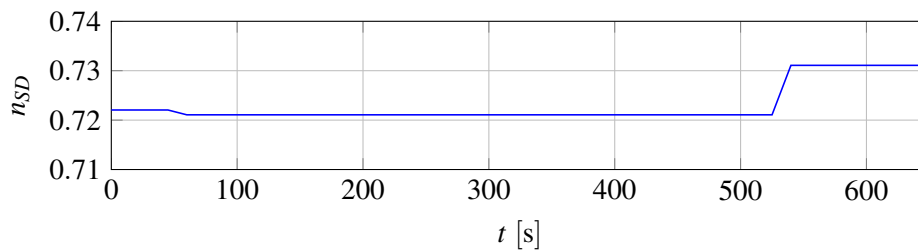
Figure 6.7. Plant data of input to secondary tank system.

The results of the EKF implementation on the simulated secondary tank system states can be seen in Figure 6.8.
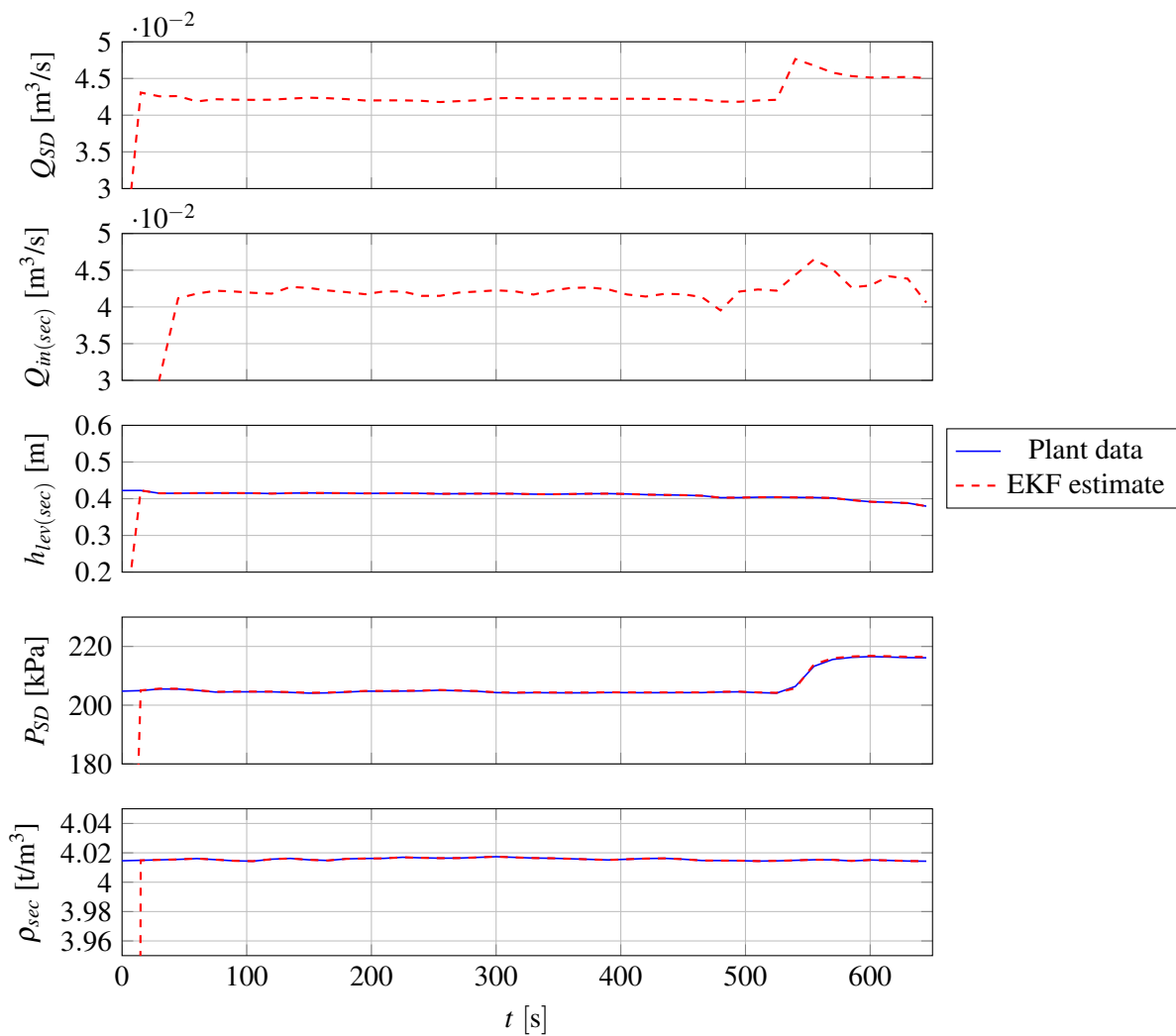
Figure 6.8. Plant data and EKF estimates of secondary tank system states and outputs.

The response in the estimated secondary densifier pump flow rate (Q_{SD}, in Figure 6.8) is as expected: the Q_{SD} estimation decreases, remains constant, and then increases with the secondary densifier pump speed (n_{SD} in Figure 6.7). The estimate of $Q_{in(sec)}$ is, however, quite noisy. The EKF estimate (red) of the plant outputs tracks the plant data (blue) effectively, for both the secondary tank level, the secondary densifier pump discharge pressure, and the secondary tank density ($h_{lev(sec)}$, P_{SD}, and ρ_{sec} in Figure 6.8 respectively). As expected, P_{SD} increases when n_{SD} is increased at $t = 510$ s, while $h_{lev(sec)}$ decreases.

Table 6.4 gives the RMSE and NRMSE for the EKF predictions of the plant data of the system outputs.

Table 6.4. RMSE and NRMSE values for secondary tank EKF on plant data.

Variable	RMSE	NRMSE
$h_{lev(sec)}$	9.5×10^{-9} m	4.1304×10^{-9}
P_{SD}	1.0712 kPa	0.0069

6.5 DILUTE MEDIUM TANK STATE ESTIMATION

To implement the EKF on the dilute medium tank, the discretisation in (6.2) is applied to the dilute medium tank augmented model equations in (5.17). Using the sampling time of T_s, the discretised dilute medium tank system equations are therefore as follows:

$$\mathbf{z}_{DM,k} = \mathbf{z}_{DM,k-1} + \frac{T_s}{2}\left[f'_{DM}(t_k, \mathbf{z}_{DM}, \mathbf{u}_{DM})\big|_{\mathbf{z}_{DM,k}, \mathbf{u}_{DM,k}} + \mathbf{w}_{DM,k} + f'_{DM}(t_{k-1}, \mathbf{z}_{DM}, \mathbf{u}_{DM})\big|_{\mathbf{z}_{DM,k-1}, \mathbf{u}_{DM,k-1}} + \mathbf{w}_{DM,k-1}\right]$$

(6.20)

$$\mathbf{z}_{DM,k} = \mathbf{z}_{DM,k-1} + \frac{T_s}{2}\begin{bmatrix} \frac{1}{A_{DM}}\left(Q_{in(DM),k} - Q_{DM,k}\right) \\ \frac{1}{k_{j(DM)}}\left(\rho_{DM,k}g(H_{p(DM),k} - h_{DM,k}) - k_p Q^2_{DM,k}\right) \\ 0 \\ 0 \end{bmatrix} + \mathbf{w}_{DM,k}$$

$$+ \frac{T_s}{2}\begin{bmatrix} \frac{1}{A_{DM}}\left(Q_{in(DM),k-1} - Q_{DM,k-1}\right) \\ \frac{1}{k_{j(DM)}}\left(\rho_{DM,k-1}g(H_{p(DM),k-1} - h_{DM,k-1}) - k_p Q^2_{DM,k-1}\right) \\ 0 \\ 0 \end{bmatrix} + \mathbf{w}_{DM,k-1}$$

$$\mathbf{y}_{DM,k} = \begin{bmatrix} h_{lev(DM),k} \end{bmatrix}.$$
(6.21)

Similarly, the Jacobians of the discrete system state equations for the dilute medium tank system are calculated as in (6.3), and are as follows:

$$\mathbf{F}_{DM,k-1} = -\left[I - \frac{T_s}{2}\mathbf{A}_{DM}\big|_{\hat{\mathbf{z}}^-_{DM,k}, \mathbf{u}_{DM,k}}\right]^{-1}\left[I - \frac{T_s}{2}\mathbf{A}_{DM}\big|_{\hat{\mathbf{z}}^-_{DM,k-1}, \mathbf{u}_{DM,k-1}}\right] \tag{6.22}$$

$$\mathbf{L}_{DM,k-1} = T_s\left[I - T_s\mathbf{A}_{DM}\big|_{\hat{\mathbf{z}}^-_{DM,k}, \mathbf{u}_{DM,k}}\right]^{-1}\left[-\frac{T_s}{2}I\right], \tag{6.23}$$

where A_{DM} is as defined in (5.15). The Jacobians of the discrete system output equations for the dilute medium tank system (calculated as in (6.7)) are as follows:

$$S_{DM,k} = \left. \frac{\delta g_{DM,k}}{\delta z_{DM,k}} \right|_{\hat{z}_{DM,k}^-, u_{DM,k}, 0} \tag{6.24}$$

$$S_{DM,k} = \begin{bmatrix} 1 & 0 & 0 & 0 \end{bmatrix}$$

$$M_{DM,k} = \left. \frac{\delta g_{DM,k}}{\delta v_{DM,k}} \right|_{\hat{z}_{DM,k}^-, u_{DM,k}, 0} \tag{6.25}$$

$$M_{DM,k} = 1.$$

Data was sampled at a rate of $T_s = 5$ s. The filter was initialized at:

$$z_{DM,0} = \begin{bmatrix} 1 & 0.017 & 2.62 & 0.02 \end{bmatrix}^T$$

$$P_{DM,0} = \text{diag} \begin{bmatrix} 1 & 0.1 & 10 & 0.1 \end{bmatrix}$$

The measurement noise covariance matrix R_{DM} is based on the noise seen in the instrumentation. The process noise covariance matrix Q_{DM} assumes equal uncertainty in $h_{lev(DM)}$ and Q_{DM}, while ρ_{DM} and $Q_{in(DM)}$ are both assumed to have uncertainty one order of magnitude greater. Q_{DM} is also scaled according to the range of each process variable.

$$R_{DM} = \text{diag} \begin{bmatrix} 8.57 \times 10^{-5} \end{bmatrix}$$

$$Q_{DM} = \text{diag} \begin{bmatrix} 0.1 & 0.01 & 100 & 1 \end{bmatrix}$$

6.5.1 EKF implementation on dilute medium tank simulation

The EKF algorithm was applied to the simulated dilute medium tank system. Band-limited additive Gaussian measurement and process noise was added to the simulation states and outputs (that is, to $h_{lev(DM)}$ and Q_{DM} and ρ_{DM}). The results of the EKF implementation on the system states and outputs are shown in Figure 6.2. Note that the inputs to the simulation were the same as in Figure 4.6.
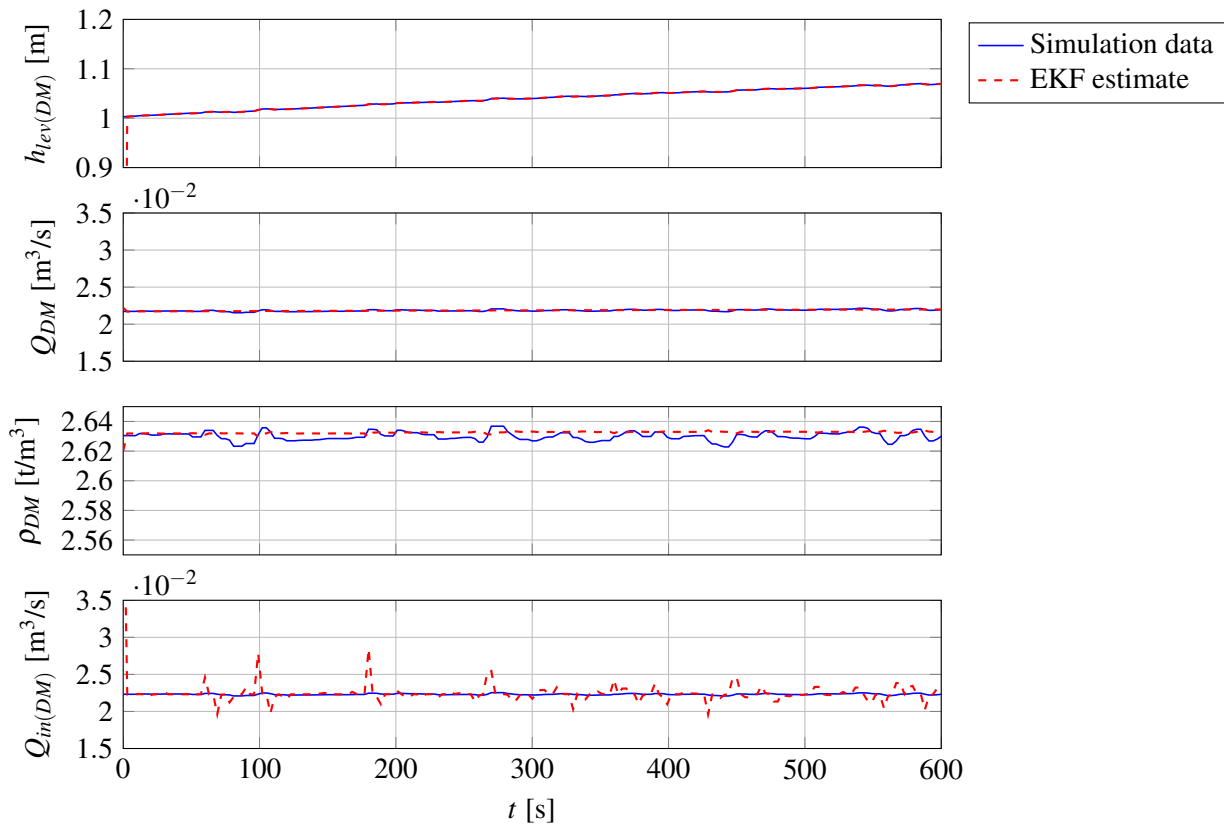
Figure 6.9. Simulation data and EKF estimates of dilute medium tank system states and outputs.

The EKF estimates of the dilute medium tank level and pump flow rate ($h_{lev(DM)}$ and Q_{DM} in Figure 6.9 respectively) track the simulation data well. The EKF estimate of the flow rate of slurry into the dilute medium tank ($Q_{in(DM)}$ in Figure 6.9) is more noisy, and there is noise (of greater magnitude than the additive Gaussian noise added to the simulation) present in the estimate. It should be noted, however, that the y-axis scale is small in magnitude.

While the EKF estimate of the dilute medium tank density (ρ_{DM} in Figure 6.9) tracks the simulation well, the EKF is initialised at 2.62 t/m^3 – very close to the simulated value of 2.63 t/m^3. Due to the fact that the dilute medium tank system is unobservable (see Section 5.5), only by initialising the EKF estimate of ρ_{DM} close to the simulated value for ρ_{DM} was the EKF able to produce an adequate estimate (as in Figure 6.9).

Table 6.5 gives the RMSE and NRMSE for the EKF predictions of the outputs and states of the dilute medium tank simulation.

Table 6.5. RMSE and NRMSE values for dilute medium tank EKF on simulation data.

Variable	RMSE	NRMSE
$h_{lev(DM)}$	0.00035 m	7.6087×10^{-5}
Q_{DM}	3.14×10^{-4} m^3/s	0.0052
$Q_{in(DM)}$	0.0022 m^3/s	0.0189

6.5.2   EKF implementation on dilute medium tank plant data

The EKF algorithm was then applied to the dilute medium tank system, using plant data. The inputs to the system are seen in Figure 6.10.
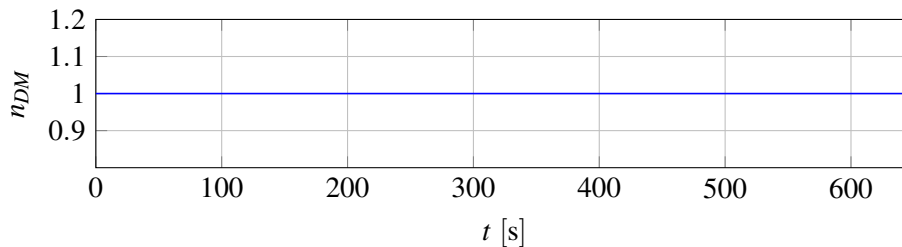
Figure 6.10. Plant data of inputs to dilute medium tank system.

The EKF state estimation of the dilute medium tank system states are seen in Figure 6.11.
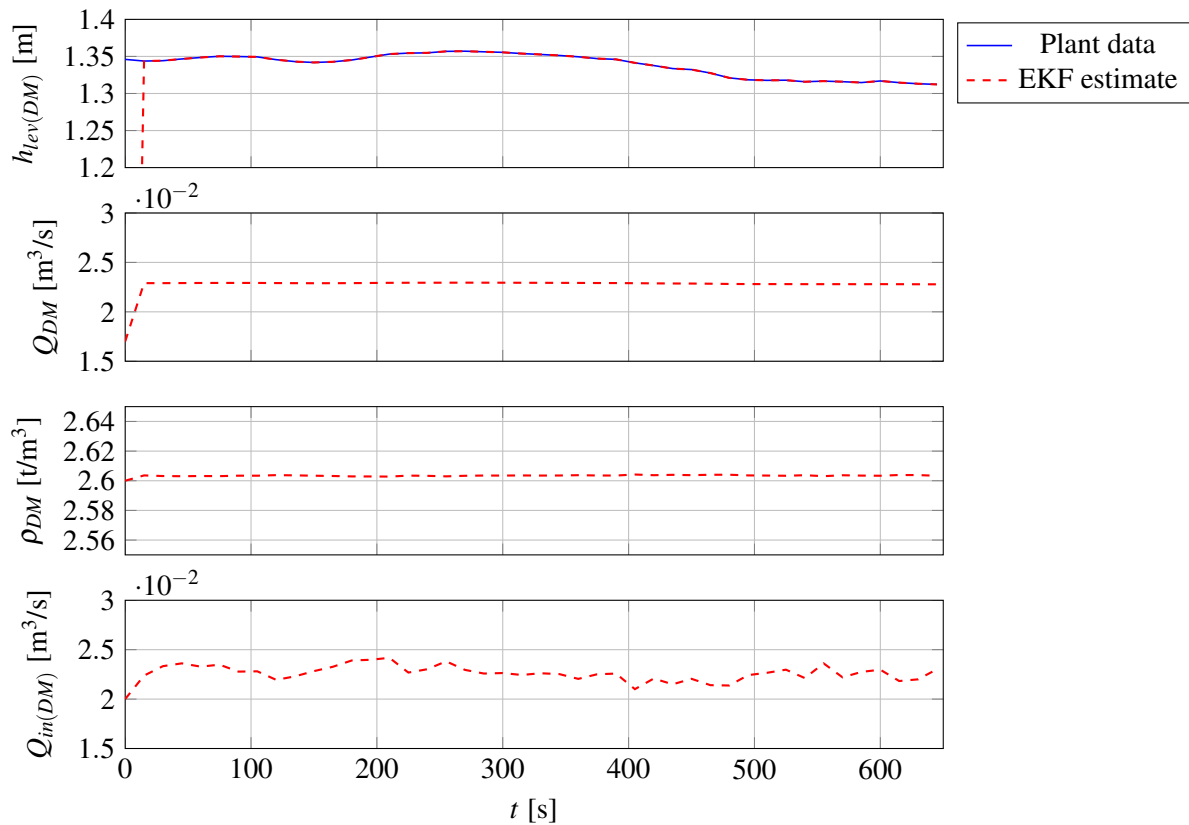
Figure 6.11. EKF state estimates of dilute medium tank system.

The EKF estimate (red) tracks the plant data (blue) of the dilute medium tank level ($h_{lev(DM)}$ in Figure 6.11) effectively. The dilute medium pump flow rate estimation (Q_{DM} in Figure 6.4) remains constant with the dilute medium pump speed (n_{DM} in Figure 6.10) as expected.

Note that the EKF estimate of ρ_{DM} does not deviate substantially from the initial value (see Figure 6.11). As shown in the EKF implementation on the dilute medium tank simulation data (see Figure 6.9), the EKF only produces adequate results for ρ_{DM} when it is initialised near the true value of ρ_{DM}, because the dilute medium tank system is not fully observable. With plant data, the true value of ρ_{DM} is not known (as ρ_{DM} is not measured), and so the EKF results for the dilute medium tank plant data (seen in Figure 6.11) are not reliable. This does not negatively affect the feasibility of detecting medium losses within the DMS circuit, because, as shown in Chapter 7, the effects of medium loss are not seen in the dilute medium tank system, and therefore accurate state estimation of the dilute medium tank system is not required to detect medium losses.

Table 6.6 gives the RMSE and NRMSE for the EKF predictions of the plant data of the dilute medium tank system outputs.

Table 6.6. RMSE and NRMSE values for dilute medium tank EKF on plant data.

Variable	RMSE	NRMSE
$h_{lev(CM)}$	2.7×10^{-7} m	6.43×10^{-9}
P_{PD}	2.5702 kPa	0.0190

6.6 MIXING BOX STATE ESTIMATION

To implement the EKF on the mixing box system, the discretisation in (6.2) is applied to the augmented mixing box system equations in (5.20) and (5.21). Using the sampling time of T_s, the discretised mixing box system equations are therefore as follows:

$$
\boldsymbol{z}_{MB,k} = \boldsymbol{z}_{MB,k-1} + \frac{T_s}{2}
\begin{bmatrix}
\frac{1}{A_{MB}}\left(Q_{CM,k} + Q_{ore,in(MB),k} - k_{MB,k}\sqrt{h_{lev(MB),k}}\right) \\
0 \\
0 \\
0
\end{bmatrix}
\tag{6.26}
$$

$$
+ \frac{T_s}{2}
\begin{bmatrix}
\frac{1}{A_{MB}}\left(Q_{CM,k-1} + Q_{ore,in(MB),k-1} - k_{MB,k-1}\sqrt{h_{lev(MB),k-1}}\right) \\
0 \\
0 \\
0
\end{bmatrix}
$$

$$
\boldsymbol{y}_{MB,k} =
\begin{bmatrix}
\rho_{MB,k}g(H_{MB} + h_{lev(MB),k}) \\
\rho_{MB,k} \\
Q_{CM,k}
\end{bmatrix}
\tag{6.27}
$$

Similarly, the Jacobians of the discrete system state equations for the mixing box system are calculated as in (6.3), and are as follows:

$$
\boldsymbol{F}_{MB,k-1} = -\left[I - \frac{T_s}{2}\boldsymbol{A}_{MB}\,|_{\hat{\boldsymbol{z}}_{MB,k}^-,\boldsymbol{u}_{MB,k}}\right]^{-1}\left[I - \frac{T_s}{2}\boldsymbol{A}_{MB}\,|_{\hat{\boldsymbol{z}}_{MB,k-1}^-,\boldsymbol{u}_{MB,k-1}}\right]
\tag{6.28}
$$

$$
\boldsymbol{L}_{MB,k-1} = T_s\left[I - T_s\boldsymbol{A}_{MB}\,|_{\hat{\boldsymbol{z}}_{MB,k}^-,\boldsymbol{u}_{MB,k}}\right]^{-1}\left[-\frac{T_s}{2}I\right],
\tag{6.29}
$$

where $\boldsymbol{A}_{MB}$ is as defined in (5.22). The Jacobians of the discrete system output equations for the mixing box system (calculated as in (6.7)) are as follows:

$$\boldsymbol{S}_{MB,k} = \left.\frac{\delta g_{MB,k}}{\delta z_{MB,k}}\right|_{\hat{z}_{MB,k}^-,\boldsymbol{u}_{MB,k},0} \tag{6.30}$$

$$\boldsymbol{S}_{MB,k} = \begin{bmatrix} g\rho_{MB,k} & 0 & g(H_{MB}+h_{lev(MB),k}) & 0 \\ 0 & 0 & 1 & 0 \\ 0 & 0 & 0 & 1 \end{bmatrix}$$

$$\boldsymbol{M}_{MB,k} = \left.\frac{\delta g_{MB,k}}{\delta v_{MB,k}}\right|_{\hat{z}_{MB,k}^-,\boldsymbol{u}_{MB,k},0} \tag{6.31}$$

$$\boldsymbol{M}_{MB,k} = \begin{bmatrix} 1 & 0 & 0 \\ 0 & 1 & 0 \\ 0 & 0 & 1 \end{bmatrix}$$

The filter was initialized at:

$$\boldsymbol{z}_{MB,0} = \begin{bmatrix} 0.688 & 0.03 & 3 & 0.06 \end{bmatrix}^T$$

$$\boldsymbol{P}_{MB,0} = \text{diag}\begin{bmatrix} 1 & 0.1 & 10 & 0.1 \end{bmatrix}$$

The measurement noise covariance matrix $\boldsymbol{R}_{MB}$ is based on the noise seen in the instrumentation. The process noise covariance matrix $\boldsymbol{Q}_{MB}$ assumes the uncertainty in k_{MB}, ρ_{MB} and Q_{CM} is one order of magnitude greater than that in $h_{lev(MB)}$. $\boldsymbol{Q}_{MB}$ is also scaled according to the range of each process variable.

$$\boldsymbol{R}_{MB} = \text{diag}\begin{bmatrix} 0.027 & 1.122 \times 10^{-5} & 1.204 \times 10^{-4} \end{bmatrix}$$

$$\boldsymbol{Q}_{MB} = \text{diag}\begin{bmatrix} 1 & 10 & 100 & 1 \end{bmatrix}$$

6.6.1   EKF implementation on mixing box simulation

The EKF algorithm was applied to the mixing box system simulation. Band-limited additive Gaussian measurement and process noise were added to the simulation inputs and outputs (i.e. to $Q_{med,in(MB)}$, $Q_{ore,in(MB)}$ and P_{MB}). The inputs to the mixing box system are seen in Figure 6.12.
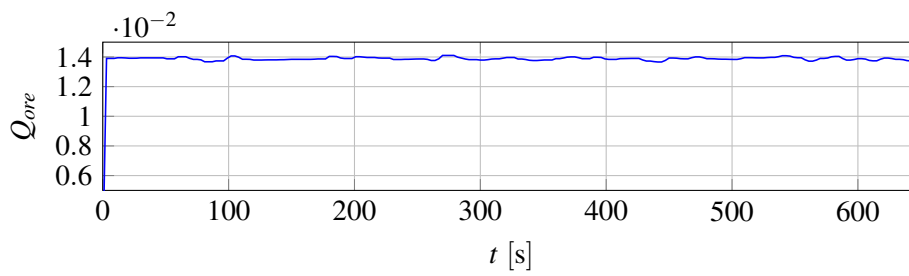
Figure 6.12. Simulation of inputs to mixing box system.

The results of the EKF implementation on the mixing box system states and outputs are shown in Figures 6.13. The EKF estimate (red) tracks the simulation (blue) effectively, for the mixing box level, outlet coefficient, density, pressure, and medium flow into the mixing box ($h_{lev(MB)}$, k_{MB}, ρ_{MB}, P_{MB}, and $Q_{in,med(MB)}$ in Figure 6.13 respectively).
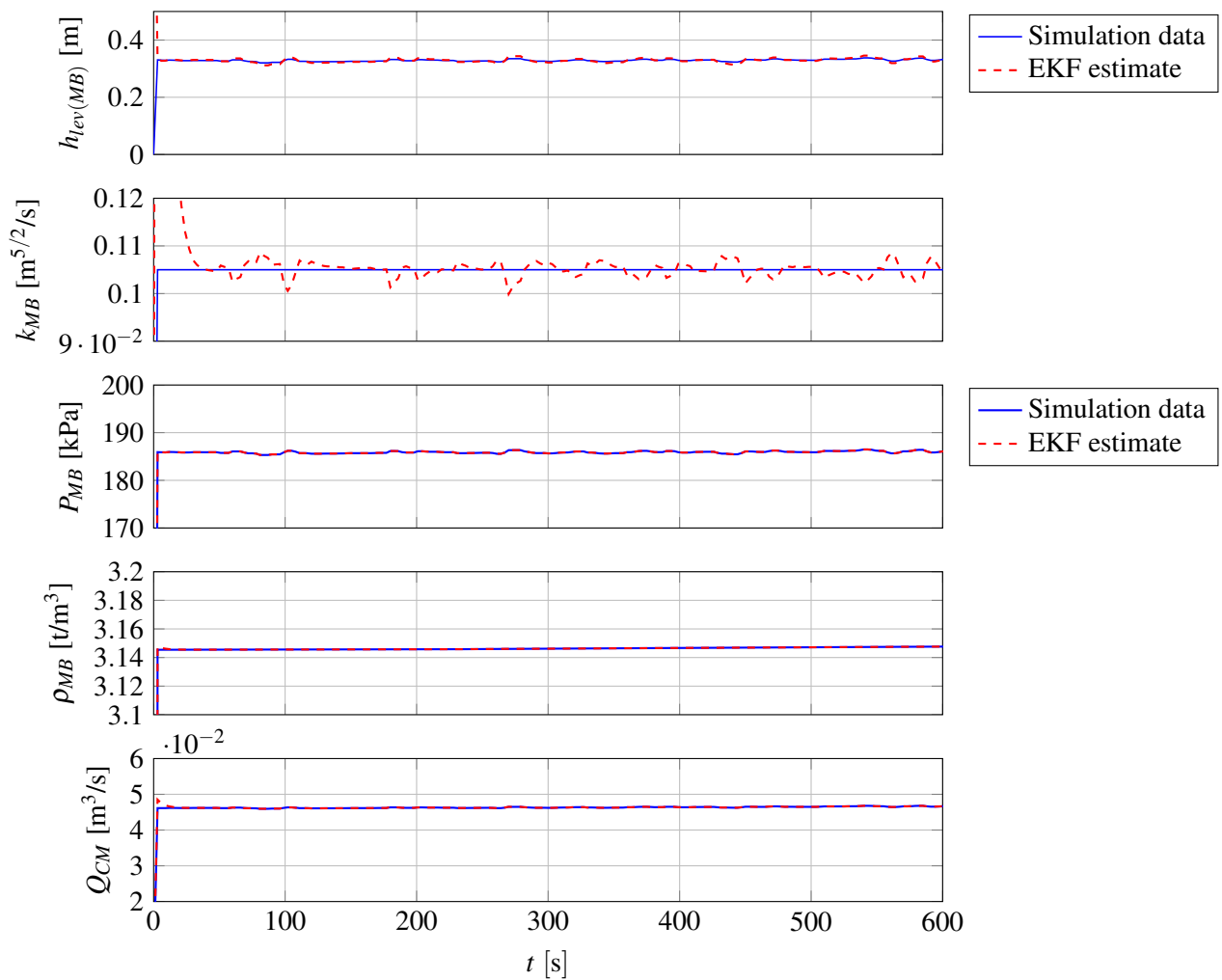
Figure 6.13. Simulation data and EKF estimates of mixing box system states and outputs.

Table 6.7 gives the RMSE and NRMSE for the EKF predictions of the simulated outputs and states.

Table 6.7. RMSE and NRMSE values for mixing box EKF on simulation data.

Variable	RMSE	NRMSE
$h_{lev(MB)}$	0.0132 m	0.0016
k_{MB}	0.00055	0.0157
P_{MB}	0.2573 kPa	0.0011
ρ_{MB}	0.0012 t/m^3	9.0704 $\times 10^{-6}$
Q_{CM}	1.69 $\times 10^{-4}$ m^3/s	0.0031

6.6.2   EKF implementation on mixing box plant data

The EKF algorithm was then applied to the mixing box system, using plant data. The inputs to the
system are shown in Figure 6.14. Note that the correct medium pump flow rate (at top in Figure 6.14)
is not a measured input, but is rather the EKF estimate of the correct medium pump flow rate from the
correct medium tank EKF implementation (see Section 6.2).
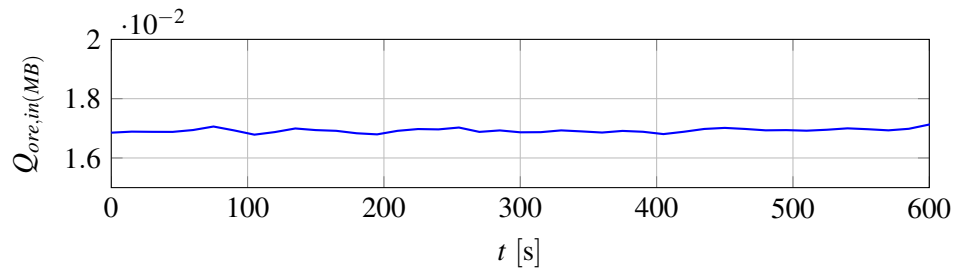
Figure 6.14. Plant data of input to mixing box system.

The results of the EKF implementation on the mixing box system states and outputs are shown in
Figures 6.15. In Figure 6.15, as the flow rate of medium into the mixing box (Q_{CM}, in Figure 6.15)
increases, so does the mixing box level, until the flow out of the mixing box increases to match the
flow in (see (3.22)). The value of k_{MB} stays relatively constant during this time, as expected. Note that
the mixing box discharge pressure (P_{MB} in Figure 6.15) EKF estimate (red) tracks the plant data (blue)
effectively. Table 6.8 gives the RMSE and NRMSE for the EKF predictions of the plant outputs.
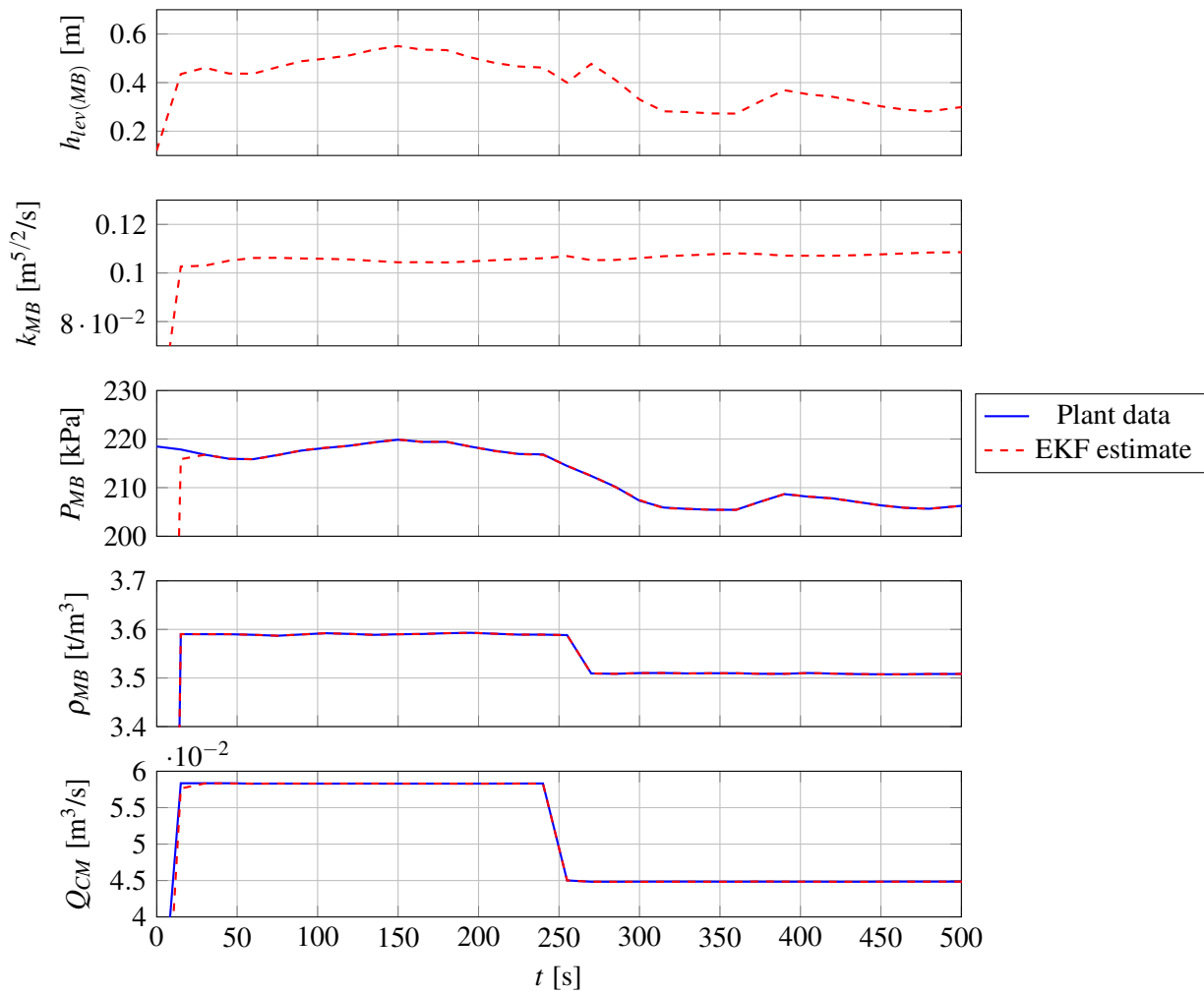
Figure 6.15. Plant data and EKF estimates of mixing box system states and outputs.

Table 6.8. RMSE and NRMSE values for mixing box EKF on plant data.

Variable	RMSE	NRMSE
P_{MB}	0.5979 kPa	0.0028
ρ_{MB}	0.0018 t/m^3	5.0704 $\times 10^{-5}$
Q_{CM}	1.75 $\times 10^{-4}$ m^3/s	0.0034

6.7   CHAPTER SUMMARY

In this chapter, the EKF was applied to the correct medium tank, the secondary tank, the dilute medium tank, and the mixing box. The EKF was applied to both simulation data, as well as to plant data. The EKF was able to adequately estimate the observable but unmeasured states of the observable units (the

correct medium tank, secondary tank, and the mixing box), and also yielded adequate estimates of these system outputs. It is noted, however, that the estimates of the flow into the correct medium tank and secondary tank contain significant noise compared to estimates of other states and outputs. For the dilute medium tank system, the EKF only produced accurate results if the filter was initialised close to the system initial values. This was as expected, as the dilute medium tank system is not fully observable.

CHAPTER 7   STATE ESTIMATION OF MEDIUM LOSSES

7.1   CHAPTER OVERVIEW

In this chapter, the points in the circuit where medium losses can occur are identified: at the mixing box due to overflows caused by blockages, at the product and waste drain-and-rinse screens, and at the magnetic separator effluent. First, the sources of medium losses are discussed in Section 7.2. Each source of loss is then simulated in Sections 7.3, 7.4, and 7.5 respectively, by altering a key parameter in the simulation, and the state estimation developed in Chapter 6 is then applied to the simulation data. For the mixing box blockage scenario, plant data is available, and so state estimation is applied to this plant data as well.

7.2   SOURCES OF MEDIUM LOSS

There are several sources of medium loss in the DMS circuit. Medium can be lost through adhesion to the ore at the drain-and-rinse screens, in the effluent of the magnetic separators (Dardis, 1989; Napier-Munn et al., 1995) as well as through mixing box overflows, or through screen blinding of the drain-and-rinse screens, which results in medium running over the screens to the floor, rather than draining through the screens. These losses can be grouped into three categories (as shown in Figure 7.1): mixing box losses (overflows of the mixing box - in green in the figure), screen losses (adhesion losses and screen blinding losses - in blue in the figure), and magnetic separator losses (losses to the magnetic separator effluent - in yellow in the figure).
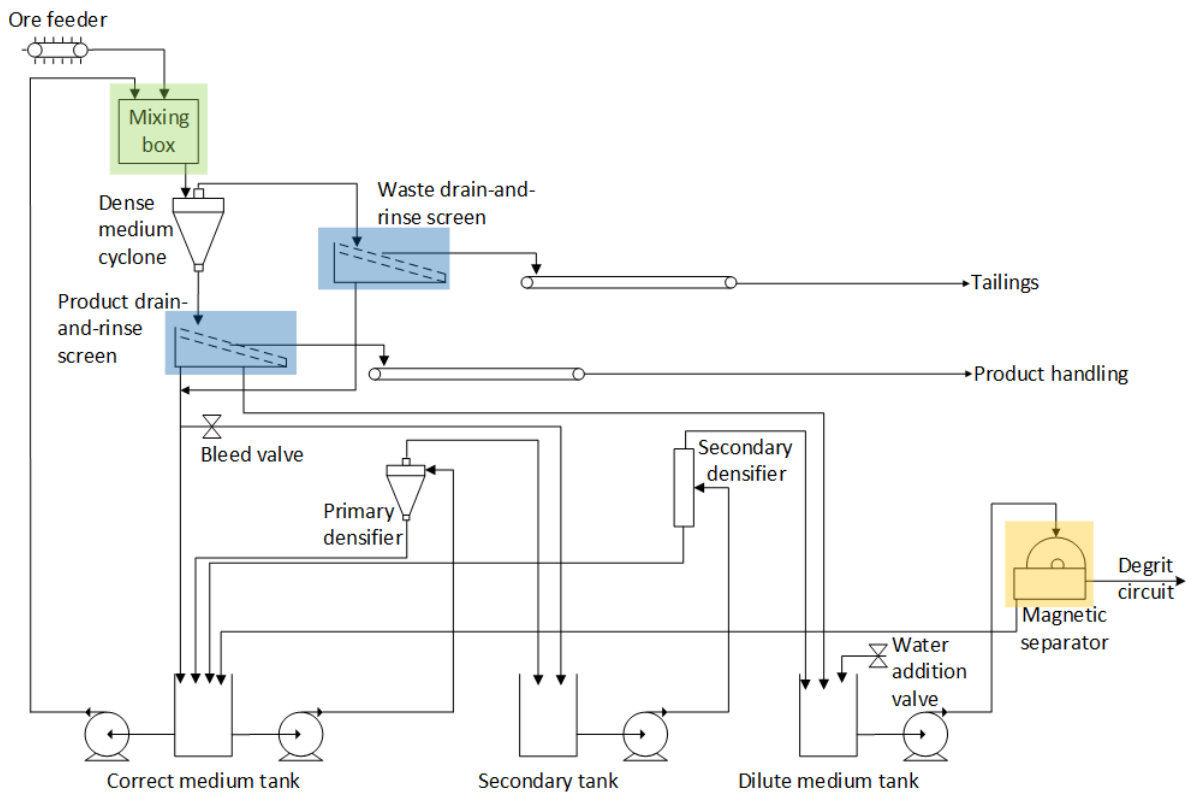
Figure 7.1. Diagram of DMS circuit. Green highlight indicates mixing box overflow medium losses, blue indicates screen losses, and yellow indicates magnetic separator losses.

The model of the DMS circuit developed in this work can be used to simulate these losses to illustrate the impact on the overall circuit. In this chapter, each of these sources of loss is simulated, and a state estimation of these scenarios is performed. Later analysis in Chapter 8, will discuss the effectiveness of this state estimation in detecting the three sources of loss.

7.3   MIXING BOX BLOCKAGES

Mixing box level overflows are experienced fairly frequently by production teams. Due to the difficulty of getting accurate level measurement of the mixing box (the environment is very abrasive due to the presence of the medium), mixing box overflows are often only detected visually. This can mean that the mixing box can be overflowing for a period of time before it is seen by plant personnel.

7.3.1   Mixing box blockage simulation

Mixing box overflows can be caused by either the flow of material into the mixing box being too high (that is, the feed of ore or the correct medium pump flow rate is too high), or due to a blockage in the

mixing box.

Blockages are akin to the geometry of the outlet of the mixing box changing (and reducing in size). Thus a blockage can be simulated by reducing the value of the mixing box outlet coefficient, k_{MB}, in (3.25). This was simulated in the Simulink model, with the k_{MB} value changing from 0.105 to 0.04 at time $t = 230$ s. The results of the simulation are shown below for the mixing box and the correct medium tank. Because the effect on the secondary tank is minimal, for brevity it has not been included.

Figure 7.2 shows the disturbance to k_{MB} introduced to the simulation.
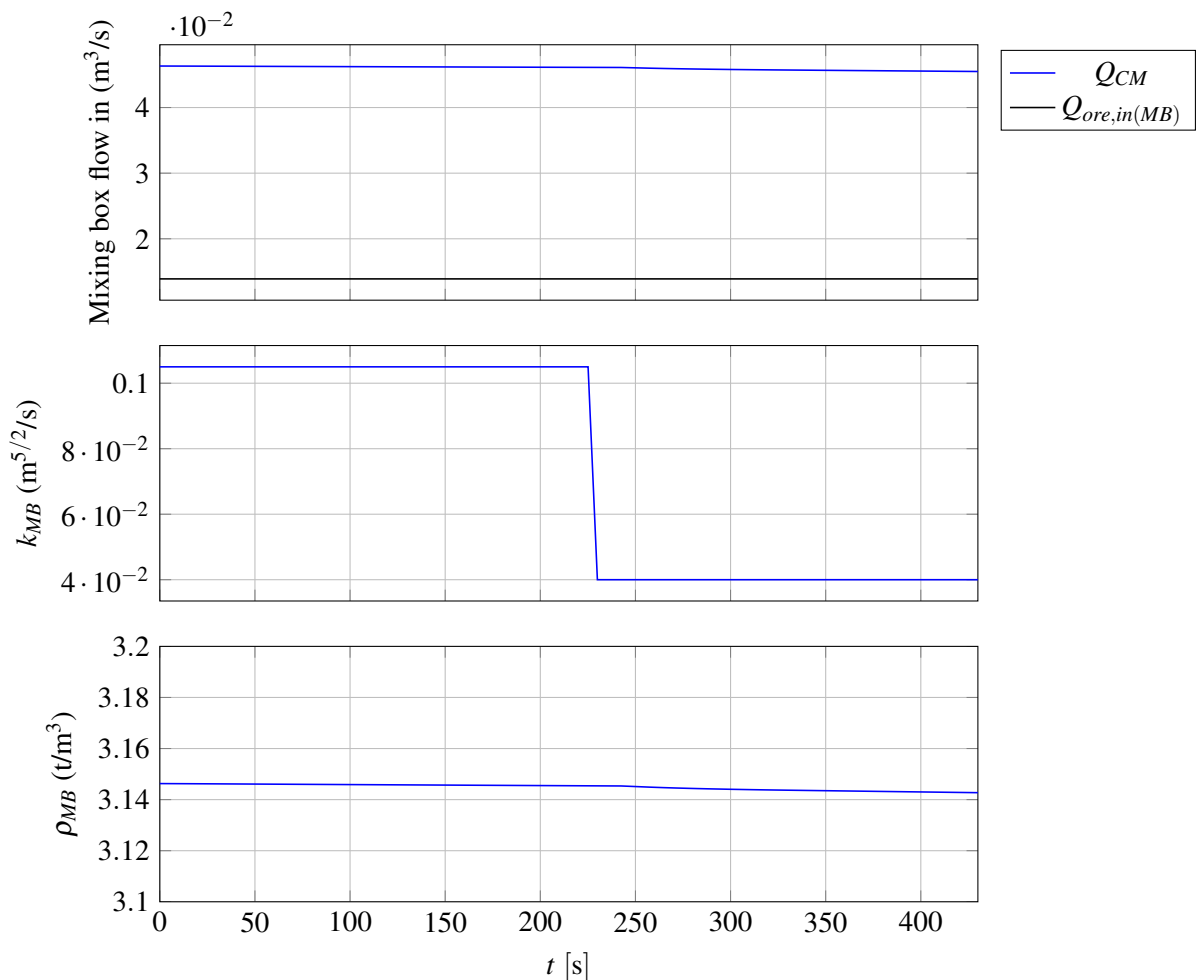
Figure 7.2. Inputs and uncontrolled disturbances to mixing box system for mixing box blockage simulation.

The effect of the decrease in k_{MB} on the mixing box can be seen in Figure 7.3: there is an immediate reduction in the flow of medium and ore out of the mixing box ($Q_{med,out(MB)}$ and $Q_{ore,out(MB)}$ respectively), which has the effect of increasing the mixing box level ($h_{lev(MB)}$).
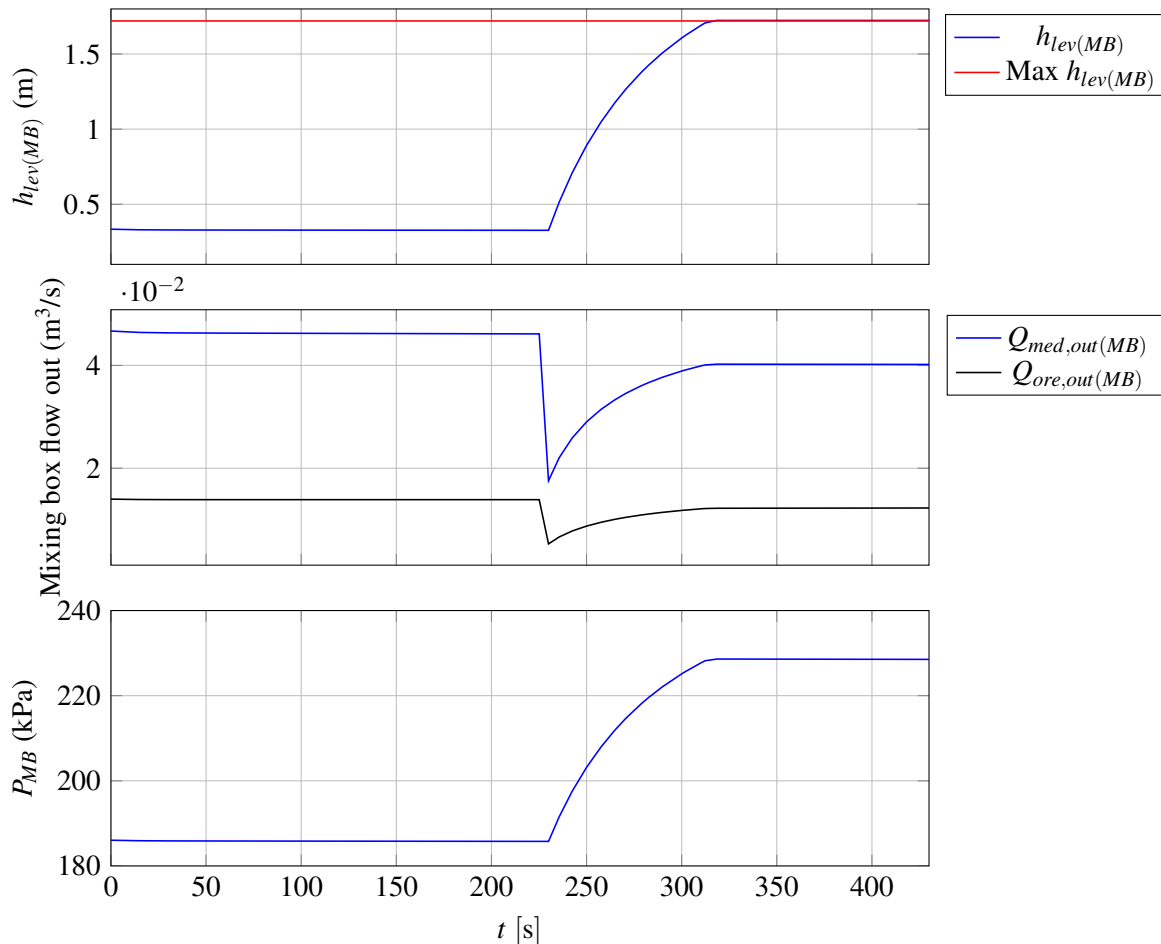
Figure 7.3. States, outputs, and flow rates out of mixing box system for mixing box blockage simulation.

Note that at $t = 230$ s, when k_{MB} is decreased, $h_{lev(MB)}$ increases rapidly until it reaches the maximum height of 1.72 m (indicated in red in Figure 7.3), where it remains. The simulation is set up such that the level is not able to exceed the maximum mixing box height, as at this point the mixing box is overflowing. This means that the flow of slurry out of the mixing box ($Q_{med,out(MB)}$, at middle in Figure 7.3) is not able to recover to the same outflow before the disturbance in k_{MB}. The same applies to the discharge pressure. The level, therefore, does not stabilise, and continues to overflow.

The reduction in $Q_{med,out(MB)}$ seen in Figure 7.3 (at middle, in blue) results in a decrease in the flow of slurry to the correct medium tank. This effect is seen in Figure 7.4.
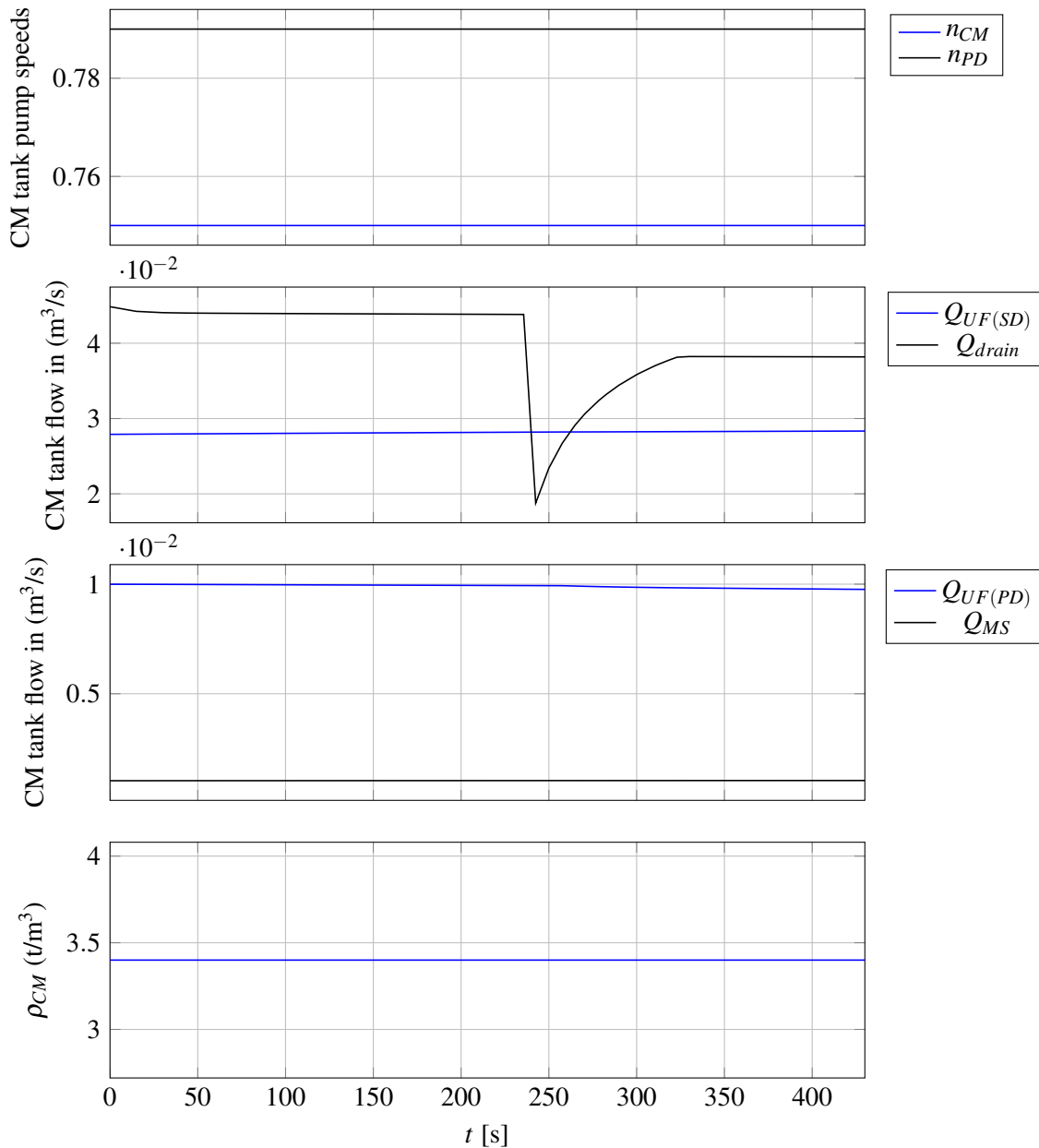
Figure 7.4. Inputs and uncontrolled disturbances to correct medium tank system for mixing box blockage simulation.

At $t = 290$ s, after the transport delay following the disturbance to the mixing box outlet coefficient (k_{MB}), the flow into the correct medium tank from the drain-and-rinse screens (Q_{drain} in Figure 7.4) reduces. This is as expected because reducing k_{MB} has the effect of decreasing the flow out of the

mixing box (see Figure 7.3 at middle), and therefore reducing the flow into the correct medium tank from the drain-and-rinse screens. This reduced flow into the tank has the effect of reducing the correct medium tank level $h_{lev(CM)}$, which can be seen in Figure 7.5. The decrease in the correct medium tank level $h_{lev(CM)}$ results in a small decrease in the correct medium and primary densifier pump flow rates (Q_{CM} and Q_{PD} in Figure 7.5 respectively). This is due to the decrease in static head (as a result of the decreased tank level).
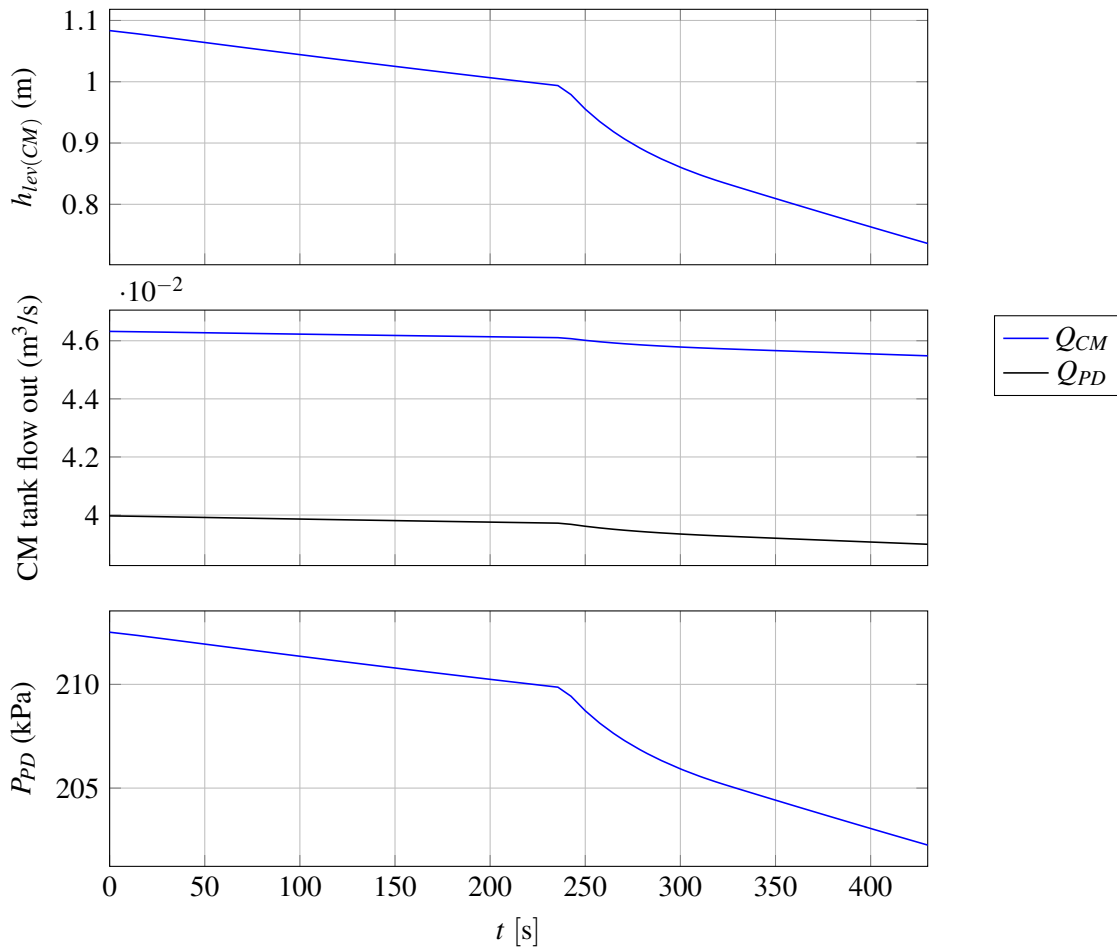
Figure 7.5. States and outputs of correct medium tank system for mixing box blockage simulation.

7.3.2   Mixing box blockage simulation state estimation

The mixing box overflows can be seen in the level of the mixing box exceeding the maximum. While the level of the mixing box is not instrumented, the observability analysis in Section 5 shows that the level and the outlet coefficient k_{MB} are both observable. Therefore, the EKF developed in Section 6.6.1 for state estimation of the observable but unmeasured states in the mixing box is applied to the mixing box blockage scenario simulated in Section 7.3.1. Before applying the EKF to the mixing box system,

however, state estimation of the correct medium tank (including of the correct medium pump flow rate, which flows into the mixing box - see Figure 1.1) is first required, because the flow of medium into the mixing box is not measured. The EKF estimation results for the correct medium tank system during the simulated mixing box blockage are shown in Figure 7.6.
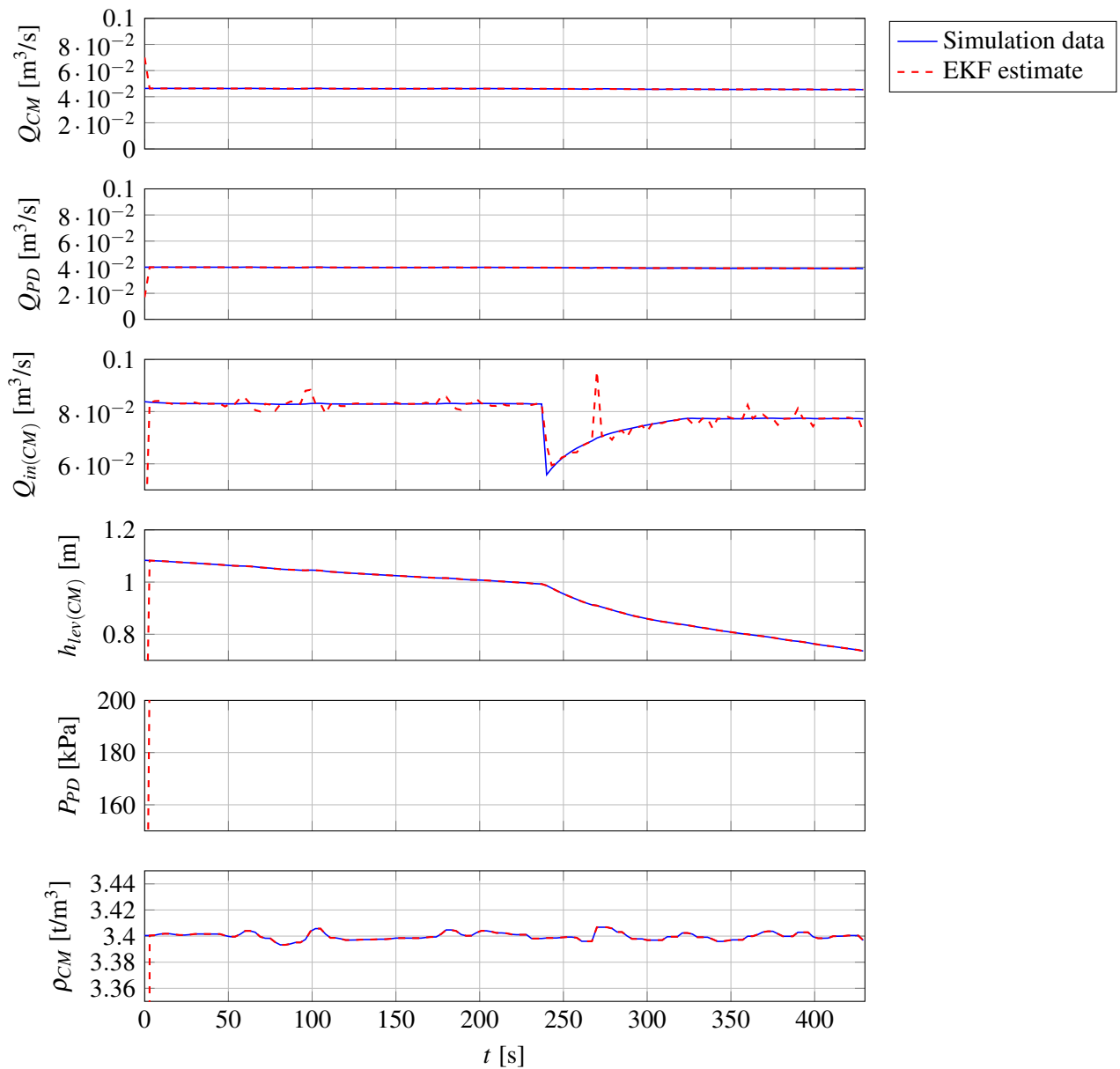
Figure 7.6. Simulation data and EKF estimates of correct medium tank system and states during simulated mixing box blockage.

Following the EKF estimation of the correct medium tank system, the EKF is then applied to the mixing box system. The input to this system is shown in Figure 7.11.
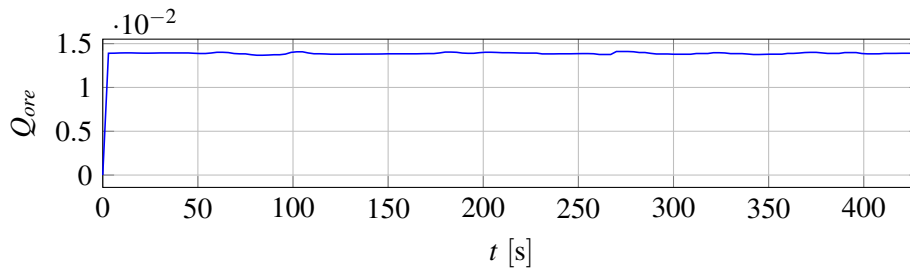
Figure 7.7. Simulation data of input to mixing box system during simulated mixing box blockage.

The results of the EKF implementation on the mixing box system states and outputs are shown in Figure 6.13.
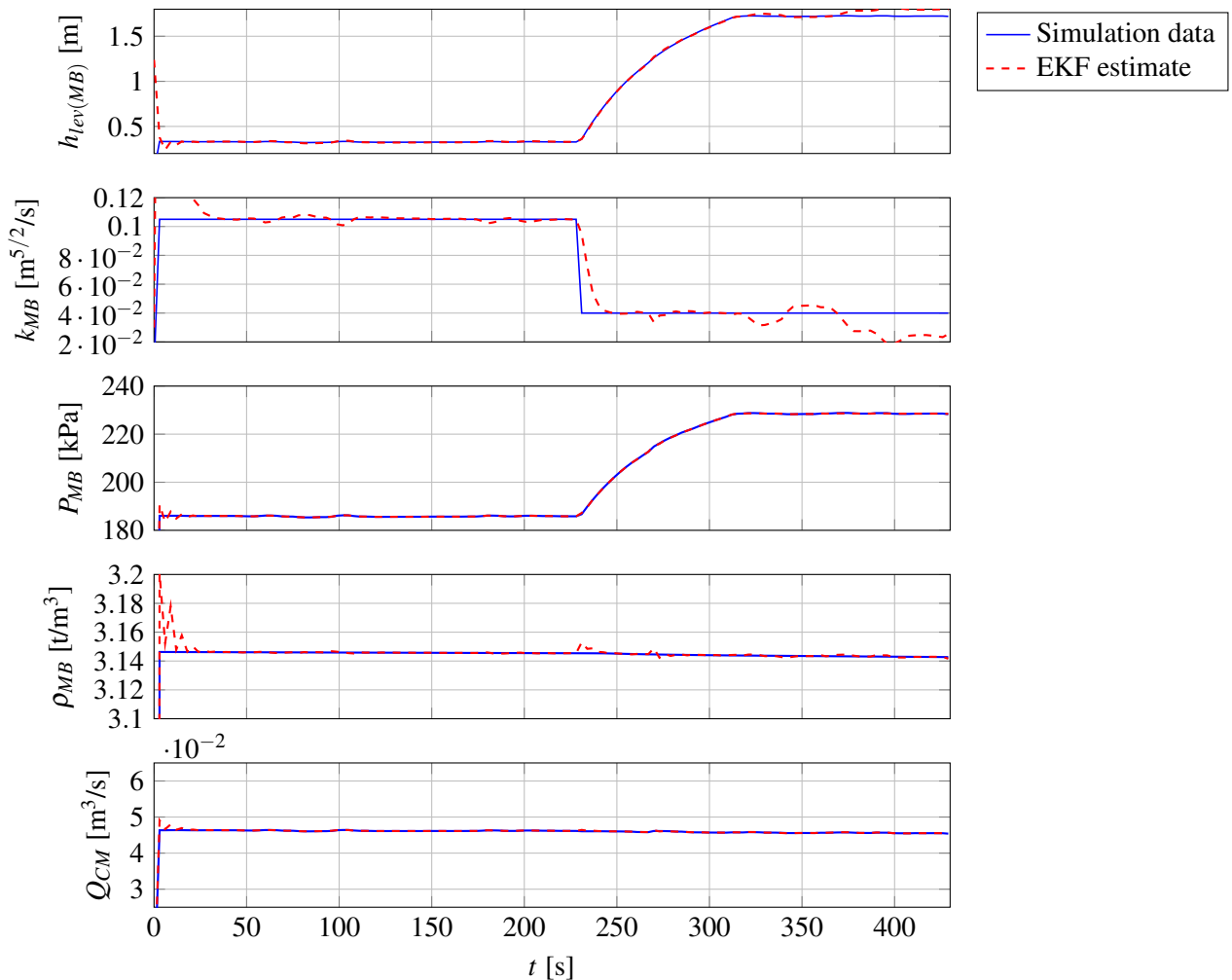
Figure 7.8. Simulation data and EKF estimates of mixing box system states and outputs during simulated mixing box blockage.

The EKF estimate (red) tracks the simulation (blue) effectively, for the mixing box level, discharge pressure, density, and flow into the mixing box ($h_{lev(MB)}$, P_{MB}, ρ_{MB}, and $Q_{med,in(MB)}$ in Figure 7.8 respectively). It should be noted that the EKF estimate of k_{MB} is fairly stable before the blockage is simulated by decreasing k_{MB} at $t = 230$ s. However, after the step decrease in k_{MB}, the EKF estimate of k_{MB} is quite noisy. This is because, in the simulation and the EKF, $h_{lev(MB)}$ is limited to its maximum level of 1.72m. This means that any noise present in the simulated P_{MB} once $h_{lev(MB)}$ is at its maximum is attributed to the estimate of k_{MB}, hence the increased noise in the k_{MB} EKF estimate after $t = 230$ s in Figure 7.8.

7.3.3   Mixing box blockage in plant data

State estimation (as developed in Chapter 6) was then applied to plant data for a period when a blockage in the mixing box was reported. Note that because the flow of medium into the mixing box is not measured, state estimation of the correct medium tank (including of the correct medium pump flow rate, which flows into the mixing box - see Figure 1.1) is first required. The inputs to the correct medium tank system during the plant mixing box blockage are shown in Figure 7.9.
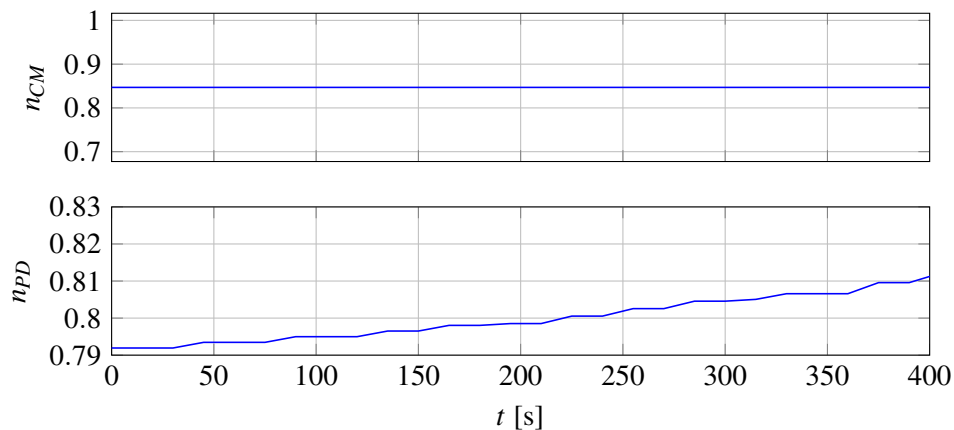
Figure 7.9. Plant data of inputs to correct medium tank system during plant mixing box blockage.

The EKF state estimation of the correct medium tank system states during the plant mixing box blockage are shown in Figure 7.10.
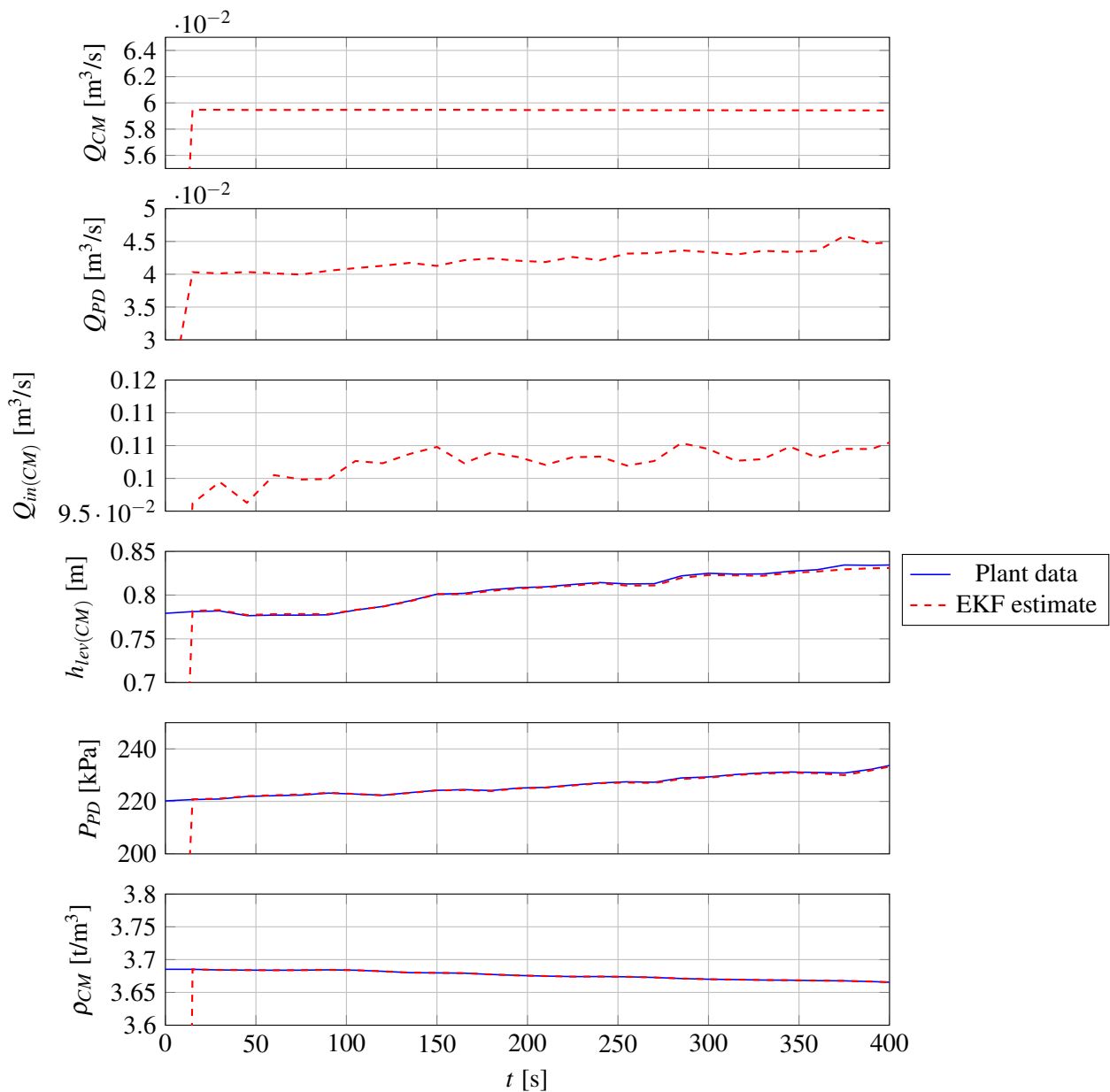
Figure 7.10. Plant data and EKF estimates of correct medium tank system states and outputs during mixing box blockage.

The EKF for the mixing box was then applied to the plant mixing box blockage data. Figure 7.11 shows the plant data of the input to the mixing box system during this period ($Q_{ore,in(MB)}$).
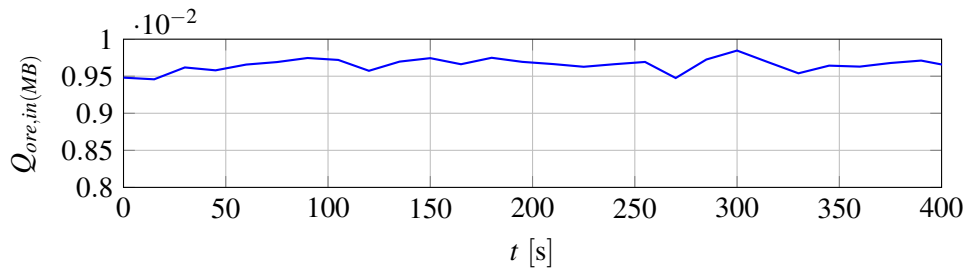
Figure 7.11. Plant data of input to mixing box system during mixing box blockage.

Figure 7.12 shows the EKF estimation results for the states and outputs of the mixing box augmented system during the plant mixing box blockage: the mixing box level ($h_{lev(MB)}$), outlet coefficient (k_{MB}), the mixing box discharge pressure (P_{MB}), the mixing box density (ρ_{MB}), and the flow of medium into the mixing box (Q_{CM}). The plant data for Q_{CM} (in Figure 7.12) is obtained from the EKF estimate of the correct medium pump discharge flow rate (obtained as part of the EKF application to the correct medium tank system - see Figure 7.10), while the plant data for ρ_{MB} is calculated using Q_{CM}, $Q_{ore,in(MB)}$, ρ_{CM}, and ρ_{ore} according to (3.24).
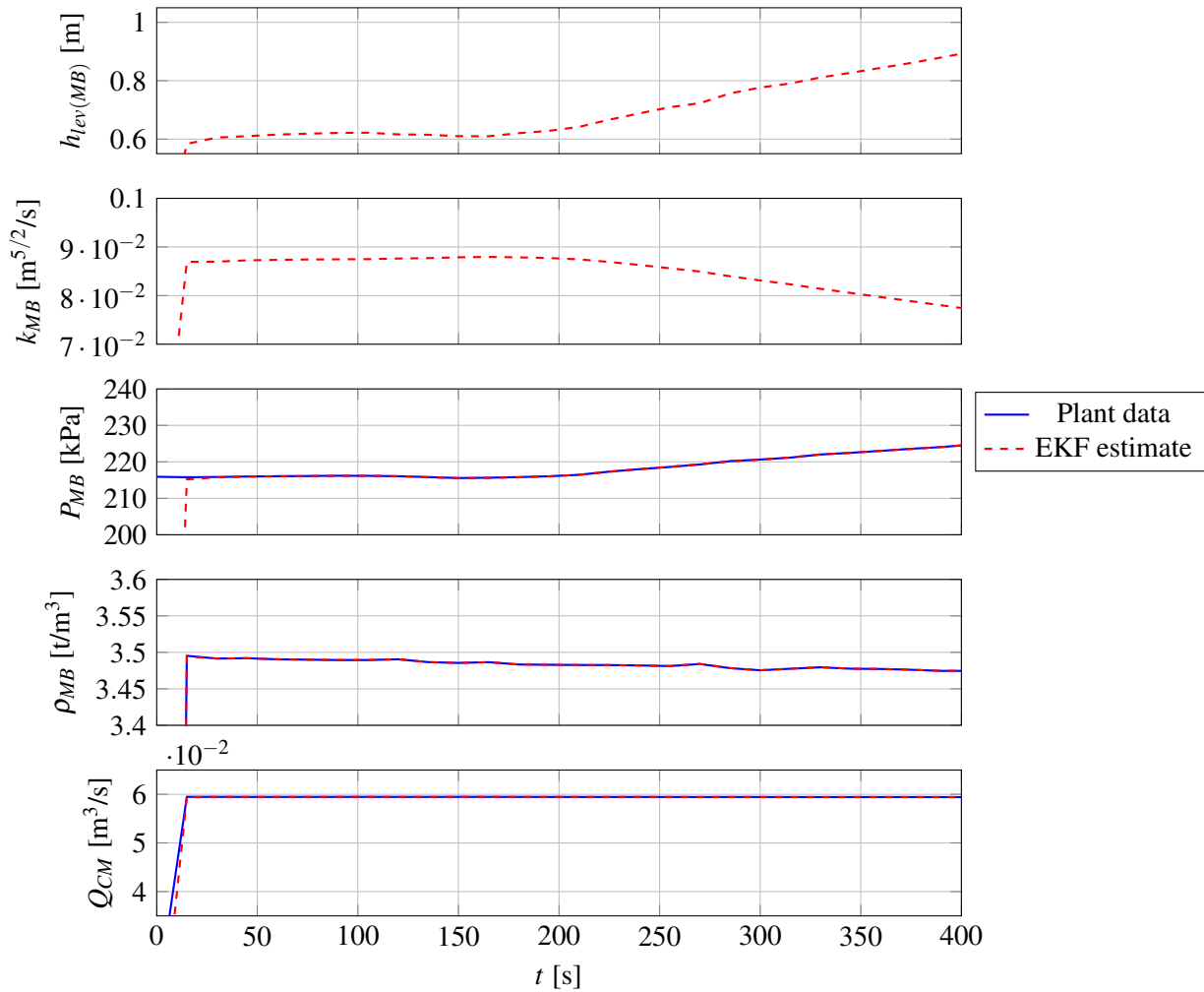
Figure 7.12. Plant data and EKF estimates of mixing box states and outputs during mixing box blockage.

In Figure 7.12, from $t = 200$ s, the outlet pressure, P_{MB}, slowly increases, despite there being no increase in Q_{CM} (see Figure 6.4) or $Q_{ore,in(MB)}$ (see Figure 7.11). This indicates a blockage, which is reflected in the state estimation of the mixing box level, $h_{lev(MB)}$ (see Figure 7.12), and in the estimation of the outlet coefficient, k_{MB} (in Figure 7.12). The level increases steadily, while the outlet coefficient k_{MB} decreases steadily, indicating a blockage. It is clear that no overflow occurred, as $h_{lev(MB)}$ remains below the maximum level of 1.72m. It would be expected that, due to the blockage, the EKF state estimate of $Q_{in(CM)}$ seen in Figure 6.4 would show a decrease, as the reason the mixing box level is increasing is because less material is flowing out of the mixing box and consequently to the correct medium tank. However, this decrease is not apparent. This is because the reduction in flow out of

the mixing box (and therefore in $Q_{in(CM)}$) is small in magnitude, and therefore not clear in the state estimation of $Q_{in(CM)}$ which contains some noise.

Despite not seeing the decrease in $Q_{in(CM)}$, the EKF estimate results, which show a clear decrease in k_{MB} during the mixing box blockage (see Figure 7.12), are significant as they demonstrate that a blockage in the mixing box, which could lead to an overflow and subsequent medium loss, can be detected.

7.4 SCREEN LOSSES

Medium losses at the product and waste drain-and-rinse screens (see Figure 7.1, highlighted in blue) can be due to adhesion of the medium to the porous ore (Dardis, 1989; Napier-Munn et al., 1995), or due to screen blinding where the medium does not drain through the screen but rather runs over the screen. In this work, these two causes of medium loss at the drain-and-rinse screens are grouped together, as both have the same effect on the systems within the circuit.

7.4.1 Screen losses simulation

Screen losses can be simulated by assuming the value of k_{DMC} in (3.27) to be less than 1. This will result in the simulated flow of medium out of the dense medium cyclone and screens system to be less than that flowing into the system, thus indicating medium has been lost. This scenario is simulated, with k_{DMC} being decreased from 1 to 0.95 at $t = 230$ s. As this would only have an effect on the correct medium and secondary tank systems, and the effect on the dilute medium tank would be minimal, only the correct medium and secondary tanks simulation results are shown. Figure 7.13 shows the inputs to the correct medium tank system during the screen losses simulation.
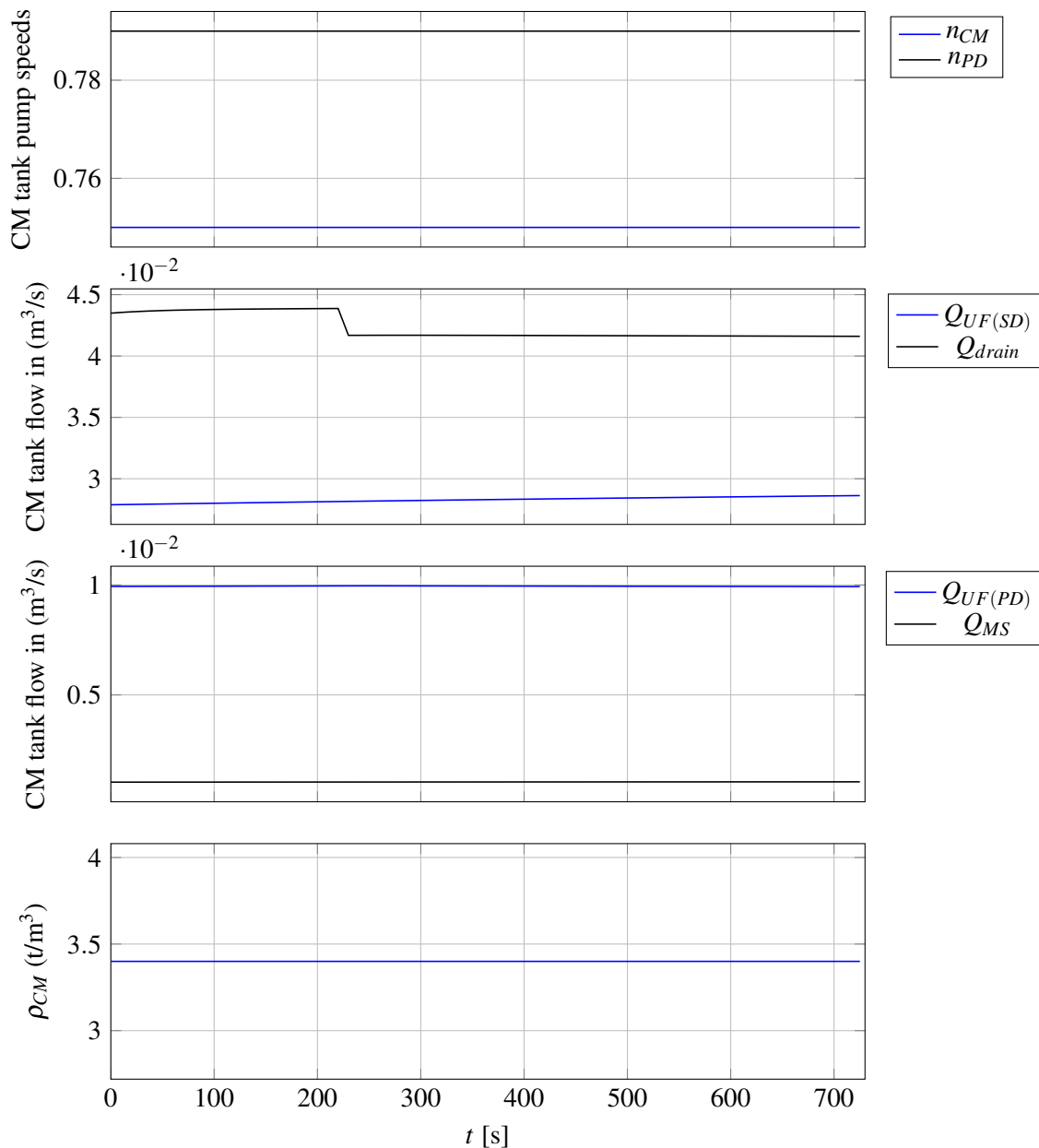
Figure 7.13. Inputs and uncontrolled disturbances to correct medium tank system during screen losses simulation.

Note that at $t = 240$ s, after the transport delay when the disturbance to the screens is introduced, the flow into the correct medium tank from the drain-and-rinse screens (Q_{drain} in Figure 7.13) reduces. This is as expected because decreasing k_{DMC} in (3.27) has the effect of decreasing the flow of medium from the drain-and-rinse screens, and therefore reducing the flow into the correct medium tank. This reduced flow into the tank has the effect of reducing the level, which can be seen in Figure 7.14.
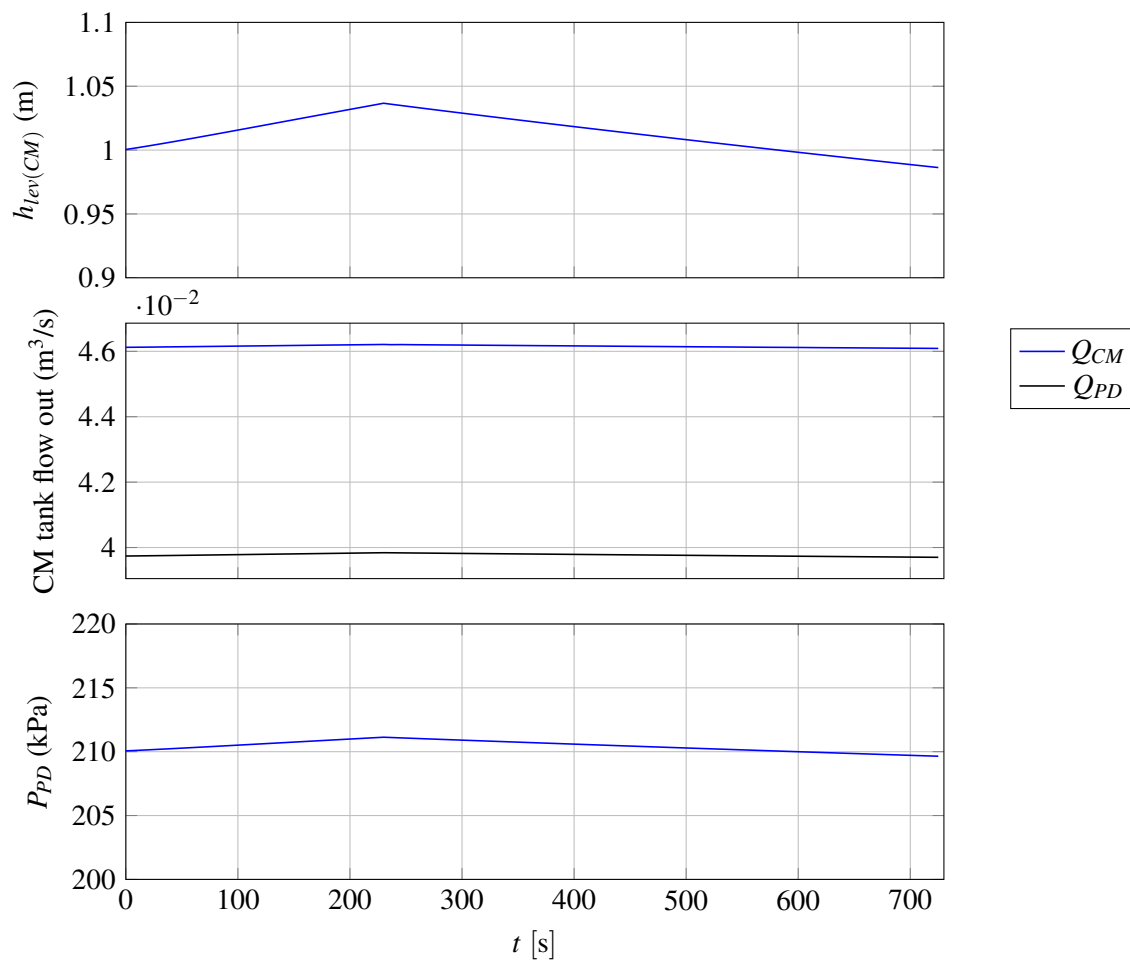
Figure 7.14. States and outputs of correct medium tank Simulink model during screen losses simulation.

Although the bulk of the medium that drains from the drain-and-rinse screens reports to the correct medium tank, there is a small bleed stream that reports to the secondary tank (Q_{bleed}). Medium losses at the drain-and-rinse screens therefore also have an effect on the secondary tank system, seen in Figures 7.15 and 7.16.
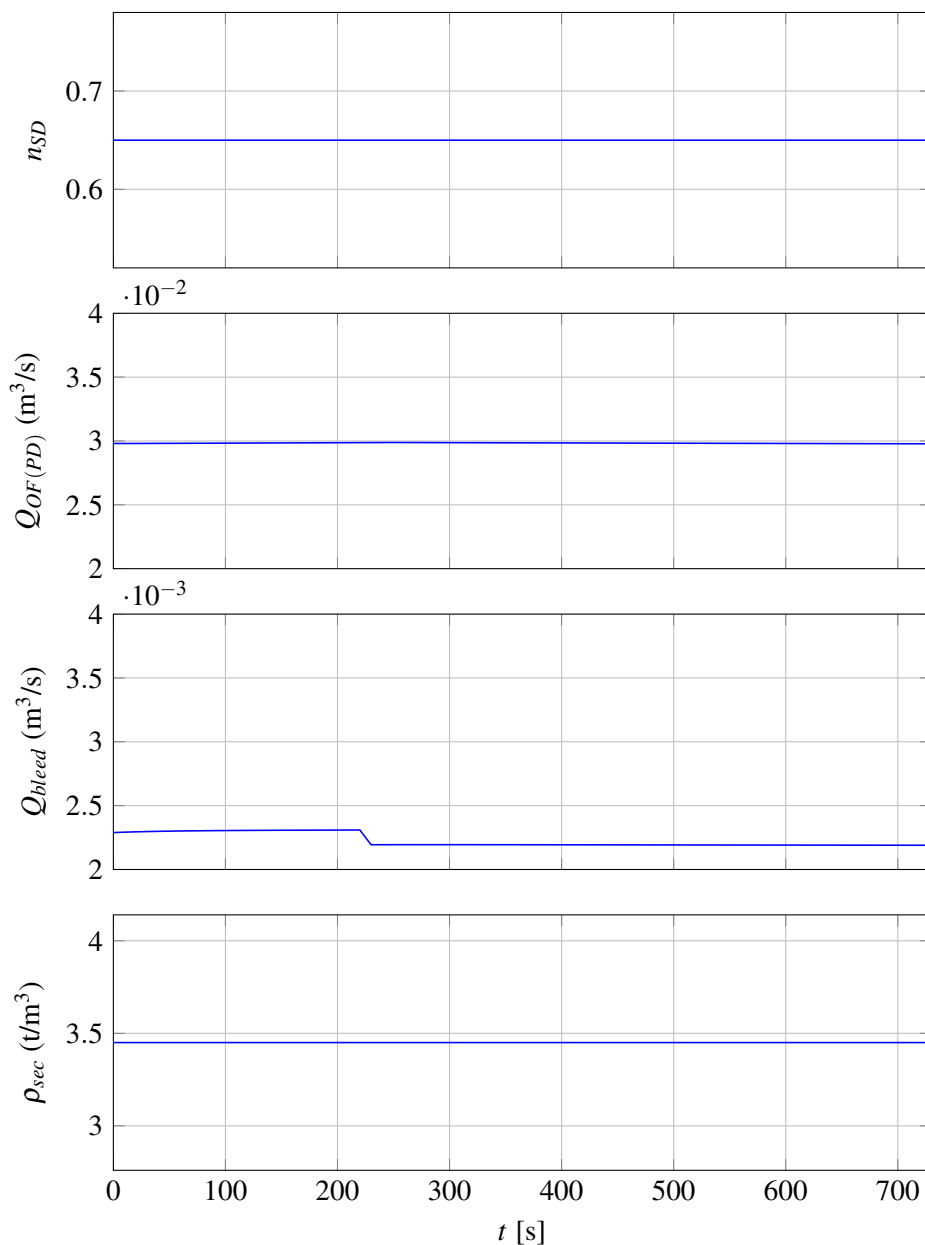
Figure 7.15. Inputs and uncontrolled disturbances to secondary tank system during screen losses simulation.

Note that the bleed stream flow of medium from the drain-and-rinse screens to the secondary tank (Q_{bleed} in Figure 7.15), while already small in comparison to the flow into the tank from the overflow of the primary densifier ($Q_{OF(PD)}$ in Figure 7.16), decreases at $t = 240$ s, following the decrease in k_{DMC}. The effect of this on the secondary tank level is seen in Figure 7.16.
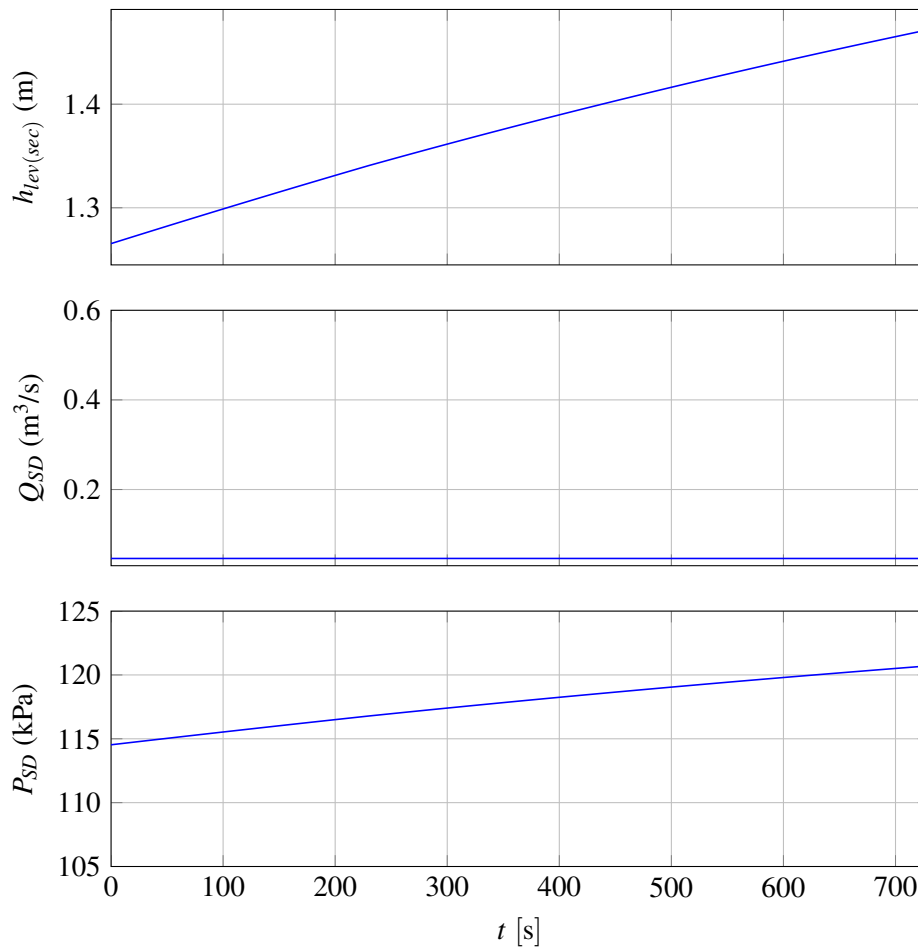
Figure 7.16. States and outputs of secondary tank Simulink model during screen losses simulation.

Note that it is very difficult to visually see a change in the rate of change of the secondary tank level ($h_{lev(sec)}$, at top in Figure 7.16), which is expected to be seen at $t = 240$ s. This concurs with the theory, as the change in the flow rate of medium into the secondary tank (see Figure 7.15) is small in magnitude compared to the total flow of medium into the tank.

7.4.2 Screen losses simulation state estimation

The dense medium cyclone and drain-and-rinse screens system is very poorly instrumented (with only the feed pressure to the DMC measured online), and therefore it is not observable, and the value of k_{DMC} as well as the flow of medium out of the system cannot be estimated using state estimation methods. The correct medium tank system, however, is fully observable (see Section 5), and the flow of medium into the correct medium tank can be estimated using an EKF (see Section 6.2). This means that if there are excessive losses at the screens (due to absorption or blinding), the reduced flow of

medium to the correct medium tank will be visible in that the EKF estimation of the flow rate into the correct medium tank will decrease. The EKF algorithm is therefore applied to the correct medium tank system, for the simulation scenario described in Section 7.4.1. The EKF estimation results are shown in Figure 7.17.
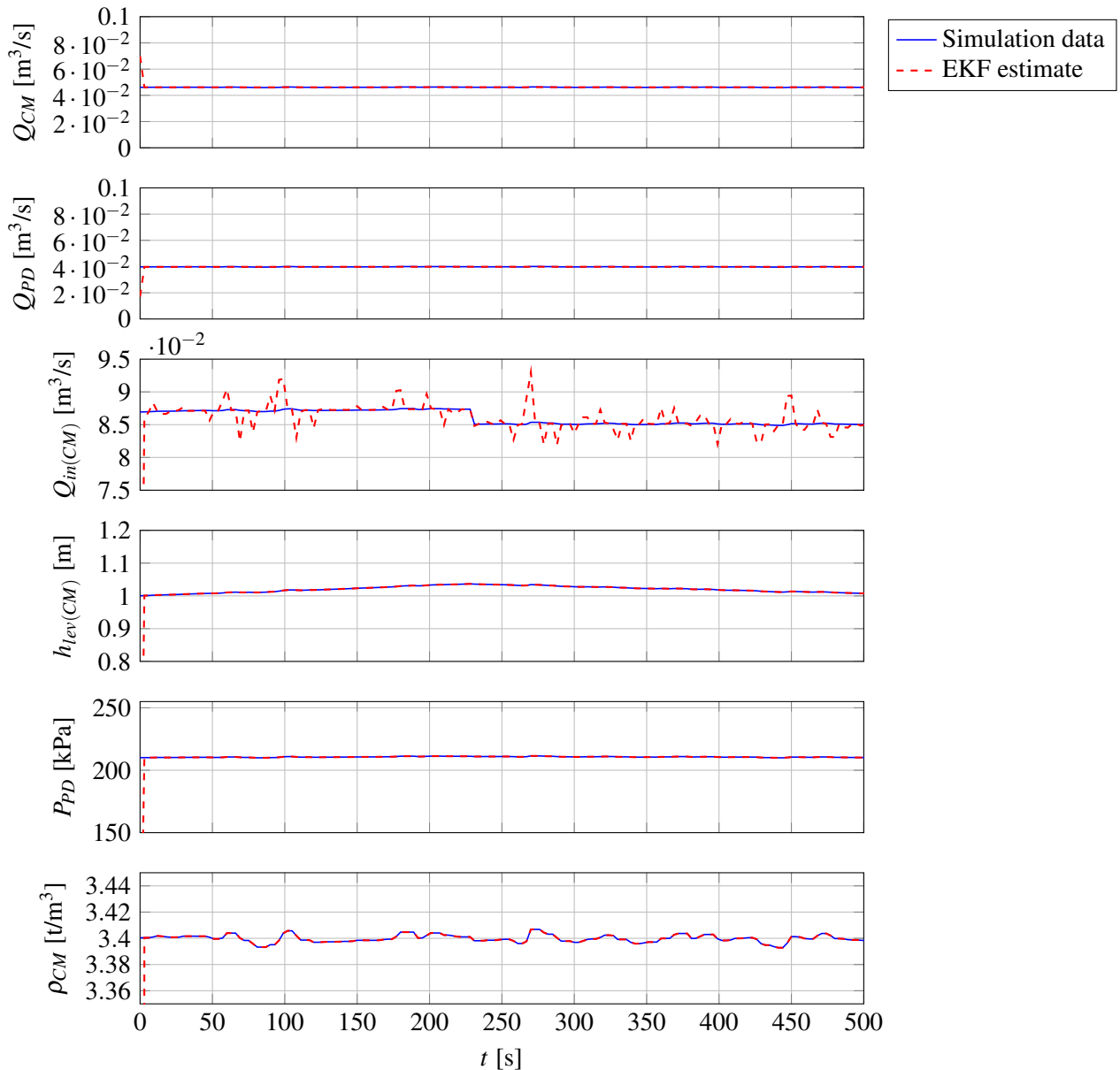

Figure 7.17. Simulation data and EKF estimates of correct medium tank system states and outputs during simulated screen medium loss event.

The estimation of the flow of medium into the correct medium tank, $Q_{in(CM)}$, is seen in Figure 7.17. The simulated $Q_{in(CM)}$ (blue) steps down from 0.086 m^3/s to 0.085 m^3/s. Note that even with the noise

present in the estimate (red) of $Q_{in(CM)}$, the decrease in the estimate of $Q_{in(CM)}$ is still clear.

As there is a small bleed stream from the product and gangue drain-and-rinse screens that reports to the secondary tank, the EKF for the secondary tank system is applied to the screen losses simulation. Figure 7.18 shows the EKF estimation results for the secondary tank system states and outputs.
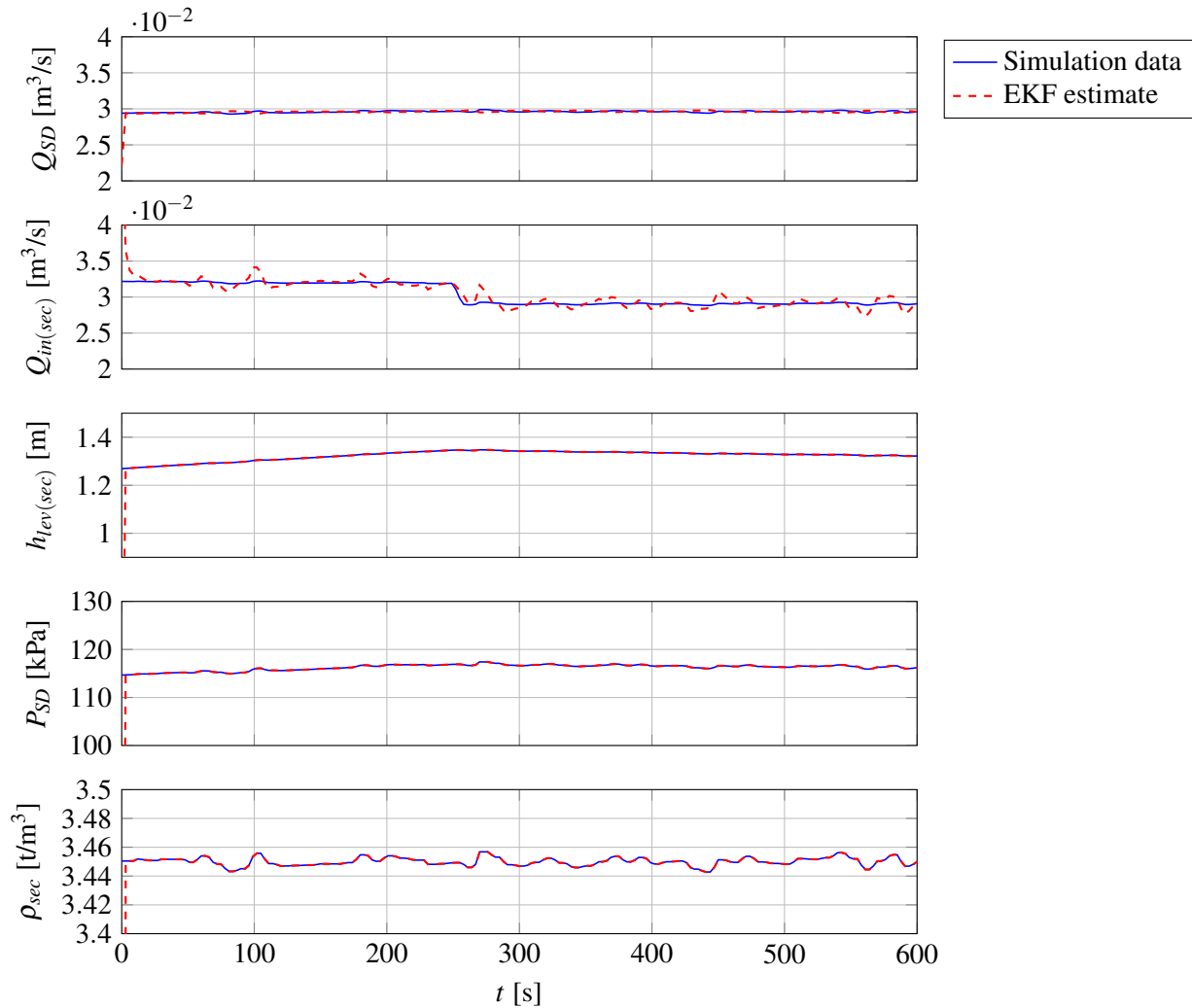

Figure 7.18. Simulation data and EKF estimates of secondary tank system states and outputs during simulated screen loss event.

Note that the reduction in the simulated flow rate of medium into the secondary tank ($Q_{in(sec)}$ in Figure 7.18) is very small in magnitude (as expected, due to the small reduction in Q_{bleed} seen in Figure 7.15). In addition, the state estimation of $Q_{in(sec)}$ (in Figure 7.18) is quite noisy in comparison to the state estimate of Q_{SD} (in Figure 7.18).

7.5   MAGNETIC SEPARATOR EFFLUENT LOSSES

A significant source of medium losses is to the magnetic separator effluent (Dardis, 1989; Napier-Munn et al., 1995). Within a magnetic separator, concentrate medium adheres to the rotating drum, while non-magnetic material passes to the effluent collection pan (Rayner and Napier-Munn, 2003a,b). Medium losses occur when, instead of adhering to the rotating drum, medium is passed into the effluent. An indicator of this is a change in the flow of concentrate from the magnetic separator, while the feed to the magnetic separator remains constant.

7.5.1   Magnetic separator effluent losses simulation

Losses to the magnetic separator can be simulated by decreasing the value of k_{MS} in (3.32). This will result in abnormally low medium flow returning from the magnetic separator to the correct medium tank, thus simulating medium losses to the magnetic separator effluent. This was simulated, with k_{MS} being reduced from 0.0476 to 0.0238 at $t = 230$ s, and the results are show Figures 7.19 and 7.20. As this would only have an effect on the correct medium tank system, only the correct medium tank simulation results are shown.
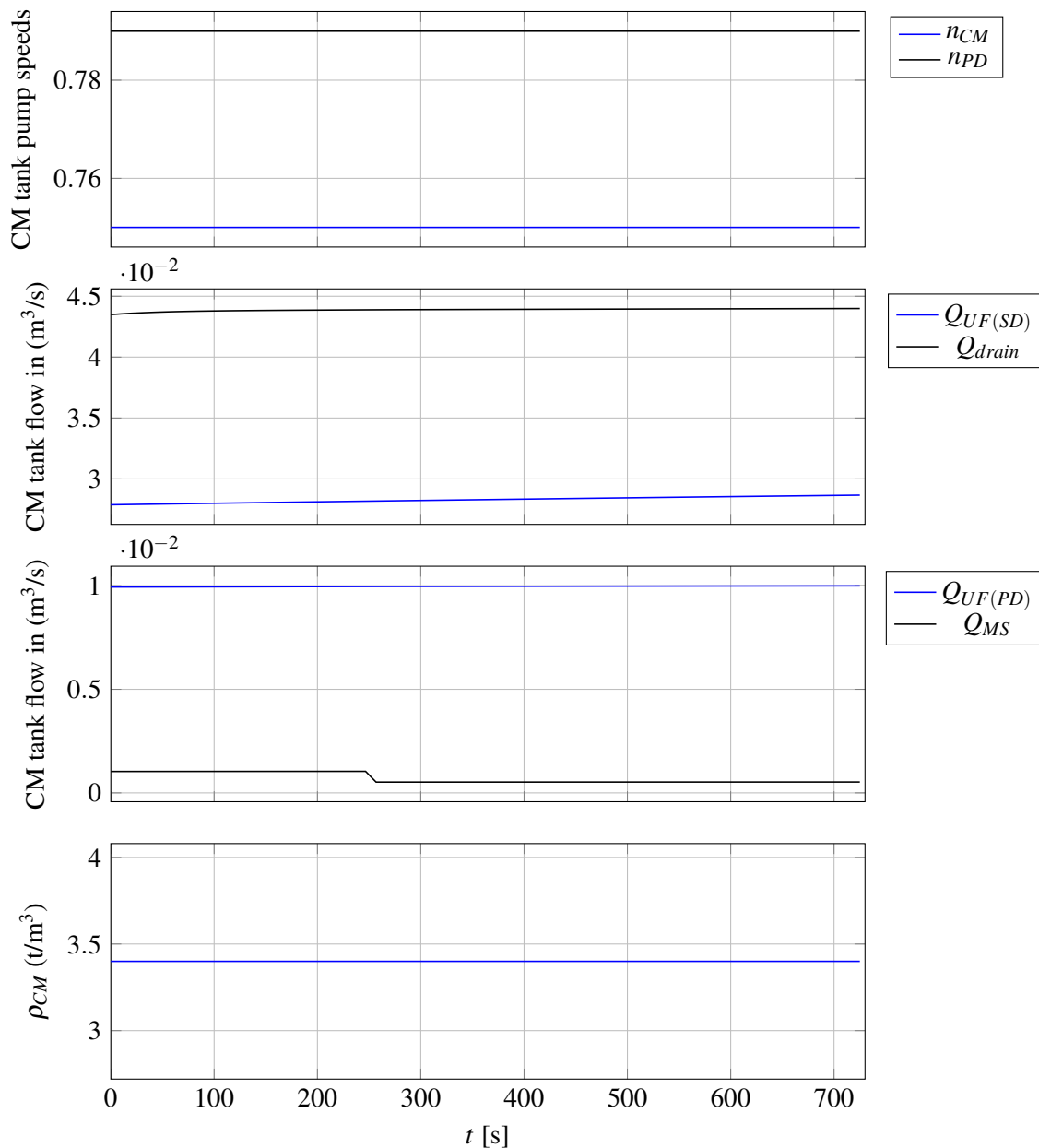
Figure 7.19. Inputs and uncontrolled disturbances to correct medium tank during magnetic separator effluent losses simulation.

Note that at $t = 250$ s, after the transport delay when the disturbance to k_{MS} is introduced, the concentrate flow from the magnetic separators into the correct medium tank (Q_{MS} in Figure 7.19) reduces. Note that this reduction in flow is quite small in magnitude, given that the concentrate flow from the magnetic separator is less than 5% of the flow of feed to the magnetic separator. This reduced

flow into the tank has the effect of reducing the rate of change level, which can be seen in Figure 7.20.
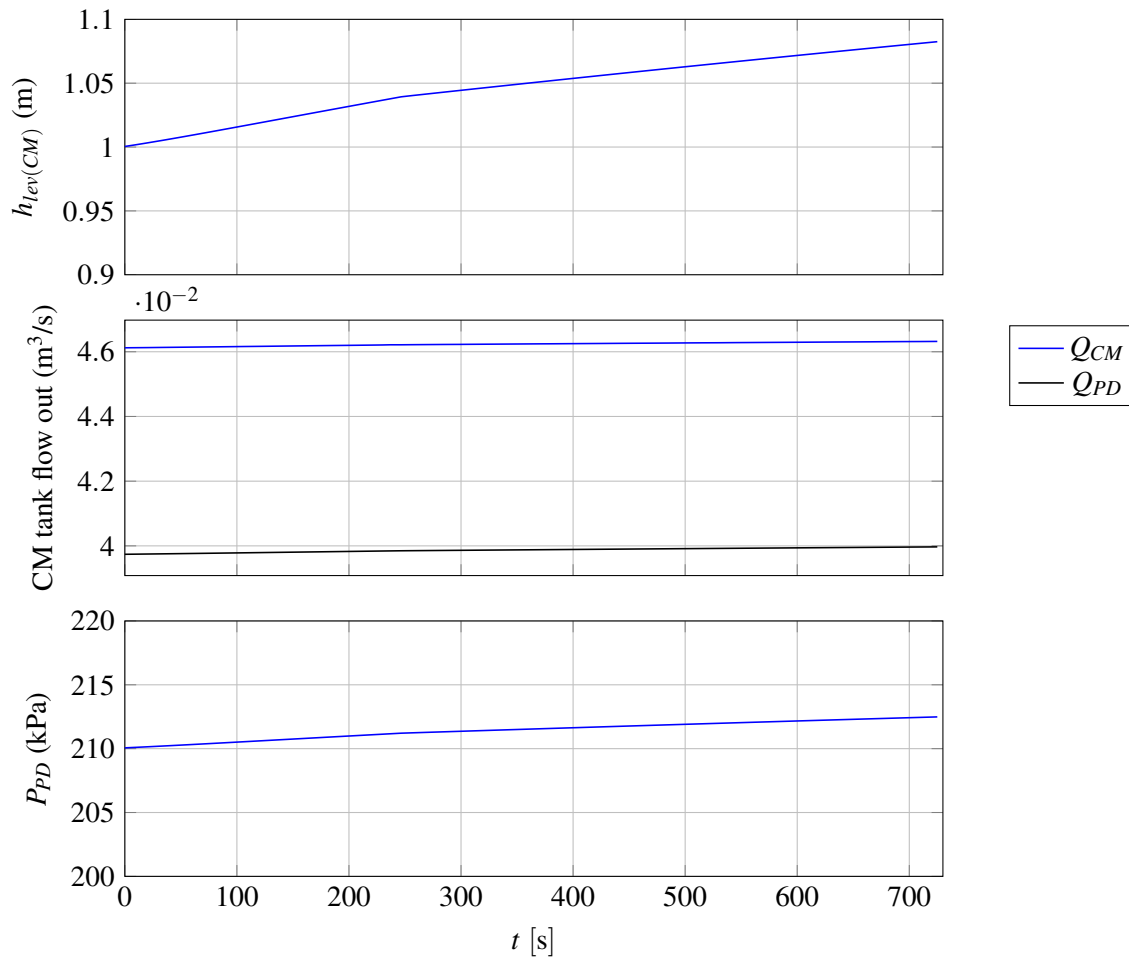
Figure 7.20. States and outputs of correct medium tank Simulink model during magnetic separator effluent losses simulation.

Note that at $t = 250$ s, the rate of change of the level of the correct medium tank ($h_{lev(CM)}$, at top in Figure 7.20) begins to reduce, as a result of the decreased flow of concentrate from the magnetic separator (seen in Figure 7.19).

7.5.2 Magnetic separator effluent losses state estimation

In this dissertation, the magnetic separator model has been heavily simplified (see (3.32)). It is also very poorly instrumented, and therefore it is not observable. The correct medium tank system, however, is fully observable (see Section 5), and the flow of medium into the correct medium tank is observable using an EKF (see Section 6.2). This means that if there are increased losses to the magnetic separator

effluent, the reduced flow of medium to the correct medium tank would be visible in that the EKF estimation of the flow rate into the tank would decrease. This is illustrated in Figure 7.21 in which the EKF algorithm is applied to the correct medium tank system, using the simulation scenario described in Section 7.5.1.

Note that the reduction in the simulated flow rate of medium into the correct medium tank ($Q_{in(CM)}$ in Figure 7.21) is very small in magnitude, due to the very small change in magnitude of the flow rate from the magnetic separator (Q_{MS} in Figure 7.19). $Q_{in(CM)}$ reduces from 0.0873 m^3/s to 0.0869 m^3/s. In addition, the state estimation of the flow rate of medium into the secondary tank ($Q_{in(CM)}$ in Figure 7.21) is quite noisy.
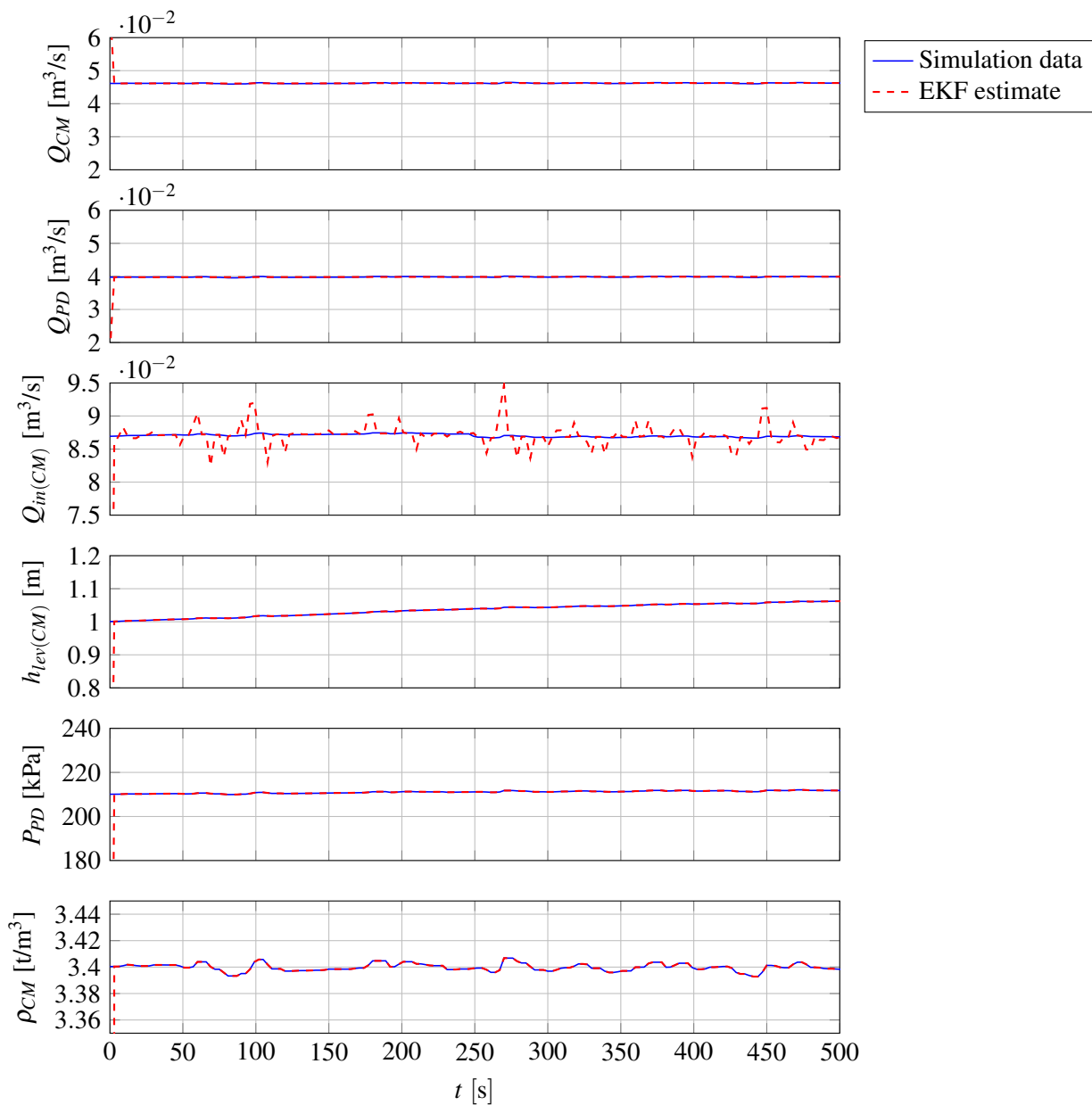
Figure 7.21. Simulation data and EKF estimates of correct medium tank states and outputs during simulated magnetic separator medium loss event.

7.6   CHAPTER SUMMARY

In this chapter, the three main sources of medium losses in the circuit were identified and simulated. State estimation was applied to the simulation, and, where available, to plant data as well. Losses at the mixing box due to overflows caused by blockages were simulated by changing the value of the outlet coefficient k_{MB} in the mixing box model. The state estimation results on the simulation show that the change in k_{MB} can be tracked. State estimation was also applied to plant data of a mixing box

blockage, and, as expected, the results show a decrease in the estimated value of k_{MB}. Medium losses at the screen were also simulated, and while this unit is modelled in steady-state and not observable, the simulation showed that the effect of these losses could be seen in a decrease in flow into the correct medium tank ($Q_{in(CM)}$). The EKF estimate of $Q_{in(CM)}$ adequately tracked this decrease, albeit with significant noise. Finally, medium losses to the magnetic separator were simulated. Again, this unit is modelled in steady-state and not observable, but the effect of losses here is seen in a decrease in $Q_{in(CM)}$. The simulation showed that the decrease in $Q_{in(CM)}$ as a result of these losses was very small in magnitude, and too small to be seen in the EKF estimate, given the noise in the estimate.

CHAPTER 8   DISCUSSION AND CONCLUSION

8.1   MEDIUM LOSSES IDENTIFICATION

8.1.1   Medium losses state estimation summary

The three main sources of medium losses in the DMS circuit have been investigated in Chapter 7: mixing box blockages and consequent overflows, drain-and-rinse screen losses, and magnetic separator effluent losses. It has been demonstrated that mixing box blockages can be seen in state estimation of the mixing box level and outlet coefficient, as well as in the flow of medium to the correct medium tank. This was demonstrated on simulated mixing box blockage data (Section 7.3.1) as well as on plant data during a mixing box blockage (Section 7.3.3).

The state estimation of the effect of losses at the product and waste drain-and-rinse screens, in Section 7.4, show that these losses can be seen in the flow of medium to the correct medium tank ($Q_{in(CM)}$, in Figure 7.17). Despite the noise present in the EKF estimation of $Q_{in(CM)}$, the change in the simulated value of $Q_{in(CM)}$ (which changes from 0.086 m^3/s to 0.085 m^3/s due to the simulated losses at the screens) is large enough to be visible in the EKF estimation. This is expected as the RMSE value of the $Q_{in(CM)}$ of the simulation is 0.002 m^3/s, and so because the magnitude of change in the $Q_{in(CM)}$ (0.006 m^3/s) is greater than the RMSE value, it is expected to be visible in the EKF estimation. With the context that the simulated screen losses are 5% of the simulated flow of medium to the screens, this result suggests that losses smaller than 5% would not be possible to detect in the EKF estimation of $Q_{in(CM)}$. It is also clear in the simulation of screen losses results, that the effect on the level is noticeable (see Figure 4.3).

The state estimation of the secondary tank system during the screen losses simulation demonstrates that it is not possible to see these losses in the EKF estimation of the flow of medium to the secondary tank ($Q_{in(sec)}$, in Figure 7.18). This is because the RMSE of this estimation is 0.002 m^3/s, while the

change in $Q_{in(sec)}$ is much smaller, at 1.4×10^{-4} m^3/s, due to the bleed stream of drained medium from the screens to the secondary tank being very small.

Similarly, the state estimation of the medium losses to the magnetic separator effluent in Section 7.5 demonstrates that it is not possible to see these losses in the EKF estimation of the flow of medium into the correct medium tank ($Q_{in(CM)}$, in Figure 7.21). This is because the change in $Q_{in(CM)}$ (0.0013 m^3/s) is larger than that of the RMSE of the estimate (0.002 m^3/s), due to the flow of medium from the magnetic separator concentrate to the correct medium tank being very small (see Q_{MS} Figure 7.19). As the simulated reduction in flow from the magnetic separator was 50%, it is therefore unlikely that any changes in the concentrate flow from the magnetic separators will be detectable in the EKF estimation of $Q_{in(CM)}$, as changes in Q_{MS} greater than 50% are highly unlikely.

8.1.2   Identifying medium losses

The state estimation of the three major sources of medium losses has shown that losses due to mixing box blockages can be seen in the state estimation of the outlet coefficient k_{MB}, while losses at the drain-and-rinse screens can be seen in the state estimation of the flow into the correct medium tank, $Q_{in(CM)}$, as well as the correct medium tank level, $h_{lev(CM)}$. Finally, the state estimation has shown that losses to the magnetic separator effluent can only be seen in the correct medium tank level, if at all. The implication of this is that only losses due to mixing box blockages can be definitively identified, as when they occur the EKF estimate of outlet coefficient k_{MB} will decrease, and, if the blockage is enough to result in overflows, the estimate of $Q_{in(CM)}$ will decrease.

On the other hand, medium losses at the screens are not definitively identifiable, as the effects of these losses is only seen in the estimate of $Q_{in(CM)}$, which will show a decrease. When this decrease is seen, it is not possible to attribute it to screen losses with certainty, as an unexpected decrease in $Q_{in(CM)}$ (unexpected in that it is not due to changing pump speeds) could be due to other unmeasured disturbances, such as a change in S_{PD} (the split of the ratio of overflow to underflow in the secondary densifier – see Section 3.9).

Table 8.1 shows the unmeasured disturbances that can occur (a change in the volumetric flow split of the primary and secondary densifier, S_{PD} and S_{SD} respectively, as well as medium losses), and the effect they have on key observable variables in the circuit (which can be estimated using the EKF).

Table 8.1. First order responses of key circuit variables as a result of medium losses.
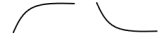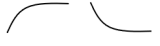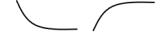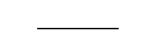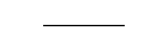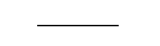
	Mixing box blockage	Magnetic separator losses	Drain-and-rinse screen losses	Change in S_{PD}	Change in S_{SD}
$Q_{in(CM)}$	↘	↘	↘	↗ ↘	↗ ↘
$Q_{in(sec)}$	↘	—	—	↘ ↗	—
k_{MB}	↘	—	—	—	—
$h_{lev(MB)}$	↗	—	—	—	—

Table 8.1 shows that a change in S_{SD} (which is both unobservable and uncontrolled) can produce the same effect on $Q_{in(CM)}$ and $Q_{in(sec)}$, as medium losses at the drain-and-rinse screens would cause. It is therefore not possible to definitively identify losses occurring at the drain-and-rinse screens. Therefore, to definitively detect screen losses, additional instrumentation is required to measure these as yet unmeasured disturbances.

Finally, medium losses to the magnetic separator effluent are also not identifiable, as the effect on both $Q_{in(CM)}$ and the correct medium tank level is very small.

8.1.3 Improving identification of medium losses

From Table 8.1, it is clear that if the flow rates of medium into the correct medium tank from the secondary densifier underflow was known, then the medium losses at the drain-and-rinse screens would be detectable, provided the losses were large enough. Therefore, simply through the addition of a flow meter on the secondary densifier underflow, medium losses at the screens would be identifiable.

Losses to the magnetic separator effluent are harder to identify. As seen in the simulation of these losses (see Section 7.5.1), the flow rate of concentrate medium returning from the magnetic separator is small in magnitude, and so a change in this flow rate is difficult to detect using an EKF estimate. Due to how small the flow is, installing a flow meter is not practical. To detect medium losses to the magnetic separator effluent, a density-focused model should be investigated, rather than a flow-focused model as developed in this work, as effluent losses are most likely to be most clearly seen in changes in density.

8.2   CONCLUDING REMARKS

A model for the flow of medium through a DMS circuit has been developed by modelling the individual units of the circuit. The models developed for the circuit units were then combined on a simulation platform (Simulink) and simulated. The circuit was simulated with a step change in the primary densifier speed introduced. The simulation results were consistent with the theory. The model was then validated using plant data for the correct medium tank and the mixing box. The model results showed close adherence to the plant data.

The unit models were then adapted to include unmeasured process disturbances and parameters (known in the simulation, but unknown in the plant) as unmeasured constant states, and these augmented units were assessed for observability. This observability analysis showed that the mixing box, correct medium tank and secondary tank are fully observable given the current level of instrumentation of the circuit. The dilute medium tank is not, however, fully observable. Additionally, the drain-and-rinse screens, primary and secondary densifiers, and magnetic separator are modelled in steady-state, and given the current instrumentation, there is no method to validate these models online.

Following this, state estimation using an EKF, was then developed for the observable units within the circuit: the correct medium and secondary tanks, and the mixing box. The state estimation was first applied to simulated data. The estimation results indicated adequate tracking of the model states and outputs. This included for the flow rates of slurry entering the correct medium and secondary tanks, which are known in the simulation but not measured in the plant, and therefore require estimation. Similarly, the state estimation for the mixing box included estimation of the mixing box outlet coefficient k_{MB}, which is unknown in the plant, and subject to change during blockages. State estimation was then applied to plant data for the observable units, and the estimation results for the outputs tracked the plant outputs adequately. For both the simulation estimates and the plant data estimates of the flow of medium into the correct medium and secondary tanks, there was significant noise in the estimates.

The three sources of loss of medium in the circuit were then analysed. It is valuable to be able to detect medium losses in the DMS circuit as these can contribute up to 39% of DMS plant operating costs (Dardis, 1989). If losses can be detected, and the source identified, they can be acted on and reduced.

Medium can be lost due to mixing box blockages causing medium overflows, at the drain-and-rinse screens (due to adhesion to the ore, or screen blinding), and in the magnetic separator effluent. These losses were simulated in the developed DMS circuit model, and state estimation applied to the simulations. In the case of a mixing box blockage, plant data was available, and so state estimation was applied to the mixing box blockage plant data. The state estimation results indicated that mixing box blockages are identifiable through state estimation, while only medium losses of 5% or greater at the product and waste drain-and-rinse screens can be seen in the state estimation. Furthermore, losses at the drain-and-rinse screens produce the same effect on the flow of material into the circuit tanks as a change in the volumetric split to overflow in the secondary densifier. These losses are therefore not definitively identifiable; however, analysis shows that the installation of a flow meter on the overflow of the secondary densifier could resolve this, and allow the screen losses to be identified. Finally, the estimation results show that medium losses to the magnetic separator are not identifiable using the developed model and state estimation, due to the flow rates of concentrate from the magnetic separator being small in magnitude.

8.3   RECOMMENDED AVENUES FOR FUTURE WORK

This dissertation has shown that, out of the three main sources of medium losses, losses caused by blockages in the mixing box resulting in overflows are the only losses definitively identifiable using the model developed. Given this, a recommended avenue for future work is to install the suggested flow meter on the secondary densifier overflow, and conduct a study on medium losses at the drain-and-rinse screens. Episodes of high medium losses at the drain-and-rinse screens can be identified in plant data, and state estimation can be applied to this data to determine if these losses can be definitively identified with the addition of the new flow meter.

More focus can also be given to losses to the magnetic separator effluent. This dissertation has shown that a flow-focused model (as developed here-in) is not capable of yielding a good enough indication of changes in the magnetic separator concentrate flow rate. Future work can investigate the merits of a model that includes density modelling, for application in the detection of medium losses to the magnetic separator effluent.

Finally, this dissertation has applied state estimation retrospectively to plant data. Further work can be done to implement this live on the plant, so that mixing box blockages can be detected in real-time, thereby reducing medium overflows at the mixing box. A control system can also be developed, to

reduce the flow of ore or medium to the mixing box when a blockage occurs, and therefore control the state-estimated mixing box level, and avoid overflows.

REFERENCES

Baker, J. (1977). The development of the magnetic drum separator performance line., *Mine and Quarry* **6**(2): 52–56.

Barbee, C., Luttrell, G., Wood, C. and Bethell, P. (2005). Simulation of heavy medium cyclone performance, *Minerals & Metallurgical Processing* **21**(4): 38–42.

Bueno, E. A. (2021). *Simulacao De Hidrociclones*, PhD thesis, Universidade Federal de Ouro Preto.

Clarkson, C. J. and Wood, C. J. (1993). A model of dense medium cyclone performance, *Coal Preparation* **12**(1-4): 101–115.

Dardis, K. A. (1989). The design and operation of heavy medium recovery circuits for improved medium recovery, *Coal Preparation* **7**(3-4): 119–157.

Davis, J. and Lyman, G. (1983). Magnetite recovery using a wet drum separator, *Australas. Inst. Min. Metall. Proc.;(Australia)* **287**: 51–60.

Dong, K. J., Yu, A. and Brake, I. (2009). DEM simulation of particle flow on a multi-deck banana screen, *Minerals Engineering* **22**(11): 910–920.

Dunglison, M. E. (1999). *A general model of the dense medium cyclone*, PhD thesis, The University of Queensland.

REFERENCES

Firth, B. and O'Brien, M. (2010). Some aspects of banana screen operation, *International Coal Preparation Congress 2010 Conference Proceedings*, SME, p. 231.

Flintoff, B. C., Plitt, L. R. and Turak, A. A. (1987). Cyclone modelling: a review of present technology, *CIM Bulletin* **80**: 39–50.

Ghafouri, J. H., Khayatzadeh, F. H. and Khayatzadeh, A. H. (2012). Dynamic modeling of variable speed centrifugal pump utilizing matlab / simulink, *International Journal of Science and Engineering Investigations* **1**(5).

Jang, L. K. (2016). Level control by regulating control valve at the bottom of a gravity-drained tank, *Chemical Engineering Education* **50**(4): 245–250.

Kallesoe, C., Cocquempot, V. and Izadi-Zamanabadi, R. (2006). Model based fault detection in a centrifugal pump application, *IEEE Transactions on Control Systems Technology* **14**(2): 204–215.

Karassik, I. J. (2008). *Centrifugal Pump Theory, Analysis, and Performance*, McGraw-Hill Professional, p. 29–117.

Legault-Seguin, E., Mohns, C. and Rylatt, M. (2017). Dense medium separation: An effective and robust preconcentration technology, *CIM Journal* **8**(3): 244.

Lobanoff, V. S. and Ross, R. R. (1992). *Specific Speed and Modelling Laws*, 2nd edn, Gulf Professional Publishing, p. 13–15.

Lundt, M. and Grewalt, I. (2017). Dense media separation - a valuable process for preconcentration, *Conference Proceedings: Metallurgical Plant Design and Operating Strategies-World's Best Practice*, pp. 11–12.

Lyman, G., Askew, H., Wood, C. and Davis, J. (1982). Dynamic modelling of dense medium cyclone washing circuits, *Proceedings of the Mill Operations Conference, NW Queensland, Australia, AusIMM*, pp. 369–381.

REFERENCES

Lynch, A. and Rao, T. (1975). Modelling and scale-up of hydrocyclone classifiers, *Proceedings of the 11th International Mineral Processing Congress*, pp. 245–269.

Maré, E., Beven, B. and Crisafio, C. (2015). 10 - developments in nonmagnetic physical separation technologies for hematitic/goethitic iron ore, *in* L. Lu (ed.), *Iron Ore*, Woodhead Publishing, pp. 309–338.

Meyer, E. J. (2015). *Nonlinear model predictive control for coal plants*, PhD thesis, The University of Pretoria.

Meyer, E. J. and Craig, I. K. (2010). The development of dynamic models for a dense medium separation circuit in coal beneficiation, *Minerals Engineering* **23**(10): 791–805.

Mulder, M. (1985). Practical methods developed by iscor to curtail ferrosilicon losses, with special reference to the methods applied at the Sishen Iron-Ore Mine, *2nd Samancor Symposium on Dense-Medium, Perth*.

Nageswararao, K. (1978). *Further developments in the modelling and scale up of Industrial Hydrocyclones*, PhD thesis, University of Queensland.

Nageswararao, K., Wiseman, D. and Napier-Munn, T. (2004). Two empirical hydrocyclone models revisited, *Minerals Engineering* **17**(5): 671–687.

Napier-Munn, T. (2018). The dense medium cyclone–past, present and future, *Minerals Engineering* **116**: 107–113.

Napier-Munn, T. J. (1991). Modelling and simulating dense medium separation processes - A progress report, *Minerals Engineering* **4**(3-4): 329–346.

Napier-Munn, T. J., Kojovic, T., Scott, I. A., Shi, F., Masinja, J. H. and Baguley, P. J. (1995). Some causes of medium loss in dense medium plants, *Minerals Engineering* **8**(6): 659–678.

REFERENCES

Narasimha, M., Brennan, M. S., Holtham, P. N. and Napier-Munn, T. J. (2007). A comprehensive CFD model of dense medium cyclone performance, *Minerals Engineering* **20**(4): 414–426.

O'Brien, M., Firth, B., Holtham, P., Hu, S., Scott, N. and Burger, A. (2016). Optimisation and control of dense medium cyclone circuits, *in* V. Litvinenko (ed.), *XVIII International Coal Preparation Congress*, Springer International Publishing, Cham, pp. 297–302.

Plitt, L. R. (1976). A mathematical model of the hydrocyclone classifier, *CIM Bulletin* **69**(776).

Rayner, J. G. and Napier-Munn, T. (2003a). A mathematical model of recovery of dense medium magnetics in the wet drum magnetic separator, *International Journal of Mineral Processing* **69**(1): 157–173.

Rayner, J. G. and Napier-Munn, T. J. (2003b). A mathematical model of concentrate solids content for the wet drum magnetic separator, *International Journal of Mineral Processing* **70**(1-4): 53–65.

Ribeiro, M. I. (2004). Kalman and extended Kalman filters: Concept, derivation and properties, *Institute for Systems and Robotics* **43**(46): 3736–3741.

Schmitz, K. S. (2017). *Physical Chemistry: Concepts and theory*, Elsevier.

Schneider, R. and Georgakis, C. (2013). How to not make the extended Kalman filter fail, *Industrial Engineering Chemistry Research* **52**(9): 3354–3362.

Scott, N. J. C. (2017). *Dynamic Analysis of Dense Medium Circuits*, PhD thesis, The University of Queensland.

Seborg, D. E., Edgar, T. F., Mellichamp, D. A. and Doyle III, F. J. (2016). *Process Dynamics and Control*, John Wiley & Sons.

Sepúlveda, J. E. (2004). Methodologies for the evaluation of grinding media consumption rates at full plant scale, *Minerals Engineering* **17**(11–12): 1269–1279.

REFERENCES

Shannon, C. (1948). A Mathematical Theory of Communications, *Bell Systems Technical Journal* **27**.

Simpson, A. R. and Marchi, A. (2013). Evaluating the approximation of the affinity laws and improving the efficiency estimate for variable speed pumps, *Journal of Hydraulic Engineering* **139**(12): 1314–1317.

Skogestad, S. and Postlethwaite, I. (2005). *Multivariable Feedback Control: Analysis and Design*, 2nd edn, Wiley, p. 132–137.

Sripriya, R., Dutta, A., Dhall, P. K., Narasimha, M., Kumar, V. and Tiwari, B. S. (2006). An analysis of medium losses in coal washing plants, *International Journal of Mineral Processing* **80**(2-4): 177–188.

Stener, J. F., Carlson, J. E., Pålsson, B. I. and Sand, A. (2016). Direct measurement of internal material flow in a bench scale wet low-intensity magnetic separator, *Minerals Engineering* **91**: 55–65. Physical Separation.

Svarovski, L. (2000). *Hydrocyclones*, 4th edn, Butterworth-Heinemann, p. 191–243.

Talmon, A. (2016). Pump and pipeline characteristics, *Dredge Pumps and Slurry Transport* pp. 7.1–7.4.

Tom, P. (2015). *Optimization of Dense Medium Cyclone Plant for the Beneficiation of Low Grade Iron Ore with Associated High Proportion of Near-Density Material at Sishen Iron Ore Mine*, Master's thesis, University of the Witwatersrand.

Ungarala, S. (2012). On the iterated forms of Kalman filters using statistical linearization, *Journal of Process Control* **22**(5): 935–943.

Wiegel, R. L. (1976). *The development and use of mathematical models in the computer simulation of the magnetic taconite concentration process*, PhD thesis, University of Queensland.

Willmott, C. J. (1981). On the validation of models, *Physical Geography* **2**(2): 184–194.

REFERENCES

Zhang, L. and Xia, X. (2014). A model predictive control for coal beneficiation dense medium cyclones, *IFAC Proceedings Volumes (IFAC-PapersOnline)* **19**: 9810–9815.

ADDENDUM A   OBSERVABILITY MATRICES

Correct medium tank system:

$$O_{CM} = \begin{bmatrix} 1 & 0 & 0 & 0 \\ \rho_{CM,0}g & 0 & \frac{\rho_{CM,0}Q_{PD,0}}{A_{PD}^2} & 0 \\ 0 & -\frac{1}{A_{CM}} & -\frac{1}{A_{CM}} & \frac{1}{A_{CM}} \\ \frac{-g\rho_{CM,0}^2 Q_{PD,0}}{A_{PD}^2 k_{j(PD)}} & \frac{-g\rho_{CM,0}}{A_{CM}} & \frac{\rho_{CM,0}Q_{PD,0}(2k_p Q_{PD,0}+2S_{PD}g\rho_{CM,0}Q_{PD,0})}{A_{PD}^2 k_{j(PD)}} - \frac{g\rho_{CM,0}}{A_{CM}} & \frac{g\rho_{CM,0}}{A_{CM}} \\ O_{CM}(5,1) & O_{CM}(5,2) & O_{CM}(5,3) & 0 \\ O_{CM}(6,1) & O_{CM}(6,2) & O_{CM}(6,3) & O_{CM}(6,4) \\ O_{CM}(7,1) & O_{CM}(7,2) & O_{CM}(7,3) & O_{CM}(7,4) \\ O_{CM}(8,1) & O_{CM}(8,2) & O_{CM}(8,3) & O_{CM}(8,4) \end{bmatrix} \quad (A.1)$$

$$O_{CM}(5,1) = \frac{-g\rho_{CM,0}}{A_{CM}k_{j(CM)}} - \frac{g\rho_{CM,0}}{A_{CM}k_{j(PD)}}$$

$$O_{CM}(5,2) = \frac{2k_pQ_{CM,0} + 2S_{CM}g\rho_{CM,0}Q_{CM,0}}{A_{CM}k_{j(CM)}}$$

$$O_{CM}(5,3) = \frac{2k_pQ_{PD,0} + 2S_{PD}g\rho_{CM,0}Q_{PD,0}}{A_{CM}k_{j(PD)}}$$

$$O_{CM}(6,1) = \frac{g\rho_{CM,0}^2 Q_{PD,0}(2k_pQ_{PD,0} + 2S_{PD}g\rho_{CM,0}Q_{PD,0})}{A_{PD}^2 k_{j(PD)}^2} - g^2 u_{3,0}^2 \left(\frac{1}{A_{CM}k_{j(CM)}} + \frac{1}{A_{CM}k_{j(PD)}} \right)$$

$$O_{CM}(6,2) = \frac{g\rho_{CM,0}(2k_pQ_{CM,0} + 2_SCMg\rho_{CM,0}Q_{CM,0}}{A_{CM}k_j(CM)} + \frac{g\rho_{CM,0}^2 Q_{PD,0}}{A_{CM}A_{PD}^2 k_{j(PD)}}$$

$$O_{CM}(6,3) = \frac{1}{A_{PD}^2}g\rho_{CM,0}\frac{2k_pQ_{PD,0} + 2S_{PD}g\rho_{CM,0}Q_{PD,0}}{A_{CM}k_{j)PD)}} - \rho_{CM,0}Q_{PD,0}\frac{(2k_pQ_{PD,0} + 2S_{PD}g\rho_{CM,0}Q_{PD,0})^2}{k_{j(PD)}^2}$$
$$- \frac{g\rho_{CM,0}}{A_{CM}k_{j(PD)}}$$

$$O_{CM}(6,4) = \frac{-g\rho_{CM,0}^2 Q_{PD,0}}{A_{CM}A_{PD}^2 k_{j(PD)}}$$

$$O_{CM}(7,1) = g\rho_{CM,0}\frac{2k_pQ_{CM,0} + S_{CM}g\rho_{CM,0}Q_{CM,0}}{A_{CM}k_{j(CM)}^2} + \frac{g\rho_{CM,0}(2k_pQ_{PD,0} + 2S_{PD}g\rho_{CM,0}Q_{PD,0})}{A_{CM}k_{j(PD)}^2}$$

$$O_{CM}(7,2) = \frac{1}{A_{CM}}\frac{g\rho_{CM,0}}{A_{CM}^2 k_{j(PD)}} - \frac{(2k_pQ_{CM,0} + 2S_{CM}g\rho_{CM,0}Q_{CM,0})^2}{k_{j(CM)}^2} - \frac{g\rho_{CM,0}}{A_{CM}k_{j(CM)}}$$

$$O_{CM}(7,3) = \frac{g\rho_{CM,0}}{A_{CM}^2 k_{j(CM)}} - \frac{1}{A_{CM}}\frac{2k_pQ_{PD,0} + 2S_{PD}g\rho_{CM,0}Q_{PD,0})^2}{k_{j(PD)}^2} - \frac{g\rho_{CM,0}}{A_{CM}k_{j(PD)}}$$

$$O_{CM}(7,4) = -\frac{g\rho_{CM,0}}{A_{CM}k_{j(CM)}}A_{CM}^2 k_{j(CM)} - \frac{g\rho_{CM,0}}{A_{CM}k_{j(CM)}}A_{CM}^2 k_{j(PD)}$$

$$O_{CM}(8,1) = g\rho_{CM,0}\frac{2gk_p\rho_{CM,0}Q_{CM,0}}{A_{CM}k_{j(CM)}^2} + \frac{2gk_p\rho_{CM,0}Q_{PD,0}}{A_{CM}k_{j(PD)}^2}$$
$$+ \frac{\rho_{CM,0}Q_{PD,0}}{A_{PD}^2}\left(g\rho_{CM,0}\frac{g\rho_{CM,0}}{Ak_{j(CM)}} + \frac{g\rho_{CM,0}}{A_{CM}k_{j(PD)}} + \frac{g\rho_{CM,0}}{A_{CM}k_{j(PD)}} - \frac{4gk_p^2\rho_{CM,0}Q_{PD,0}^2}{k_{j(PD)}^3} \right)$$

$$O_{CM}(8,2) = \frac{-g\rho_{CM,0}}{A_{CM}}\left(\frac{4k_p^2Q_{CM,0}^2}{k_{j(CM)}^2} - \frac{g\rho_{CM,0}}{A_{CM}k_{j(CM)}^2} + \frac{g^2\rho_{CM,0}^2}{A_{CM}^2 k_{j(PD)}} \right)$$
$$- \frac{\rho_{CM,0}Q_{PD,0}}{A_{PD}^2}\left(\frac{2gk_p\rho_{CM,0}Q_{PD,0}}{A_{CM}k_{j(PD)}^2} + \frac{2gk_p\rho_{CM,0}Q_{CM,0}}{A_{CM}k_{j(CM)}k_{j(PD)}} \right)$$

$$O_{CM}(8,3) = \frac{\rho_{CM,0}Q_{PD,0}}{A_{PD}^2}$$

$$\times \left(\left(\left(\frac{2k_p Q_{PD,0}}{k_{j(PD)}} \frac{4k_p^2 Q_{PD,0}^2}{k_{j(PD)}^2} - \frac{g\rho_{CM,0}}{A_{CM}k_{j(PD)}} \right) - \frac{2gk_p \rho_{CM,0}Q_{PD,0}}{A_{CM}k_{j(PD)}^2} \right) \right.$$

$$\left. - g\rho_{CM,0} \left(\frac{1}{A_{CM}} \left(\frac{4k_p^2 Q_{PD,0}^2}{k_{j(PD)}^2} - \frac{g\rho_{CM,0}}{A_{CM}k_{j(PD)}} \right) - \frac{g\rho_{CM,0}}{A_{CM}^2 k_{j(CM)}} \right) \right.$$

$$O_{CM}(8,4) = \frac{2gk_p \rho_{CM,0}^2 Q_{PD,0}^2}{A_{CM}A_{PD}^2 k_{j(PD)}^2} - g\rho_{CM,0} \left(\frac{g\rho_{CM,0}}{A_{CM}^2 k_{j(CM)}} + \frac{g\rho_{CM,0}}{A_{CM}^2 k_{j(PD)}} \right)$$

Secondary tank system:

$$O_{sec} = \begin{bmatrix} 1 & 0 & 0 \\ g\rho_{sec,0} & \frac{-\rho_{sec,0}Q_{SD,0}}{A_{SD}^2} & 0 \\ 0 & -\frac{1}{A_{sec}} & \frac{1}{A_{sec}} \\ \frac{-g\rho_{sec,0}^2 Q_{SD,0}}{A_{SD}^2 k_{j(SD)}} & \frac{2S_{SD}g\rho_{sec,0}^2 Q_{SD,0}^2}{A_{SD}^2 k_{j(SD)}} - \frac{g\rho_{sec,0}}{A_{sec}} & \frac{g\rho_{sec,0}}{A_{sec}} \\ \frac{g\rho_{sec,0}}{A_{sec}k_{j(SD)}} & \frac{(2S_{SD}g\rho_{sec,0}Q_{SD,0})}{A_{sec}k_{j(SD)}} & 0 \\ -\frac{g^2\rho_{sec,0}^2}{A_{sec}k_{j(SD)}} + \frac{(2S_{SD}g^2\rho_{sec,0}^2 Q_{SD,0})}{A_{sec}k_{j(SD)}} & \frac{\rho_{sec,0}Q_{SD,0}}{A_{SD}^2} \left(\frac{g\rho_{sec,0}}{A_{sec}k_{j(SD)}} - \frac{4S_{SD}^2 g^2\rho_{sec,0}^2 Q_{SD,0}^2}{k_{j(SD)}^2} \right) + \frac{2S_{SD}g^2\rho_{sec,0}^2 Q_{SD,0}}{A_{sec}k_{j(SD)}} & \frac{-g\rho_{sec,0}^2 Q_{SD,0}}{A_{sec}A_{SD}^2 k_{j(SD)}} \end{bmatrix}$$

$$(A.2)$$

Dilute medium tank system:

$$O_{DM} = \begin{bmatrix} 1 & 0 & 0 & 0 & 0 \\ 0 & -\frac{1}{A_{DM}} & -\frac{l_{DM,0}}{A_{DM}} & \frac{1}{A_{DM}} & 0 \\ -\frac{g\rho_{DM,0}}{A_{DM}k_{j(DM)}} & \frac{2S_{DM}gQ_{DM,0}\rho_{DM,0}}{A_{DM}k_{j(DM)}} & 0 & 0 & -\frac{g(H_{DM}n_{DM,0}^2 - S_{DM}Q_{DM,0}^2) + gh_{lev(DM),0}}{A_{DM}k_{j(DM)}} \\ \frac{2S_{DM}g^2 Q_{DM,0}\rho_{DM,0}^2}{A_{DM}k_{j(DM)}^2} & O_{DM}(4,2) & \frac{-gl_{DM,0}\rho_{DM,0}}{A_{DM}^2 k_{j(DM)}} & \frac{-g\rho_{DM,0}}{A_{DM}^2 k_{j(DM)}} & O_{DM}(4,5) \\ O_{DM}(5,1) & O_{DM}(5,2) & O_{DM}(5,3) & O_{DM}(5,4) & O_{DM}(5,5) \end{bmatrix}$$

$$(A.3)$$

$$O_{DM}(4,2) = \frac{1}{A_{DM}} \left(\frac{g\rho_{DM,0}}{A_{DM}k_{j(DM)}} - \frac{4S_{DM}^2 g^2 Q_{DM,0}^2 \rho_{DM,0}^2}{k_{j(DM)}^2} \right)$$

$$O_{DM}(4,5) = \frac{2S_{DM}g Q_{DM,0}\rho_{DM,0}g(H_{DM}n_{DM,0}^2 - S_{DM}Q_{DM,0}^2 + h_{lev(DM),0})}{A_{DM}k_{j(DM)}}$$

$$O_{DM}(5,1) = \frac{g^2 \rho_{DM,0}^2}{A_{DM}k_{j(DM)}^2} - \frac{4S_{DM}^2 g^3 Q_{DM,0}^2 \rho_{DM,0}^3}{A_{DM}k_{j(DM)}^3}$$

$$O_{DM}(5,2) = -\frac{2S_{DM}g^2 Q_{DM,0}\rho_{DM,0}^2}{A_{DM}^2 k_{j(DM)}^2} - \frac{2S_{DM}g Q_{DM,0}\rho_{DM,0}}{A_{DM}k_{j(DM)}} \left(\frac{g\rho_{DM,0}}{A_{DM}k_{j(DM)}} - \frac{4S_{DM}^2 g Q_{DM,0}^2 \rho_{DM,0}^2}{k_{j(DM)}^2} \right)$$

$$O_{DM}(5,3) = \frac{2S_{DM}g^2 l_{DM,0} Q_{DM,0}\rho_{DM,0}^2}{A_{DM}^2 k_{j(DM)}^2}$$

$$O_{DM}(5,4) = \frac{2S_{DM}g^2 Q_{DM,0}\rho_{DM,0}^2}{A_{DM}^2 k_{j(DM)}^2}$$

$$O_{DM}(5,5) = \frac{g^2 \rho_{DM,0}g Q_{DM,0}\rho_{DM,0}(H_{DM}n_{DM,0}^2 - S_{DM}Q_{DM,0}^2 + h_{lev(DM),0})}{A_{DM}^2 k_{j(DM)}^2}$$

$$- \frac{4S_{DM}^2 g^3 Q_{DM,0}^2 \rho_{DM,0}^2 (H_{DM}n_{DM,0}^2 - S_{DM}Q_{DM,0}^2 + h_{lev(DM),0})}{A_{DM}k_{j(DM)}^3}$$